Master's thesis

NTNU
Norwegian University of Science and Technology
Faculty of Engineering
Department of Energy and Process Engineering

Andrea Engøy

Development of a Francis Turbine Test Rig at Kathmandu University

A Measurement System for Axial Load and Friction Torque

Master's thesis in Engineering and ICT
Supervisor: Ole Gunnar Dahlhaug
December 2019

NTNU
Norwegian University of
Science and Technology

Andrea Engøy

Development of a Francis Turbine Test Rig at Kathmandu University

A Measurement System for Axial Load and Friction Torque

Master's thesis in Engineering and ICT
Supervisor: Ole Gunnar Dahlhaug
December 2019

Norwegian University of Science and Technology
Faculty of Engineering
Department of Energy and Process Engineering

NTNU
Norwegian University of
Science and Technology

Abstract

Nepal has great potentials for hydropower that is not yet utilized. This Master's thesis is a part of the long-standing collaboration between Kathmandu University (KU) and Norwegian University of Science and Technology (NTNU) to develop a Turbine Testing Lab (TTL). The goal of the lab is to perform hydropower research within the standards of IEC60193. The objective of this thesis is to develop an axial load and friction torque measuring device to be installed at TTL. The device is a part of the bearing block and is measuring the forces with strain gauges. The main challenge is that the strains caused by the axial load are much bigger than that caused by friction torque.

Two designs have been investigated. The first design has been experimentally tested, calibration equations have been obtained, and uncertainty analysis has been performed. It is found that the calibration equations for the axial load and friction torque should not be functions of the same strain gauges, as the uncertainties become too high. As a result of the insight obtained during the work on the first design, an improved design is developed. This second design is the recommended version to install. Based on numerical analysis, the output from the strain gauges should be such that the final calibration equations are not related, meaning they are functions of one strain gauge set each. This will lower the uncertainties drastically. A compendium that accompanies the final design to ease the process of completion has been made as part of this thesis.

Sammendrag

Nepal har et stort potensial for vannkraft som ikke er utnyttet. Denne masteroppgaven er en del av det langvarige samarbeidet mellom Kathmandu University (KU) og Norges teknisk-naturvitenskapelige universitet (NTNU) for å utvikle en lab for testing av vannturbiner, kalt Turbine Testing Lab (TTL). Målet for laben er å kunne utføre tester i henhold til standardene i IEC60193. Målsetningen for denne oppgaven er å utvikle et målesystem for aksiell last og friksjonsmoment som skal installeres på TTL. Enheten er en del av bæreblokken og den måler krefter med strekklapper. Hovedutfordringen er at tøyningene forårsaket av aksiell last er mye større enn tøyningene forårsaket av friksjonsmoment.

To design er undersøkt. The første designet har blitt testet eksperimentelt, kalibrasjonsligninger er funnet og en usikkerhetsanalyse er utført. Det ble bekreftet at kalibrasjonsligningene for aksielle krefter og friksjonsmoment ikke kan være funksjoner av de samme strekklappene fordi usikkerhetene da blir for store. Som et resultat av lærdommen av arbeidet på det første designet, er et forbedret design utviklet. Dette andre designet er den anbefalte versjonen å installere på TTL. Numeriske analyser gir grunn til å tro at strekklappene vil gi målinger som gir kalibrasjonsligninger som er uavhengig av hverandre. Dette vil senke usikkerhetene drastisk. Et kompendium som akkompagnerer det endelige designet er også skrevet for å lette fullføringsprosessen.

Preface

I feel very lucky to have had the opportunity to write a Master's thesis that is contributing to the development of hydropower research in Nepal. The work being meaningful is very motivating. I am especially thankful for the opportunity to visit Kathmandu University and to meet the staff working in the lab, and I am looking forward to visiting again in the future.

Thank you, Professor Ole Gunnar Dahlhaug, for such a meaningful assignment and your essential guidance. Thanks to Joar Grilstad and Bård Brandåstrø for the indispensable help during my lab work. Bjørn Winther Solemslie, thank you for sharing your essential insight and for performing academic first aid.

Thanks to all the students at VKL for creating such a good social environment. Lunch, cake Fridays, and pizza evenings have fulfilled the need for silly talks and relieving laughs. Thanks to Aatma Kayastha and all the other students and employees at TTL for your help and fun times during our visit to Dhulikhel.

Andrea Engøy
Trondheim, 20th of December, 2019

Table of Contents

List of Figures

List of Tables

Abbreviations

ALMD	Axial Load Measuring Device
ATMD	Axial load and friction Torque Measuring Device
BEP	Best Efficiency Point
CAD	Computer-aided design
DAQ	Data Acquisition
deg	Degree
GF	Gauge Factor
IEC	International Electrotechnical Commission
KU	Kathmandu University
LIFO	Last In First Out
NI	National Instruments
NORAD	Norwegian Agency of Development Corporation
NTNU	Norwegian University of Science and Technology
rpm	Revolutions per minute
RSS	Root of the Sum of the Squares
SG	Strain Gauges
TML	Tokyo Measuring Instruments Lab
TTL	Turbine Testing Lab (at KU)
VKL	Waterpower laboratory (at NTNU)

List of Symbols

Symbol	Description	Unit
A	Area	m^2
B_1	Inlet height	m
b’	Repeatability	-
β	Blade angle	deg
c	Velocity	m/s
D	Diameter	m
E	Elasticity Module	N/m^2
ϵ	Strain	-
η	Efficiency	-
F	Force	N
f_0	Zero Deviation	-
g	Gravitational constant	m/s^2
H	Head	m
h	Height	m
h_{mean}	Hysteresis	-
k	Constant	-
L	Length	m
N	Normal force	N
n	Revolutions per minute	rpm
n_{S_x}	Size of sample	-
n_x	Number of measurement series pair	-
ω	Angular velocity	rad/s
Ω	Speed number	-
p	Pressure	Pa
P	Power	W
P*	Power at BEP	W
Q	Discharge	m^3/s
R	Resistance	Ω
r	Radius	m
ρ	Density	kg/m^3
S_x	Standard deviation	-
t	Student-t distribution number	-
T	Torque	Nm
U	Voltage	V
u	Blade velocity	m/s^2
w	Uncertainty	-
x_{ij}	Data from measurement series i in measurement point j	-

Chapter 1

Introduction

Nepal is a relatively small country compared to its two neighboring countries, India and China, and has become economically dependent and highly influenced by both. With the challenging nature of the skyscraping Himalayas in the north and a landscape dominated by jungle and agriculture in the south, this country has different challenges in improving the living conditions of the people. There is a big gap between rich and poor, and after the powerful earthquakes in 2015, it was recorded that 25% of the country's inhabitants lived under the poverty threshold [1]. Social development and economic growth will have a positive impact on people's lives. One step in that direction is the cooperation between Nepali authorities and the Norwegian Agency for Development Cooperation (NORAD) focusing on education, women and equality, good governance, climate change, and energy production. The latter is the focus area of most relevance to this thesis. By contributing to a stable power grid and ensuring the people of Nepal access to electrical power, better living conditions could be achieved for everyone, regardless of financial status. By utilizing Nepal's huge potentials for hydropower, the country could not only be self-sufficient but even able to export energy. [2]

Former NTNU principal Inge Johansen started the collaboration between the Norwegian University of Science and Technology (NTNU) and Kathmandu University (KU) in 1991. This was also the year that Nepal became a democracy, and 5-year free compulsory schooling was introduced [1]. In the years of the civil war, between 1996 to 2006, the partnership continued, and in 1999, professor Arne Kjølle contributed to the decision of building a Turbine Testing Lab (TTL) at KU. Between 2003 and 2004, Professor Ole Gunnar Dahlhaug had a sabbatical year in Nepal to supervise the planning of the construction of TTL and kept strengthening the relationship between the two universities. Since 2003, it has continuously been one or more Norwegian master students working on the development of TTL through their theses, and there have been several PhD-candidates from KU doing their research at NTNU obtaining increased knowledge to bring back to Nepal.

1.1 The Waterpower Laboratory at NTNU

Hydropower has been used in the Norwegian industry for centuries, and as the demand for electricity increased in the early 1900s, the use of hydropower in energy production also increased [3]. This led to an interest in improving the turbine design as a small improvement would mean much more energy generated. The Waterpower Laboratory (VKL) at NTNU was built in 1917 and has, since then, had a leading role in hydropower research both nationally and globally. [4]

VKL has had various research areas, including test rigs for Francis, Pelton, and pump turbines, all within the standards of IEC60193 [5]. The current Francis rig is built in such a way that model tests with dynamic similarity to a corresponding prototype can be performed. The rig can be run in a closed or open loop, and the two pumps of 330 kW can be run in series or parallel. The combination of closed-loop and pumps run in series gives a maximum head of 100 m. When the pumps are run in parallel in a closed-loop, the maximum flow is 1 m^3/s. The open-loop mode pumps the water up to the upper reservoir, which has a free water surface, in the attic of the laboratory, giving the water a natural head of 16 m. [6]

1.2 The Turbine Testing Lab at Kathmandu University

In 2011, the building for the Turbine Testing Lab (TTL) was complete, and by fall 2019, all the major mechanical parts have been installed such that the Francis rig is almost functional. Improvements and installation of smaller devices, like an axial load and friction torque measuring device, remains. When the lab is complete within the standards of IEC60193, TTL will devote much time to research sediment erosion in turbines as this is one of the main challenges in hydropower in Nepal.

The design of the Turbine Testing Lab (TTL) at Kathmandu University (KU) is based on the design of the Francis rig at VKL. The rig will be able to perform prototype tests for turbines up to 300 kW and model tests for larger turbines [7]. As VKL, TTL can be run in both open and closed-loop and is equipped with two pumps of 250 kW that can be run in parallel or series. When the pumps are run in series in a closed-loop, a maximum head of 150 m is achieved. When the pumps are run in parallel in a closed-loop, the maximum flow is 0.5 m^3/s. The open-loop mode pumps the water up to the upper reservoir of 100 m^3, which is placed on top of the campus, giving a natural head of 30 m, and the lower reservoir of 300 m^3 is placed under the lab. Design data for the best efficiency point is given by technical staff at KU in Table 1.1.

Parameter	Symbol	Value	Unit
Head	H	46	m
Discharge	Q	0.233	m^3/s
Speed number	Ω	0.32	1
Inlet diameter	D_1	0.4047	m
Outlet diameter	D_2	0.25	m
Inlet height	B_1	0.0422	m
Speed	n	1000	rpm
Power at BEP	P*	95.59	kW

Table 1.1: Main dimensions of the runner at TTL.

1.3 Previous Work

Many project and master's theses have been contributing to the development of TTL, and some are mentioned in the following. In 2012, Bidhan Halwai designed a Francis model runner with hydraulic parameters similar to Jhimruk Hydroelectric Power Project in Nepal. Then, the 3D drawings he made were merged with the drawings of the pipe system at TTL [8]. In 2014, Rasmussen designed, among other things, the main shaft and the bearing block, and she started the work on an axial load and friction torque measuring device [9].

It was decided that the *Axial block spare section*, part 14 colored yellow in Figure 1.1, would become the axial load and friction torque measuring device. The forces would be measured by strain gauges placed on the surface of the cylinder wall. In 2016, Selmurzaev [10] continued the work and presented a method for calibration of the measuring device while installed in the rig. Grefstad further contributed to the development of the device in 2017 [11], such that Bådsvik could test it experimentally during her master's thesis in 2018 [12].

Bådsvik focused on the measurements of axial load and referred to the device as the Axial Load Measuring Device (ALMD). She calculated the theoretical maximum axial force the device would be applied, as a result of the hydraulic forces acting on the runner. Different wall thicknesses of the ALMD was numerically tested with Ansys Mechanical for this amount of force. As a result, she decided to experimentally test it with a wall thickness of 18 mm and 2 mm. Due to the lack of weights in the range of 200-500 kg, there were only performed load measurements in the interval of 0-200 kg and 500-700 kg. This gap in the loads was suspected of being the reason for significant hysteresis effects in the results. In the work of further development of the measuring device, Bådsvik recommended to perform load measurements with evenly applied loads and to perform a temperature calibration. [12]

The author of this thesis did perform Bådsvik's recommended actions in her project thesis, but only small improvements in uncertainties were achieved. Hysteresis was still a significant contributor to the uncertainties, and some bigger changes had to be done to improve results. Further work was suggested to include a thorough investigation of the strain gauges' unexpected behavior and other parts of the experimental setup that could cause significant uncertainties.

1.4 Objectives of this Thesis

The objective of this master's thesis is to design a measurement system for axial load and friction torque measurements to be installed at the Turbine Testing Laboratory at Kathmandu University. The measuring system has previously been called Axial Load Measuring Device (ALMD), but for the sake of this thesis, it is renamed to Axial load and friction Torque Measuring Device (ATMD). Figure 1.1 shows the assembly of the turbine, and the final design of the ATMD will replace part number 14, the axial block spare section, colored yellow in the figure. The parts in the figure are listed in Table 1.2.

First, the focus was to improve the whole system for axial load measurements so that the uncertainties were lowered. The ATMD is resting on part 20, the *Head Cover Top*, and all the axial forces working on the runner and shaft are aggregated to the device from above, leaving it to be compressed. The sources for the axial loads are the weight of the runner, shaft and other parts, and hydraulic forces. The total axial forces the ATMD will be applied is around 8500 N.

Second, the focus was to develop the ATMD further to enable measuring of friction torque as well. The ball bearing, detail B, shown in Figure 1.2a, and the cylindrical bearing, part 10 and detail C, shown in Figure 1.2b, are the sources of the friction torque the ATMD is to measure. Because the friction in such bearings is very low [13], the friction torque to measure is around 20 Nm [14].

The main challenge of this thesis is that the strain caused by the friction torque is much smaller than the strains caused by the axial force. The key is to find the balance between making the ATMD strong enough to be safe for all operation points, while maintaining the ability to measure small values without significant uncertainties in the results. The measuring device may be considered fully developed when calibration equations giving the relation between measured strain, and axial force and torque, with sufficiently low uncertainties, are obtained.

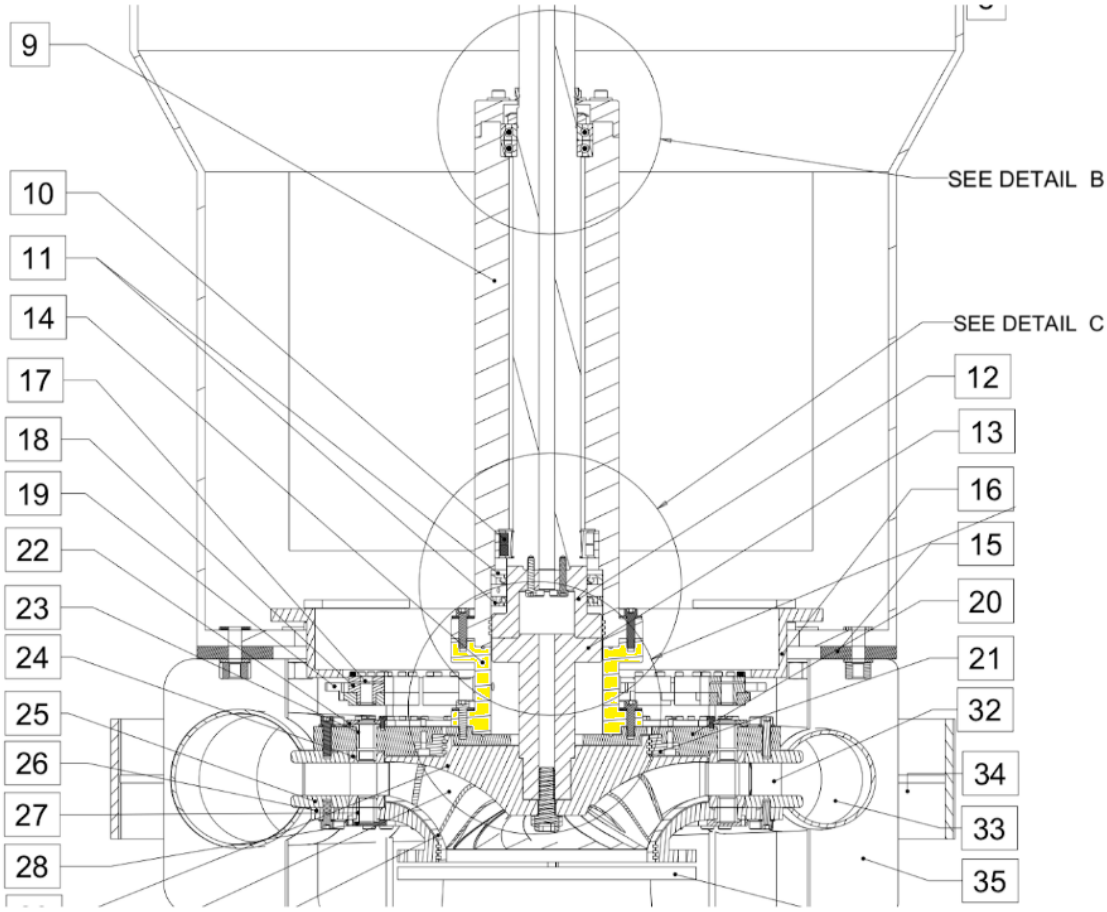

Figure 1.1: Machine drawing of the turbine at TTL and related parts, where the ATMD will replace part 14. This drawing is made by technical staff at TTL.

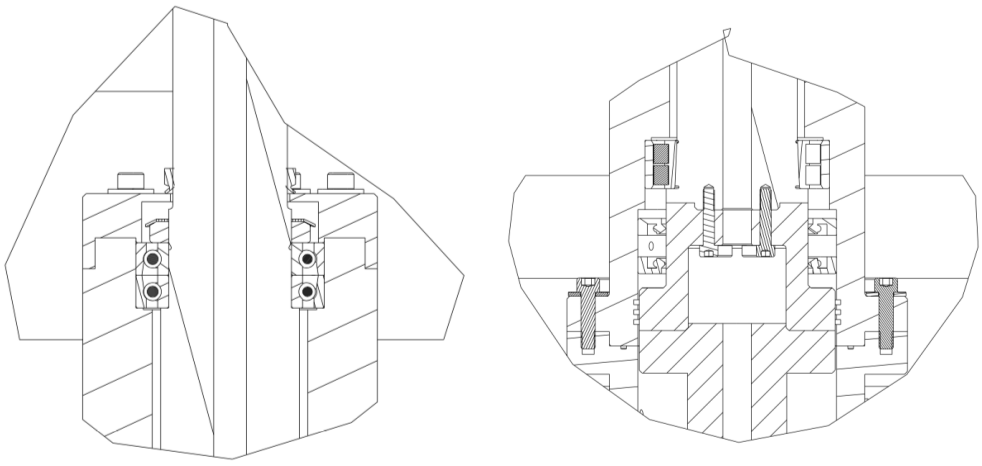

(a) Detail B: Ball bearings.

(b) Detail C: Cylindrical Bearings.

Figure 1.2: The bearings causing the friction torque.

Part number	Part name
9	Bearing housing
10	Cylindrical roller bearing
11	Shaft seal
12	Turbine intermediate shaft
13	Turbine shaft to runner
14	**Axial block spare section**
15	Turbine support spiral casing top plate
16	Guide vane control ring
17	Guide vane
18	ETP bushing
19	Guide vane control ring link
20	Head cover top
21	Head cover top labyrinth seal
22	Guide vane cover top
23	Guide vane top flange bushing
24	Guide ring
25	Stay ring
26	Stay vane support
27	Guide vane bottom flange bushing
28	Guide vane cover bottom
29	Runner Hub
30	Runner blade
31	Runner shroud
32	Stay vane
33	Spiral casing
34	Spiral casing radial supports
35	Spiral casing plate support

Table 1.2: The parts in the machine drawing, Figure 1.1.

Chapter 2

Theory

This chapter is divided into two parts. First, the theory for the forces acting on a Francis runner is presented as this is the forces the ATMD will be measuring. Then, the experimental theory is presented, giving the necessary foundation for performing experiments.

2.1 Forces Acting on a Francis Runner

This section describes the axial forces and torque working on the runner in a Francis turbine and is mostly taken from the author's project thesis, as the theoretical foundation is the same for both theses [14]. The following equations are from *Pumper og Turbiner* by Brekke [15], and the variable's subscripts are describing the variable's position. The first number in the subscript means the inlet and outlet of the runner, respectively 1 and 2. The second number means at the hub and the shroud, respectively 1 and 2. The equations will refer to vector components given in Figure 2.1.

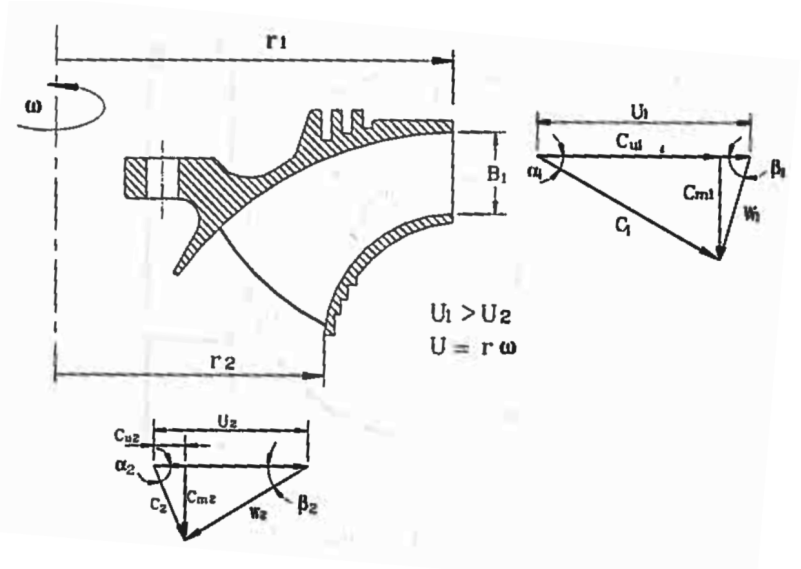

Figure 2.1: Velocity components at inlet and outlet of a turbine [15].

2.1.1 Axial Forces

The axial forces, F_1 to F_9, are shown in Figure 2.2. Pressure forces and reaction forces at the inlet and outlet of the runner are presented in the four first equations. F_1 is the force due to the difference in diameter of the hub, D_{11}, and the shroud, D_{12}, given by

$$F_1 = p_1 \cdot A_1 = \frac{1}{2} \cdot \rho \cdot g \cdot (h_{11} + h_{12}) \cdot \frac{\pi}{4} \cdot (D_{12}^2 - D_{11}^2) \qquad \text{(N)} \tag{2.1}$$

where ρ is the density of the water, g is gravitational acceleration, h is height and D is diameter. The water entering the runner at an angle $\phi \geq 0$ has an axial force component given by

$$F_2 = \rho \cdot Q \cdot c_{m1} \cdot sin\phi \qquad \text{(N)} \tag{2.2}$$

where Q is the flow rate and c_{m1} is the meridional velocity at the inlet. Note that if the water is entering the runner at an angle equal to zero, then D_{11} and D_{12} is equal, which makes both F_1 and F_2 to be zero. The force due to the pressure at the outlet of the runner is given by

$$F_3 = p_3 \cdot A_3 = \rho \cdot g \cdot h_2 \cdot \frac{\pi \cdot D_{2L}^2}{4} \qquad \text{(N)} \tag{2.3}$$

where the subscript *2L* means the lower labyrinth seal at the outlet. The reaction force at the outlet of the runner is given by

$$F_4 = \rho \cdot Q \cdot c_{m2} \qquad \text{(N)} \tag{2.4}$$

where the subscript *m2* means the meridional velocity at the outlet of the runner.

The axial forces due to the pressure between the runner and the top cover are presented in the three following equations. The force due to the pressure between the top cover and the runner hub within the labyrinth seal is given by

$$F_5 = \rho \cdot g \cdot \pi \cdot (r_p^2 - r_i^2) \cdot (h_p - \frac{k^2 \cdot \omega^2}{4 \cdot g} \cdot (r_p^2 - r_i^2)) \qquad \text{(N)} \tag{2.5}$$

where the subscript p means the position of the labyrinth's innermost radius r_p, the subscript i means at the inner radius, shown as D_r in Figure 2.2, k is a constant between 0.5 and 0.55 and ω is the angular velocity.

The force due to the pressure between the top cover and the runner hub outside of the labyrinth seal is given by

$$F_6 = \frac{\rho \cdot \pi \cdot g \cdot h_{11}}{4} \cdot (D_{11}^2 - D_{11L}^2) - \frac{\rho \cdot \pi \cdot k^2 \cdot \omega^2}{64} \cdot (D_{11}^2 - D_{11L}^2)^2 \qquad \text{(N)} \tag{2.6}$$

where D_{11} and D_{11L} are diameters both shown in Figure 2.2. The force between the top cover and the runner shroud outside of the lower labyrinth seal, is given by

$$F_7 = \frac{\rho \cdot \pi \cdot g \cdot h_{12}}{4} \cdot (D_{12}^2 - D_{12L}^2) - \frac{\rho \cdot \pi \cdot k^2 \cdot \omega^2}{64} \cdot (D_{12}^2 - D_{12L}^2)^2 \qquad \text{(N)} \tag{2.7}$$

where the diameters D_{12} and D_{12L} are also marked in Figure 2.2.

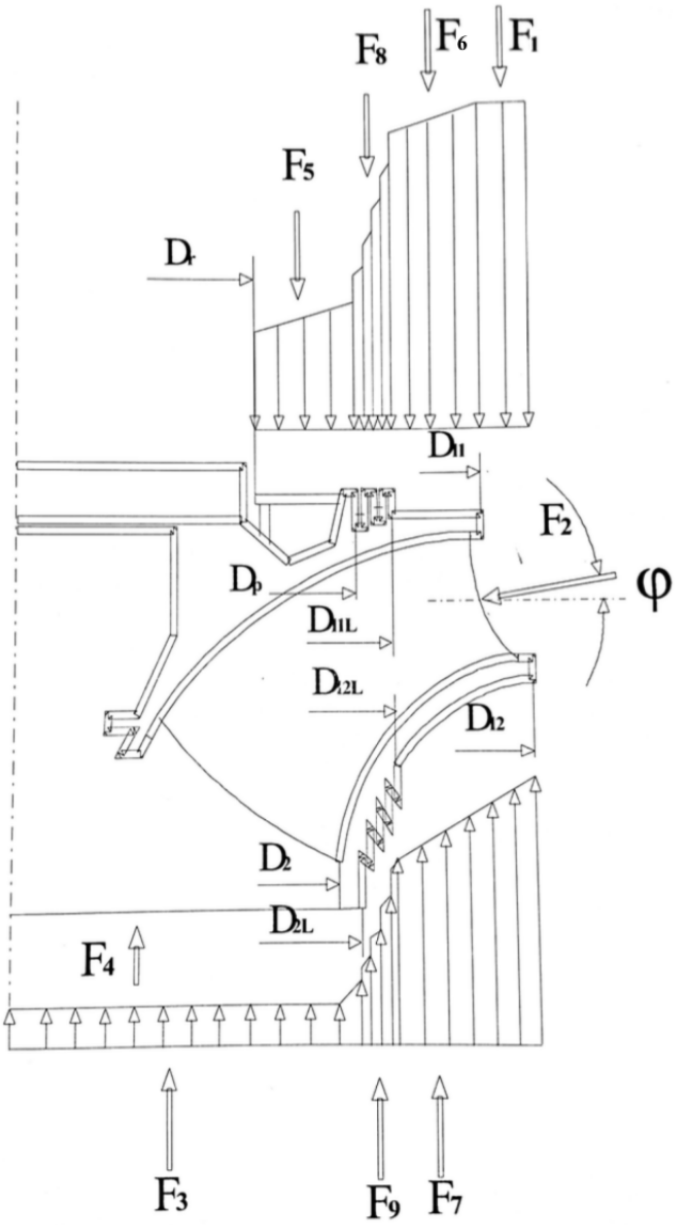

Figure 2.2: The axial hydraulic forces working on a Francis runner [15].

The axial forces due to the pressure in the labyrinth seals are presented in the two last equations. F_8 is the forces on the upper labyrinth seal

$$F_8 = p_8 \cdot A_8 = \frac{\rho \cdot g \cdot (h_{11L} + h_p)}{2} \cdot \frac{\pi \cdot (D_{11L}^2 - D_p^2)}{4} \qquad (\mathrm{N}) \tag{2.8}$$

and F_9 is the forces on the lower labyrinth seal

$$F_9 = p_9 \cdot A_9 = \frac{\rho \cdot g \cdot (h_{12L} + h_s)}{2} \cdot \frac{\pi \cdot (D_{12L}^2 - D_{2L}^2)}{4} \qquad (\mathrm{N}) \tag{2.9}$$

Note that if the turbine has vertical oriented labyrinth seals, then A_8 and A_9 equals zero, leaving F_8 and F_9 to be zero too.

Then, at last, the total axial force can be calculated by equation 2.10. Positive direction is defined as downwards as this is the desired direction.

$$F_{tot} = F_1 + F_2 - F_3 - F_4 + F_5 + F_6 - F_7 + F_8 - F_9 \qquad (\mathrm{N}) \tag{2.10}$$

2.1.2 Torque

The torque in the shaft is a result of the work the water performs on the runner and is given by

$$\vec{T_z} = \rho \cdot Q \cdot (c_{u1} \cdot r_1 - c_{u2} \cdot r_2) \qquad (\mathrm{N \cdot m}) \tag{2.11}$$

where c_{u1} and c_{u2} are the velocity vector components in the rotational direction for inlet and outlet respectively. The torque can also be written as a function of the power production.

$$\vec{T_z} = \frac{P}{\omega} \qquad (\mathrm{N \cdot m}) \tag{2.12}$$

Most of the torque is absorbed in the generator and its housing which leaves the ATMD only being exposed to the torque due to the friction in the bearings. The shaft power is given by

$$P_a = \eta_m \cdot \eta_h \cdot \eta_{vf} \cdot Q \cdot \rho \cdot g \cdot H = \eta_{tot} \cdot Q \cdot \rho \cdot g \cdot H \qquad (\mathrm{W}) \tag{2.13}$$

where η_h is the hydraulic efficiency, η_{vf} is the loss in efficiency due to leakage and disc friction. The outer mechanical losses, η_m, is the efficiency of the most interest in this thesis as this gives the friction torque.

2.1.3 Pressure and Velocity Components

To calculate the axial forces and the torque working on the shaft, the pressure at the inlet and outlet of the runner and the velocity vector components, shown in Figure 2.1, must be known.

The equation for the outlet pressure h_2 is given by

$$h_2 = h_{atm} - \frac{c_2^2}{2 \cdot g} \qquad [\mathrm{m}] \tag{2.14}$$

The equation for the inlet pressure h_1 is given by

$$h_1 = h_2 + \frac{c_2^2 - c_1^2}{2 \cdot g} + H_n \qquad [\mathrm{m}] \tag{2.15}$$

To solve the two equations above the absolute speed of the water is needed. The absolute speed of the water at inlet c_1 is given by

$$c_1 = \sqrt{c_{m1}^2 + c_{u1}^2} \qquad [\mathrm{m/s}] \tag{2.16}$$

where c_{m1} is given by

$$c_{m1} = \frac{Q}{\pi \cdot D_1 \cdot B_1} \qquad [\mathrm{m/s}] \tag{2.17}$$

Next, c_{u1} can be calculated by

$$c_{u1} = \frac{\eta_h \cdot g \cdot H_n}{u_1} = \frac{0.96 \cdot g \cdot H_n}{u_1} \qquad [\mathrm{m/s}] \tag{2.18}$$

where a hydraulic efficiency of 96% and no swirl at the outlet at BEP is assumed. When also assuming continuity, equation 2.18 is valid for all operation points.

The aboslute speed of the water at the outlet, c_2, is given by

$$c_2 = \sqrt{c_{m2}^2 + c_{u2}^2} \qquad [\mathrm{m/s}] \tag{2.19}$$

where c_{m2} is given by

$$c_{m2} = \frac{Q}{\pi \cdot D_2^2/4} \qquad [\mathrm{m/s}] \tag{2.20}$$

and, c_{u2} is given by

$$c_{u2} = u_2 - \frac{c_{m2}}{tan(\beta_2)} \qquad [\mathrm{m/s}] \tag{2.21}$$

The outlet blade angle, β_2, is constant for all operational points, and can be calculated by

$$\beta_2 = tan^{-1}(\frac{c_{m2,BEP}}{u_2}) \qquad [\mathrm{deg}] \tag{2.22}$$

The blade velocity at inlet u_1 and outlet u_2 is given by

$$u_i = \omega \cdot \frac{D_i}{2} \qquad [\mathrm{m/s}] \tag{2.23}$$

2.2 Experimental Theory

This section describes the theoretical foundation for the experimental work.

2.2.1 Stress and Strain in a Solid Body

As a result of forces working on a solid body, stress and strain occur in the material. The three following equations are from *Konstruksjonsmekanikk* by Bell [16]. Normal strain ϵ is defined as the relative change in length in the axial direction, given by

$$\epsilon = \frac{\Delta L}{L_0} \qquad [-] \tag{2.24}$$

The normal stress σ in a solid body is defined as the normal force N divided by the body's cross section area A, given by

$$\sigma = \frac{N}{A} \qquad [\mathrm{Pa}] \tag{2.25}$$

For linear elastic materials, like steel, Hooke's law describes the linear relationship between the stress and strain and is given by

$$\epsilon = \frac{\sigma}{E} = \frac{N}{A \cdot E} \qquad [-] \tag{2.26}$$

where E is Young's Modulus for the material.

2.2.2 Strain Gauges

Strain gauges mounted on the surface of a solid body that is compressed or stretched can measure the strain through the change in length of the wires causing the resistance to change [17]. Strain gauges are often arranged in a Wheatstone bridge as this configuration is well suited for measuring changes in resistance [18]. Figure 2.3 shows the schematic of a full Wheatstone bridge.

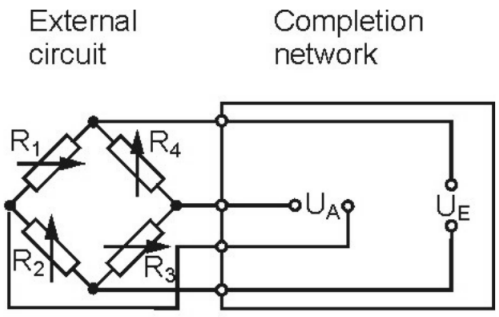

Figure 2.3: Strain gauges arranged in a full Wheatstone bridge [18].

The following equations are from the article *Applying the Wheatstone Bridge circuit* by Karl Hoffman [18]. When the strain gauges are arranged as in Figure 2.3 a linear relationship between the relative change in resistance and strain is obtained, given by

$$\frac{\Delta R}{R_0} = GF \cdot \epsilon \qquad [-] \tag{2.27}$$

where GF is the Gage Factor, a characteristic depending on the specific strain gauge.

The equation

$$\frac{U_A}{U_E} = \frac{R_1}{R_1 + R_2} - \frac{R_4}{R_3 + R_4} = \frac{R1 \cdot R_3 - R_2 \cdot R_4}{(R_1 + R_2) \cdot (R_3 + R_4)} \qquad [-] \tag{2.28}$$

is valid for a bridge with strain gauges that is initially balanced, which means

$$\frac{U_A}{U_E} = 0 \qquad [-] \tag{2.29}$$

when

$$R_1 = R_2 = R_3 = R_4 \qquad [\Omega]$$

or

$$\frac{R_1}{R_2} = \frac{R_4}{R_3} \qquad [-]$$

When R_1 to R_4 are exposed to strain, the bridge is no longer balanced and U_A is non-zero. With the assumption that the deviation in resistance, ΔR_i, is much smaller than the resistance itself, R_i, second-order factors can be neglected and equation 2.28 can be written as

$$\frac{U_A}{U_E} = \frac{1}{4} \cdot (\frac{\Delta R_1}{R_1} - \frac{\Delta R_2}{R_2} + \frac{\Delta R_3}{R_3} - \frac{\Delta R_4}{R_4}) \qquad [-] \tag{2.30}$$

By substituting equation 2.27 into equation 2.30 we get the relation between the change in voltage and applied strain

$$\frac{U_A}{U_E} = \frac{GF}{4} \cdot (\epsilon_1 - \epsilon_2 + \epsilon_3 - \epsilon_4) \qquad [-] \tag{2.31}$$

There are several ways of arranging the strain gauges depending on the desired measurand. For measuring axial strain, the arrangement is as in Figure 2.4. With this arrangement the strain gauges only give output due to axial load, any torque load or extension of the wires due to a temperature rise will be canceled out [19]. Note that the figure is demonstrating tension while the ATMD will be applied compression. The direction of the axial force *F* only affects the sign of the strain output and the principle is the same for positive and negative axial forces. For measuring compression, ϵ_1 and ϵ_3 will be negative, and ϵ_2 and ϵ_4 will be positive, and equation 2.31 becomes

$$\frac{U_A}{U_{E\,Compression}} = \frac{GF}{4} \cdot (-|\epsilon_1| - |\epsilon_2| - |\epsilon_3| - |\epsilon_4|) \qquad [-] \tag{2.32}$$

In most cases, ϵ_1 and ϵ_3 are the values of interest as strain gauge number 1 and 3 are the ones placed in the same direction as the applied forces. Poisson's Ratio ν is a material constant describing the

material's change in length perpendicular to the direction of the force, and is usually around 0.3 for metals. For a purely axial compression, we have $\epsilon_1 = \epsilon_3 = \epsilon$ and $\epsilon_2 = \epsilon_4 = \nu \cdot \epsilon$, by using this we can rewrite equation 2.32 to

$$\begin{aligned} \frac{U_A}{U_{E\,Compression}} &= \frac{GF}{4} \cdot (-|\epsilon| - |\nu \cdot \epsilon| - |\epsilon| - |\nu \cdot \epsilon|) \\ \frac{U_A}{U_{E\,Compression}} &= -\frac{GF \cdot |\epsilon|}{4} \cdot (2 + 2 \cdot \nu) \qquad [-] \end{aligned} \tag{2.33}$$

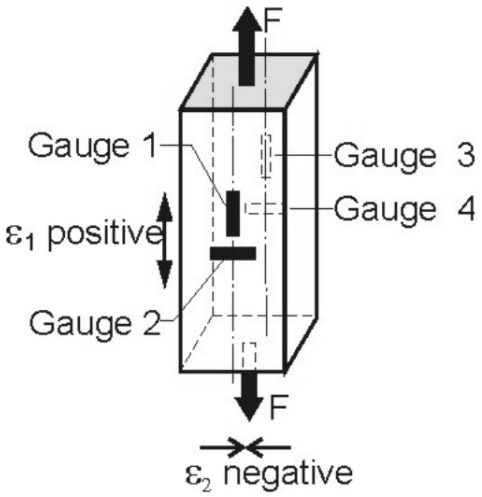

Figure 2.4: Arrangement of strain gauges measuring axial forces [18].

For measuring torque the strain gauges are arranged as in Figure 2.5. With this arrangement the strain gauges only give output caused by torque, any axial load or extension due to temperature rise, will be canceled out [19]. In the figure a clockwise torque is applied, meaning the left side of the beam is held fixed and a clockwise twist is applied on the right side of the beam. This causes strain gauge 1 and 3 to experience positive strain and strain gauge 2 and 4 to experience negative strain. In most practical cases for torque measurement, pre-positioned strain gauges, arranged as a fishtail, are used to make sure the strain gauges are exactly 45°. The absolute value of $|\epsilon_1| = |\epsilon_2| = |\epsilon_3| = |\epsilon_4| = \epsilon$ which reduces equation 2.31 to

$$\begin{aligned} \frac{U_A}{U_{E\,Torque}} &= \frac{GF}{4} \cdot (|\epsilon| - (-|\epsilon|) + |\epsilon| - (-|\epsilon|)) \\ \frac{U_A}{U_{E\,Torque}} &= GF \cdot \epsilon \qquad [-] \end{aligned} \tag{2.34}$$

Since the equations for change in voltage for axial and torque load applied, respectively equations 2.33 and 2.34, only consist of one unknown value ϵ, this value is possible to derive. The change in voltage in the bridge U_A is measureable, and the the exitation voltage U_E, the gage factor GF, and the Poisson's Ratio ν are known.

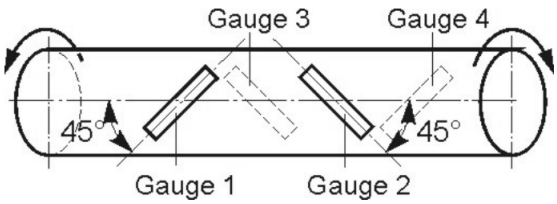

Figure 2.5: Arrangement of strain gauges measuring torque [18].

2.2.3 Uncertainty

This subsection is partly taken from the author's project thesis [14] as the uncertainty analysis is performed in the same matter in both theses.

Uncertainties are divided into two parts: systematic and random. The systematic error is caused by the experimental setup and the measuring devices used, never being exactly accurate. The following equations describing systematic errors are published by German Calibration Service in *Calibration of Pressure Gauges* [20]. The first number in the subscript is referring to a total of six measurement series. Each measurement session is done in pairs, first on-loading (number 1, 3, and 5) and then off-loading (number 2, 4, and 6), where measurement series 1 and 2 are one pair of on-loading and off-loading, etc. The second subscript in the equations refers to a measurement point within a measurement series. In the equations where the second subscript is *j*, then the uncertainty is different for each measurement point. The unit in the three following equations is not specified as it depends on the unit of the measurements, which is μstrain in this thesis.

A systematic error highly relevant in this thesis is hysteresis, as this was the main challenge in earlier performed measurements. Hysteresis is occurring when the output of a variable has a different value when the variable is increasing and decreasing, see Figure 2.6, and are calculated by

$$h_{mean} = \frac{1}{n_x} \cdot \big(|(x_{2,j} - x_{1,0}) - (x_{1,j} - x_{1,0})| + |(x_{4,j} - x_{3,0}) - (x_{3,j} - x_{3,0})| + |(x_{6,j} - x_{5,0}) - (x_{5,j} - x_{5,0})| \big) \tag{2.35}$$

where n_x is the number of measurement pairs, which is three for a set of six measurement series.

Another systematic error is the deviation in output at zero loads for the different measurement series, called zero deviation. It is defined as the maximum deviation of the measured value at zero loads for one on-loading and the corresponding off-loading, and is calculated by

$$f_0 = max\big(|x_{2,0} - x_{1,0}|, |x_{4,0} - x_{3,0}|, |x_{6,0} - x_{5,0}|\big) \tag{2.36}$$

Repeatability is the error that describes how much the results at one point deviates within the different measurement series. The repeatability for each measurement point *j* is given by

$$\begin{aligned} b'_{up,j} &= |(x_{3,j} - x_{3,0}) - (x_{1,j} - x_{1,0})| \\ b'_{down,j} &= |(x_{4,j} - x_{4,0}) - (x_{2,j} - x_{2,0})| \\ b'_{mean,j} &= max(b'_{up,j}, b'_{down,j}) \end{aligned} \tag{2.37}$$

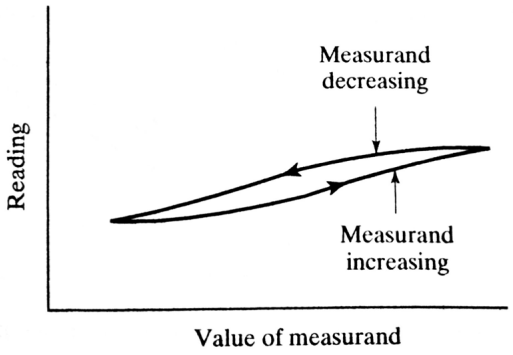

Figure 2.6: The principle of hysteresis [17].

Random errors will occur when gathering data in big samples. By assuming the data points of a measurement have a Gaussian distribution, the random uncertainty can be calculated by

$$w_{\bar{x}} = t \cdot \frac{S_x}{\sqrt{n_{S_x}}} \qquad [-] \tag{2.38}$$

where S_x is the standard deviation of the sample and n_{S_x} is the size of the sample. The number t is the Student's t-distribution number which is obtained from tables and is a function of the degree of freedom and the desired confidence interval. In this thesis, the confidence interval used for the random uncertainty is 95%.

When dealing with a variable that depends on several uncertain values, it is not very likely that all terms become simultaneously high or low. Summing up all the uncertainties give unreasonably high estimates. Calculating the *Root of the Sum of the Squares* (RSS) is a more used method for the total uncertainty [17], and is given by

$$w_R = \left(\sum_{i=1}^{n} \left[w_{x_i} \cdot \frac{\delta R}{\delta x_i} \right]^2 \right)^{\frac{1}{2}} \qquad [-] \tag{2.39}$$

where w_R is the total uncertainty for the result variable R and w_{x_i} is the uncertainty of variable x_i. The term, $\frac{\delta R}{\delta x_i}$, is the relation between a small change in the result variable R and a small change in variable x_i. If a change in x_i have a direct impact on the result variable R, $\frac{\delta R}{\delta x_i}$ is equal to one.

Chapter 3

Process

This chapter is divided into three parts. First, previous work is evaluated to ensure progress in the development of the measuring device. Second, a new design of the measurement device is developed so that it can measure both axial load and friction torque. Then third, the experimental process is described.

3.1 Evaluation of Previous Work

The strain gauges previously used was Kulite Semiconductor S/UCP-090-120, and their strain output for axial load applied is shown in Figure 3.1. Note that the repeatability in the measurements are so good that the blue series is plotted over the red and green series in the figure. The hysteresis effects, on the other hand, are severe. The general opinion of the lab technicians at VKL and according to the manufacturer and supplier, these types of strain gauges should be giving better results than obtained [21]. It was assumed that the adhesive or poor mounting must have been the reason for the big hysteresis effects even though the mounting was done by an experienced technician with apparently the correct adhesive. When the ATMD is complete, it must be installed by the staff at TTL themselves. If the mounting of the semiconductor-type strain gauge is so sensitive that not even an experienced lab technician can do it correctly, then this is not the strain gauges to recommend KU. It was therefore decided to test other types.

The amount of strain measured by the Kulite Semiconductor strain gauge type when the ATMD was applied 700 kg was known to be about 16 μstrain and the corresponding numerical calculated strain was about 24 μstrain [14]. One of the students previously working on the ATMD had mounted some traditional HBM pre-wired strain gauges on a steel bar and it was decided to test these strain gauges for the same amount of strain to check the uncertainties of their output. The desired strain was around 25 μstrain, the bar's cross-section was 2 cm^2 and the material's Young's Modulus was around 200 GPa. The amount of force to apply the bar was calculated with Hooke's law, equation 2.26, to be around 100 kg. The bar was tested numerically in Ansys Mechanical with an axial load of 100 kg applied to give a numerical strain of 25 μstrain.

The bar was then tested experimentally for axial loads with a hanging system of 5 kg in steps of 20 kg up to 105 kg in total weight applied, and the output is shown in Figure 3.2. The traditional

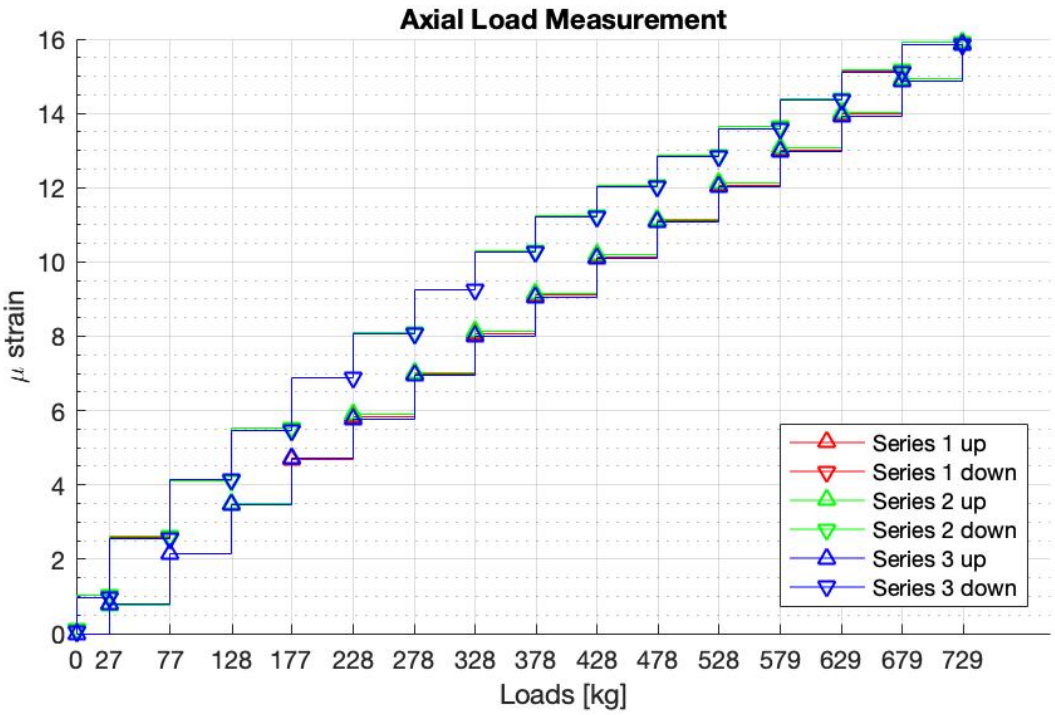

Figure 3.1: Output from the Kulite Semiconductor strain gauges when applied axial load.

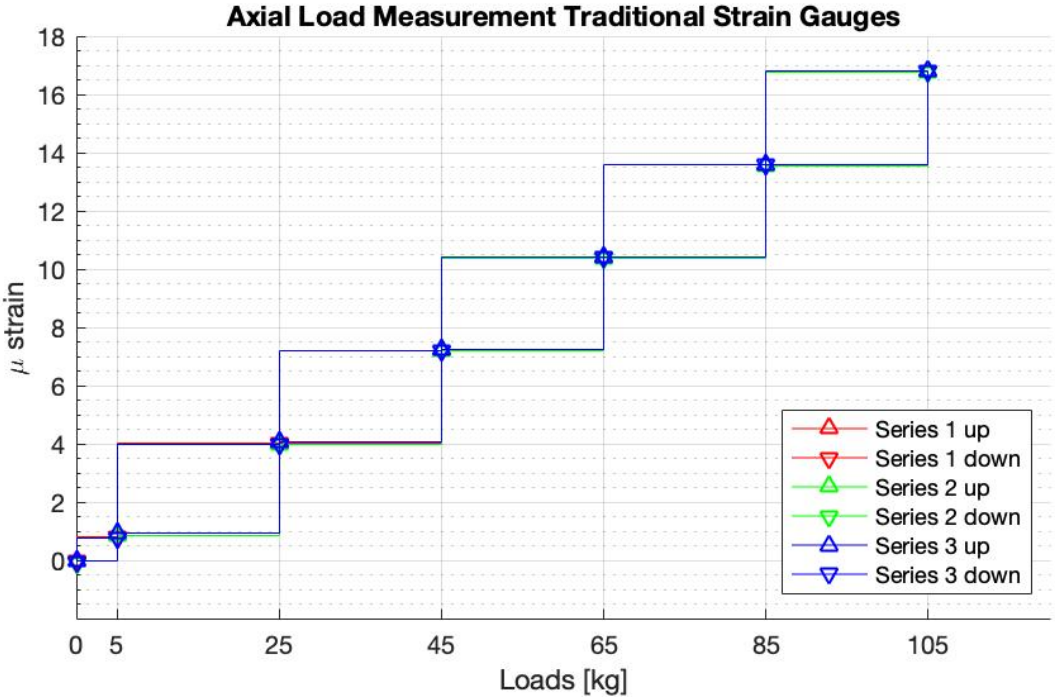

Figure 3.2: Output from the traditional strain gauges when applied axial load.

strain gauges, that was mounted by the inexperienced student herself, show much less hysteresis and are much more linear than the earlier used strain gauges shown in Figure 3.1. It was concluded to use strain gauges like these in the further development of the measurement device. The advantage with traditional strain gauges is that they are cheaper than the semiconductor-type and the pre-wired types are easier to mount by someone inexperienced. The disadvantage with the pre-wired type is that they do not exist in a fishtail configuration, the type that is most used for torque measurements. Still, it was decided to use traditional pre-wired strain gauges and to be precise when mounting the diagonal strain gauges in 45°.

3.2 Geometrical Change Through Numerical Analysis

Since new experimental data collection had to be performed to test the new strain gauges, it was decided to also do some bigger changes to the geometry of the ATMD to enable measuring of friction torque as well. By cutting holes in the middle part of the ATMD it was believed that the strain as a result of solely applied torque would be big enough to measure. What kind of holes to choose was decided through numerical analysis. The axial forces the shaft will be applied during operation in the Francis Rig at KU was calculated by Bådsvik [12], and is given in Table 3.1. The maximum amount of friction torque transferred to the ATMD was calculated by this thesis's author's project thesis to be 20 Nm [14] .

	F_1[N]	F_2[N]	F_3[N]	F_4[N]	F_5[N]	F_6[N]	F_7[N]	F_8[N]	F_9[N]	F_{tot}[N]
BEP	0	0	-5198	-1106	4804	24 490	-22 528	0	0	461
Q_{Max}	0	0	3667	-5093	4804	43 840	-40 250	0	0	6968

Table 3.1: Axial forces F_i in the turbine at TTL due to hydraulic forces [12]. Positive direction is defined as downwards.

The new geometrical design had two main requirements: first, the ATMD must be strong enough to be safe for all operation points meaning the maximum stress should never exceed 80% of the yield strength, and second, it must be flexible enough to be able to measure the small friction torque values. As seen in the previous section, a bar with old fashioned metal wire strain gauges had satisfactory linear experimental results with no signs of hysteresis for a strain interval of 0-17 μstrain, and the corresponding numerically calculated strain was 25 μstrain. It was therefore decided to find a design of the ATMD that gave numerically calculated strain as high as possible, preferably around 25 μstrain, for solely 20Nm torque applied.

Before any geometrical changes were performed, the ATMD had a wall thickness of 2 mm, two circular holes through the wall for the drainage of labyrinth seal water, and four flattened sections at the wall where the old strain gauges were attached, see Figure 3.3. Downsizing the ATMD to a wall thickness of 1 mm would almost halve the cross-section area and increase the strain values, and could have been a good basis for further investigation. Even so, this alternative was considered to be practically difficult because the smallest wall thickness at the flattened sections was 0.72 mm, meaning that if this version had got 1 mm wall thickness, there would be six holes in the wall. It was therefore decided to investigate different designs of 2 mm wall thickness.

Figure 3.3: Flattened sections of the ATMD and the previous used semiconductor strain gauges.

First, the ATMD were numerically tested for different materials with the use of Ansys Mechanical. For all the materials tested: copper, aluminum, bronze, and stainless steel, it was concluded that a change in the material would not give big enough strains and that holes in the wall were necessary. By the use of CAD-drawing in Creo Parametric different designs of the ATMD were constructed and then numerically tested. In this process, 31 different designs were investigated, and the holes ranged from straight, diagonal, circular, oval, ellipse, big and small, see Figure 3.4 for a selection of the investigated designs. Vertically oriented holes were considered, but the 2 mm wall thickness limitation gave that not even the design in the lower left in Figure 3.4 were giving big enough strains when solely applied torque. The lower right model in Figure 3.4 were the chosen design, as this design combines two weak points in the upper and lower circular part of the slotted holes and form a larger area with bigger strain values. Figure 3.5 shows the numerical results of solely 20 Nm torque applied giving 19 μstrain in the area where the strain gauges would be mounted. Getting higher maximum strain without getting too close to the 80% of yield strength limit turned out to be difficult.

The final design of the ATMD that was meant for Kathmandu University, from now on called the *KU-version*, is not geometrically identical to the version of the ATMD on which the experiments were performed, from now on called the *experimental version*. Due to a miscommunication with the lab technician machining the holes, the experimental version ended up having holes of 25 mm width, see Figure 3.6, while the KU-version was planned to have 20 mm width, see Figure 3.7. Another difference is that the experimental version is made of st52 steel and has the four flattened sections, while the KU-version will not have these flat areas and are planned to be made of stainless steel 316.

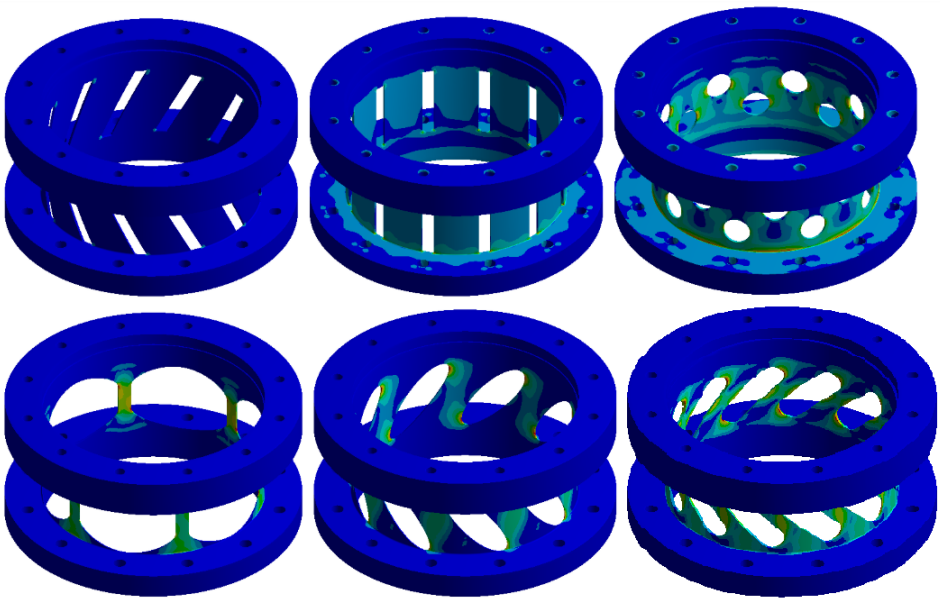

Figure 3.4: A selection of the investigated designs.

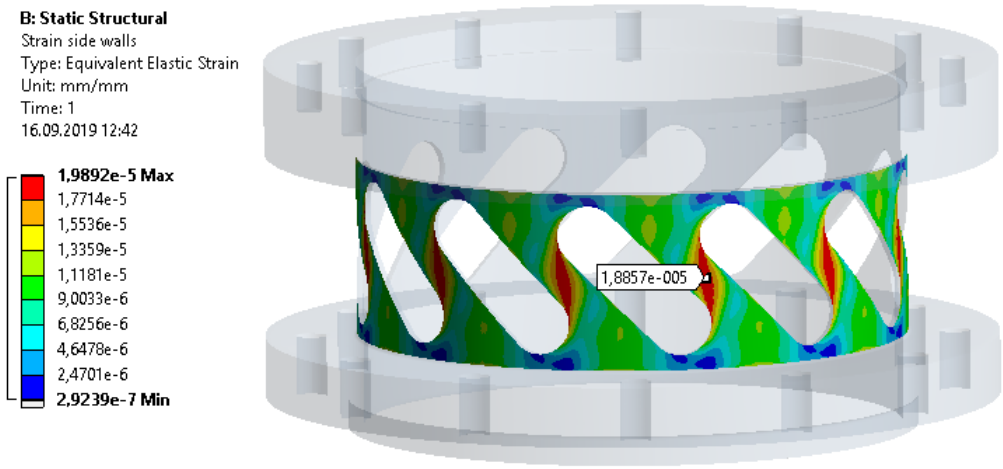

Figure 3.5: The design combines two weak spots into a larger area of bigger strain values. At the strain gauge's position, there is 19 μstrain for 20 Nm applied torque.

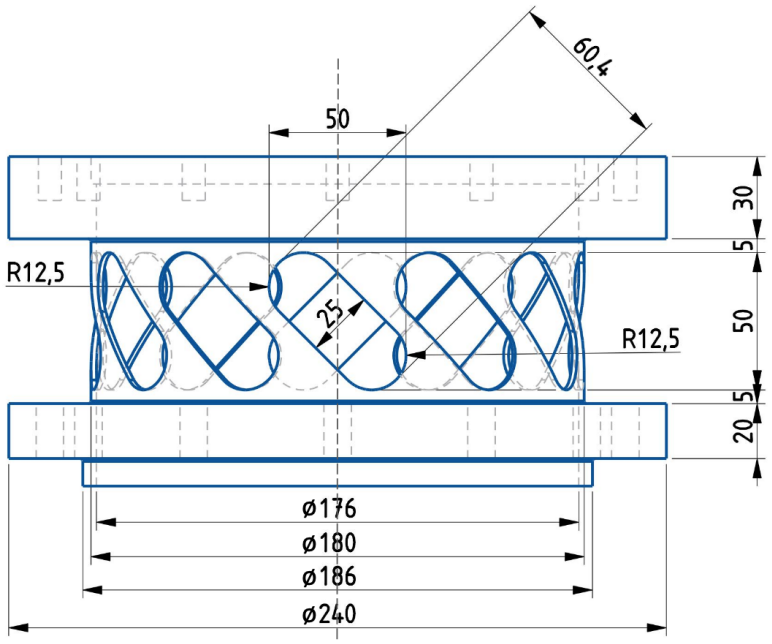

Figure 3.6: Design of the experimental version of the ATMD with dimensions in millimeter.

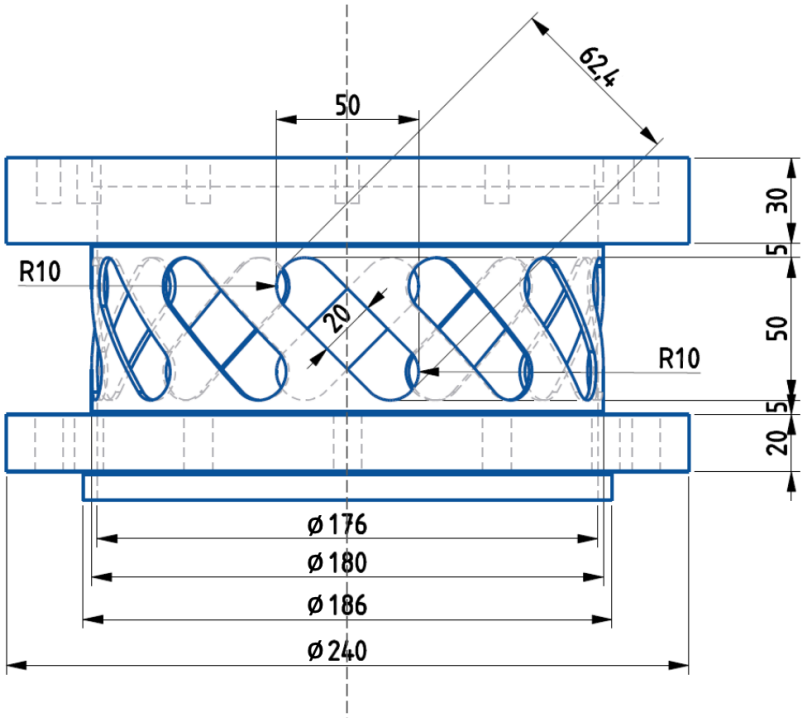

Figure 3.7: Design of the KU-version of the ATMD with dimensions in millimeter.

Due to the geometrical and material differences, the resulting strain will be different for the same amount of force. Considering the materials, the experimental version is the stronger one as st52-steel has 355 MPa in yield strength [22], and stainless steel 316 is having 205 MPa in yield strength [23]. Considering the geometry, the bigger holes and the flat thin parts of the experimental version makes the KU-version the strongest. Table 3.2 shows that the KU-version is in total the stronger one. To achieve the same amount of strain, the axial forces should be reduced to 69% and the torque to 73%. Table 3.3 presents the average strain at the strain gauge's position for the adjusted forces applied to the experimental version, showing that the adjustments are making the two versions comparable. In Table 3.2 and Table 3.3, case 1 is referring to the maximum amount of axial forces and friction torque the ATMD will be applied, case 2 is the maximum axial hydraulic forces and friction torque, case 3 is only the maximum friction torque and case 4 is only the maximum axial hydraulic forces.

Case	Axial force [N]	Torque [Nm]	Average strain at SG-point		Strain in KU-version compared to experimental [%]
			KU-version [μstrain]	Experimental version [μstrain]	
1	-8500	-20	440	640	69
2	-7000	-20	360	530	68
3	0	-20	19	26	73
4	-7000	0	350	510	69

Table 3.2: Numerical analysis of the experimental version and KU-version.

Case	Axial force 69% [N]	Torque 73% [Nm]	Average strain at SG-point [μstrain]	Strain in KU-version compared to experimental [%]
1	-5865	-14.6	441	100
2	-4830	-14.6	365	99
3	0	-14.6	18.9	101
4	-4830	0	352	99

Table 3.3: Numerical analysis of the experimental version for adjusted forces.

For both versions, it was necessary to make sure that the amount of stress would not exceed 80% of the yield strength for the maximum applied forces, case 1 in Table 3.2 and Table 3.3. The maximal numerical calculated stress applied to the experimental version is 253 MPa, which is around 71% of the yield strength of 355 MPa for the st52-steel type. For the KU-version, the maximum stress was calculated to be 157 MPa, which is 76% of the yield strength of 205 MPa for stainless steel 316.

The theory behind constructing a good mesh such that reliable numerical results are obtained are described in appendix A. One of the actions performed is a mesh independent test to make sure

the calculated values were correct. A deviation of 1% was found in the maximum stress calculation and was considered small enough to regard the numerical results as mesh independent.

3.3 Experimental Data Collection

After the two versions of the ATMD had been tested numerically to be safe for the amount of forces to apply, it was time to test the experimental version in the lab. This section describes the necessary preparations for the experiments and the procedure in the data collection.

3.3.1 Preparations of Experiments

After the ATMD had gotten diagonal slotted holes through the walls, the eight new strain gauges were attached. Four of them were arranged as in Figure 2.4 for the axial load measurements, and this group was named vertical-SGs. The other four were arranged as in Figure 2.5 for the torque measurements and were named diagonal-SGs. The strain gauges used are from Tokyo Measuring Instruments Lab (TML) and have a gauge resistance of 119.8 $\pm$ 0.5 Ω, a gauge factor of 2.15 $\pm$ 1%, and a gauge length of 1 mm [24]. The strain gauges were initially cabled in a full Wheatstone bridge and calibrated within LabView as described by National Instruments in *Connecting Strain Gages to a DAQ Device* [25]. This calibration removes the null point offset, making sure the first measurement is close to zero for no load applied.

The experimental setup for axial load measurements was arranged such that the ATMD was compressed, see Figure 3.8 for a schematic. Upon the ATMD, a circular cover was placed where the hanging system was attached to the exact center. This was important because if the weights were applied slightly off-center, the weight would not be evenly distributed in the walls of the ATMD, and the strain gauges would give the wrong output.

For the torque load measurements, the ATMD was hanged in a stable frame, and an arm of 15 cm was attached underneath, see Figure 3.9 for schematic. The hanging system consisted of a thin wire and a metal plate with a total weight of 0.6515 kg. All the weight plates used were either calibrated by Justervesenet or calibrated during the work of this thesis' author's project thesis [14].

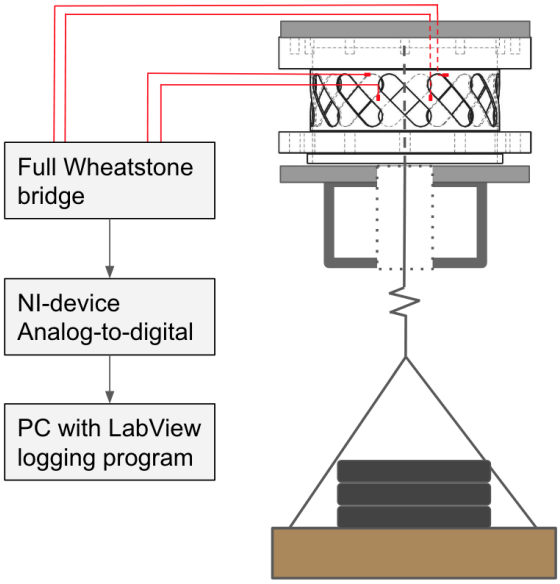

Figure 3.8: Drawing of the experimental setup for axial load measurements.

The equipment used in the axial load data collection:

- The ATMD
- Strain gauges attached to the ATMD cabled in a full Wheatstone bridge
- A temperature probe taped to the surface of the ATMD
- Some isolating material to cover the strain gauges and temperature probe
- A strong beam with a hole between the top and bottom
- Hanging system
  - Top cover plate with screws
  - A hook
  - Lever hoist
  - Straps
  - Pallet
- Weight plates
  - 20 weight plates of 10 kg
  - 12 weight plates of 25 kg
  - 38 weight plates of 5 kg
  - 5 weight plates of 2 kg
- NI-devices converting analog signals from the strain gauges to digital signals
- PC with LabView program for logging
- Matlab for post-analysis

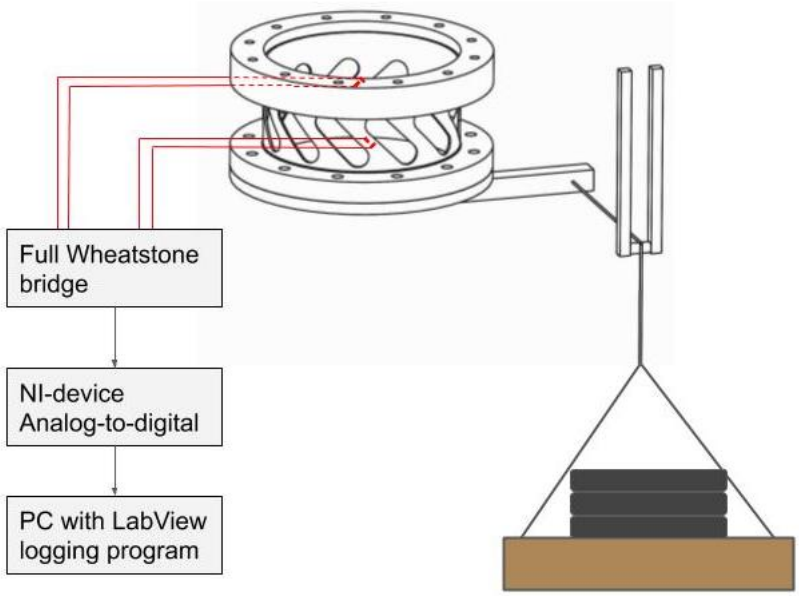

Figure 3.9: Drawing of the experimental setup for torque measurements.

The equipment used in the torque load data collection:

- The ATMD
- Strain gauges attached to the ATMD cabled in a full Wheatstone bridge
- A temperature probe taped to the surface of the ATMD
- Some isolating material to cover the strain gauges and temperature probe
- A stable frame to hang the ATMD from
- Hanging system
  - An arm attached underneath the ATMD
  - Plate to place weights
  - Wire to attach to the arm and plate
  - Pulley on which the wire can slide frictionless
- 5 weight plates of 2 kg
- NI-devices converting analog signals from the strain gauges to digital signals
- PC with LabView program for logging
- Matlab for post-analysis

3.3.2 The Data Collection

The procedure in collecting axial load measurement data is based on Bådsvik's original procedure [12], which she partly based on the guideline for calibrating pressure gauges from the German Calibration Service [20]. As part of the planning of the procedure, a risk assessment was performed.

At the beginning of every measurement session, a measurement without any load, not even the hanging system, was performed for later to be able to compensate for a possible zero-point drifting. Each measurement session contained a pair of on-loading and off-loading measurement series. For the axial load data collection, the first on-loading measurement was of the hanging system of 37 kg, then 50 kg was added in 12 steps, adding up to a total of 637 kg. Then all the weights were removed in LIFO-order, meaning last in first out. Every recording was done in one minute, and the hanging system had to be still and undisturbed during that time.

The data collection of torque load was performed in the same matter. The first on-loading torque measurement was of the hanging system of 0.6515 kg, giving a torque of 0.96 Nm. Then weights of 2 kg were added in 5 steps, adding up to a total of 10.6515 kg, which is 15.67 Nm. The complete procedure was performed three times to be able to investigate the repeatability of each measurement point.

During the data collection, the temperature on the surface of the ATMD was also collected. The arrangement of the strain gauges should be temperature-compensating [19]. However, if it does not work as expected, it would be necessary to know the surface temperature to be able to perform a temperature compensation afterwards. The output from the strain gauges and the temperature probe was, through an analog-to-digital-device, provided to LabView, which wrote the data to .txt-files. Then Matlab was used for analysis, as discussed in the following chapter.

Chapter 4

Results of the Experiments

This section presents and discusses the results of the experiments performed, where three test cases were investigated. The goal was to obtain two independent sources of strain data to relate to the two unknowns the system is to measure, axial load and friction torque.

The output from the full-bridge vertical-SGs of test case 1 had sufficiently low uncertainties and was kept in all the test cases as the first source of strain data. Test case 2 and 3 were performed to find a better second source of strain data than the full-bridge arrangement of diagonal-SGs in case 1. An arrangement with low uncertainties for both axial load and torque load, or low uncertainty for one of the loads while close to zero output for the other, would be a good second source.

4.1 Case 1: Vertical-SG and Diagonal-SG both in Full-bridge

The first case to be investigated was the original setup with the vertical-SGs and diagonal-SGs arranged in two separate full Wheatstone bridges. The output from the two sets of strain gauges is first presented for the axial load applied, then for the torque applied.

4.1.1 Axial Load Applied

Output From Vertical-SGs

The temperature development during the measurements of axial load applied is shown in Figure 4.1 and the strain measured by the vertical-SGs is shown in Figure 4.2. These strain gauges are arranged in a way such that they should compensate for temperature change [19]. It seems to be working as the blue measurement series is the warmest measurement, and the strain measured lies in between the other measurement series.

Figure 4.3 is presenting the different uncertainty-types. The uncertainty due to repeatability is the biggest contributor to the lower load measurements. Zero deviation and hysteresis being low for all loads is an improvement compared to the earlier used strain gauges [14], which had hysteresis effects as shown in Figure 3.1. The random uncertainty in the data acquisition is neglected throughout the whole thesis as it is about 0.01 μstrain, which is 1% the size of the other uncertainties. The total uncertainty is calculated by using the *Root of the Sum of the squares* method (RSS).

The total absolute uncertainty is presented in Figure 4.4 and the total relative uncertainty is presented in Figure 4.5. Based on the measured values, a linear best fit line with an upper and lower uncertainty band of the total uncertainty is plotted in Figure 4.6.

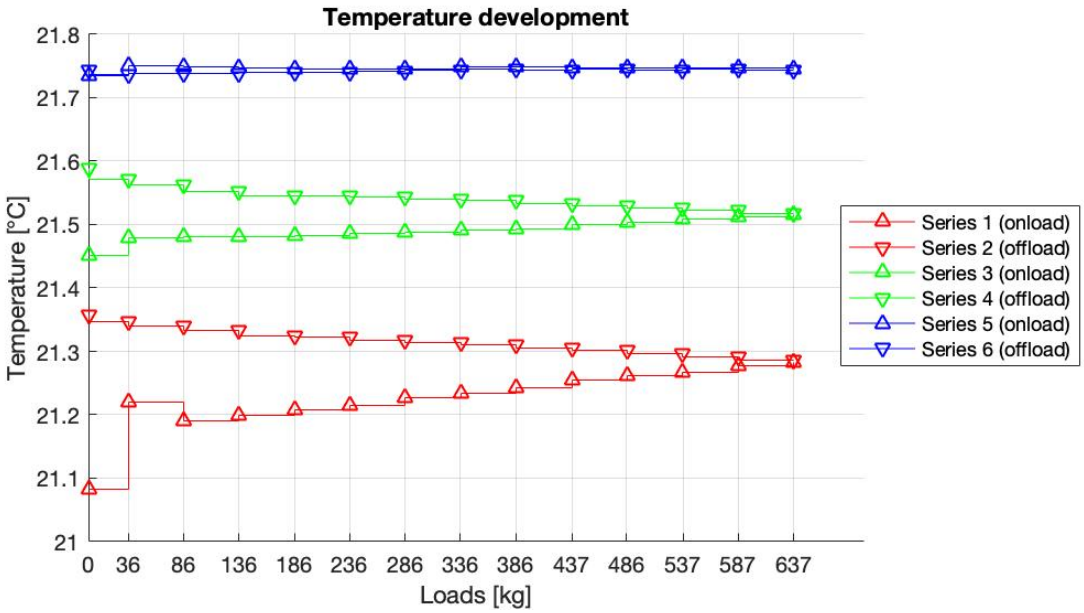

Figure 4.1: Case 1: Temperature development during axial load applied.

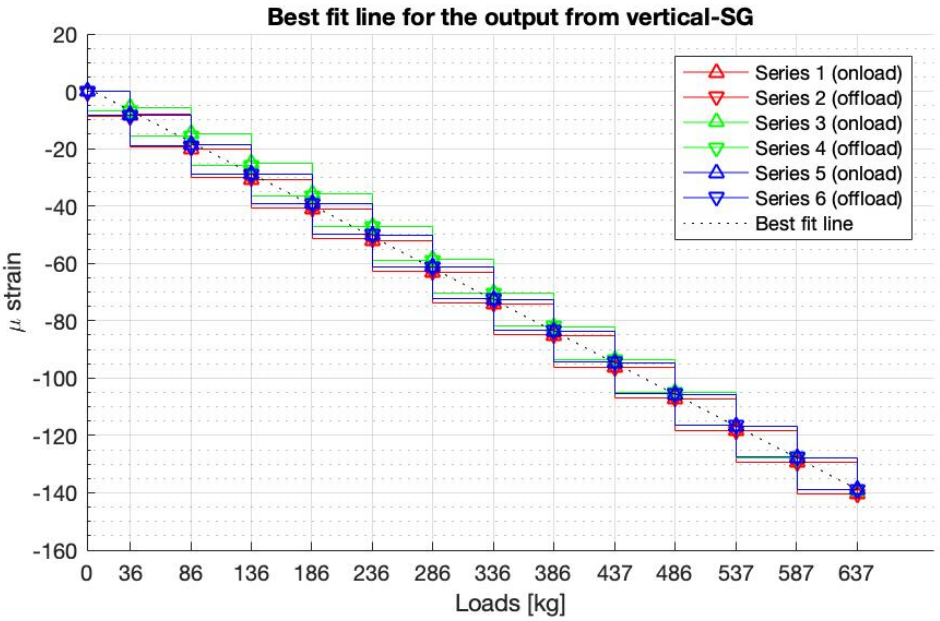

Figure 4.2: Case 1: Measured strain by vertical-SGs during axial load applied.

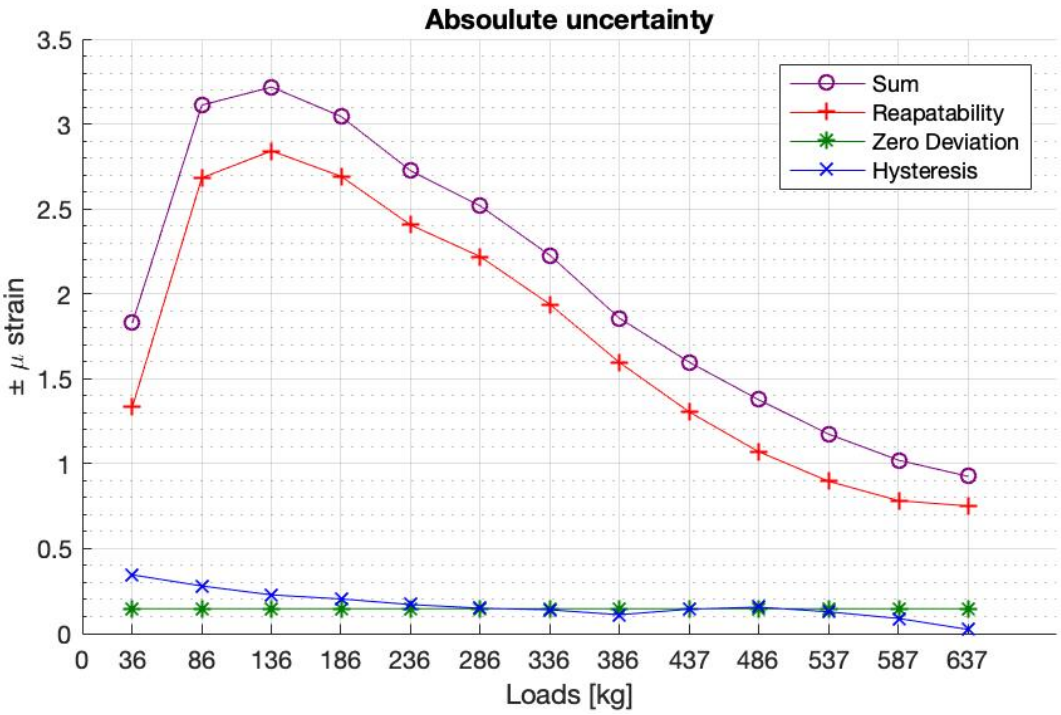

Figure 4.3: Case 1: Uncertainties in the output from the vertical-SGs applied axial load.

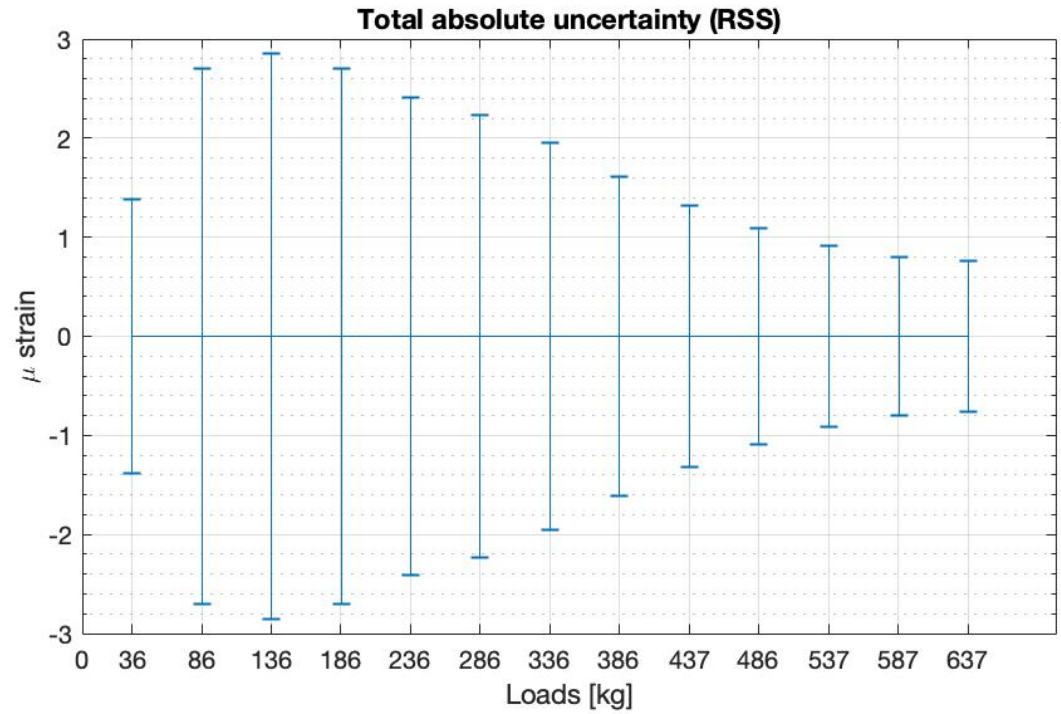

Figure 4.4: Case 1: The total absolute uncertainty in the output from the vertical-SGs applied axial load.

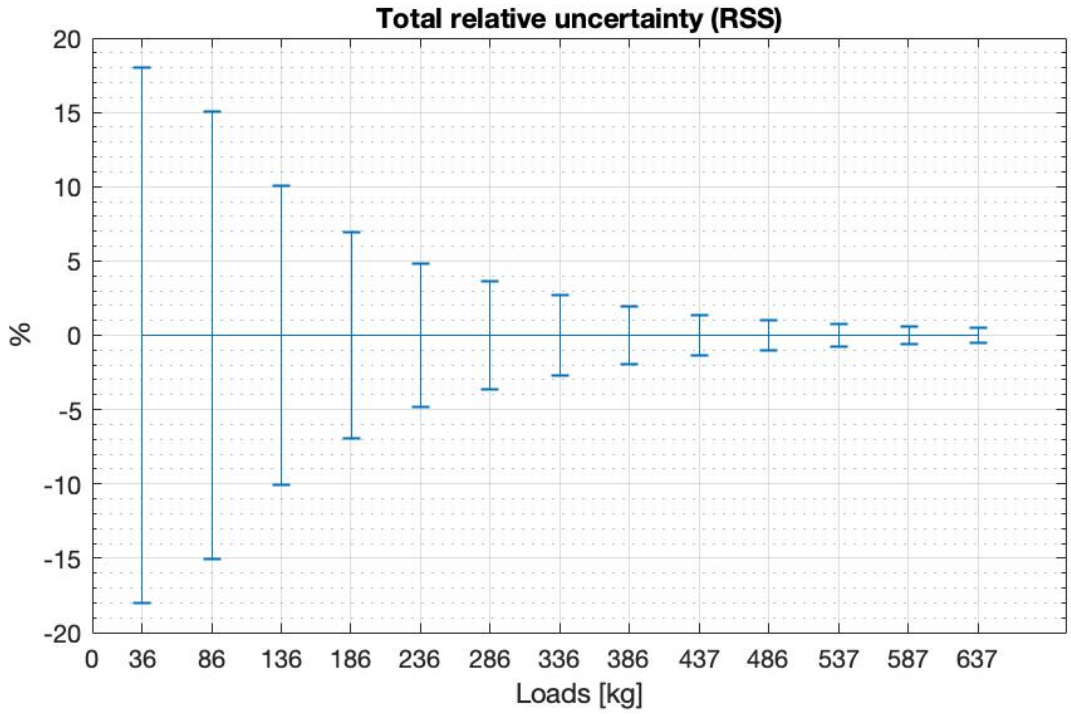

Figure 4.5: Case 1: The total relative uncertainty in the output from the vertical-SGs applied axial load.

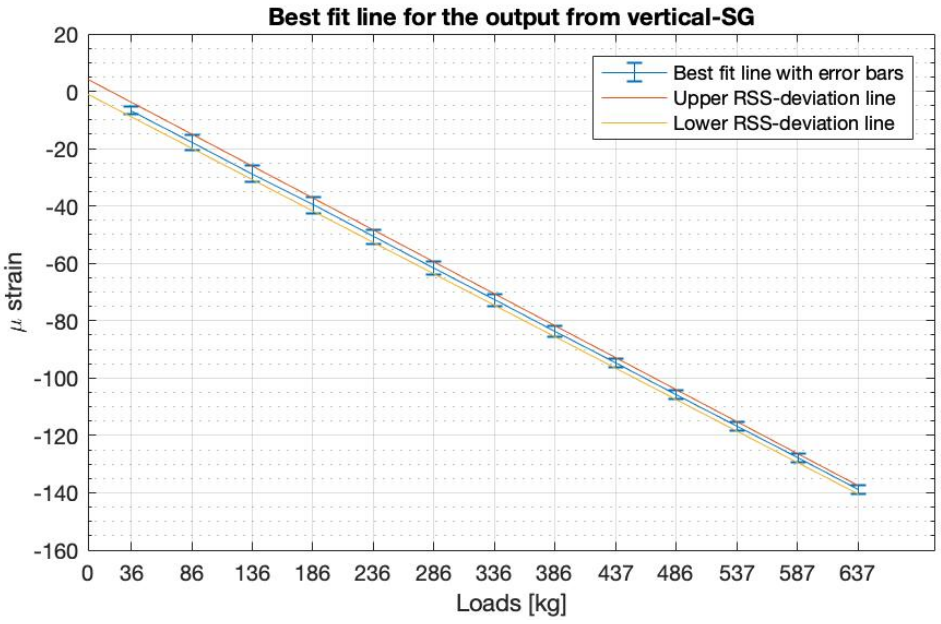

Figure 4.6: Case 1: Best fit line with upper and lower uncertainty band for vertical-SGs applied axial load.

Output From Diagonal-SGs

The diagonal-SGs was intended to measure torque, and was expected to have no output when applied axial load. As seen in Figure 4.7, that was not the case. Since the holes in the wall of the ATMD are diagonal, the forces applied must also work in the same diagonal direction along the holes, leaving the diagonal-SGs affected. Even so, the full-bridge arrangement should cause the strain gauges to temperature compensate. It seems to be working as the warmest measurement, the blue series in Figure 4.1, is giving strain output in between the red and green measurement series.

The uncertainties in the output from the diagonal-SGs are shown in Figure 4.8. By comparing these results to the corresponding figure for vertical-SGs, Figure 4.3, it can be seen that repeatability is still the biggest contributor and that zero deviation has increased. Within each measurement series, the repeatability is quite good, but the strain gauges may be affected by some drifting resulting in low repeatability between the series. Figure 4.9 and 4.10 show the total absolute and relative uncertainty for the strain measured by diagonal-SGs with axial load applied. Since the total amount of strain measured by the diagonal-SGs is about one-third of the strains measured by the vertical-SGs, the relative uncertainties are much higher for the diagonal-SGs as the absolute uncertainties are about the same. Figure 4.11 shows the best fit line together with an upper and lower uncertainty band. These uncertainties being relatively higher than for the vertical-SGs is the reason for the choice of investigating other arrangements that could serve as a second source of strain data.

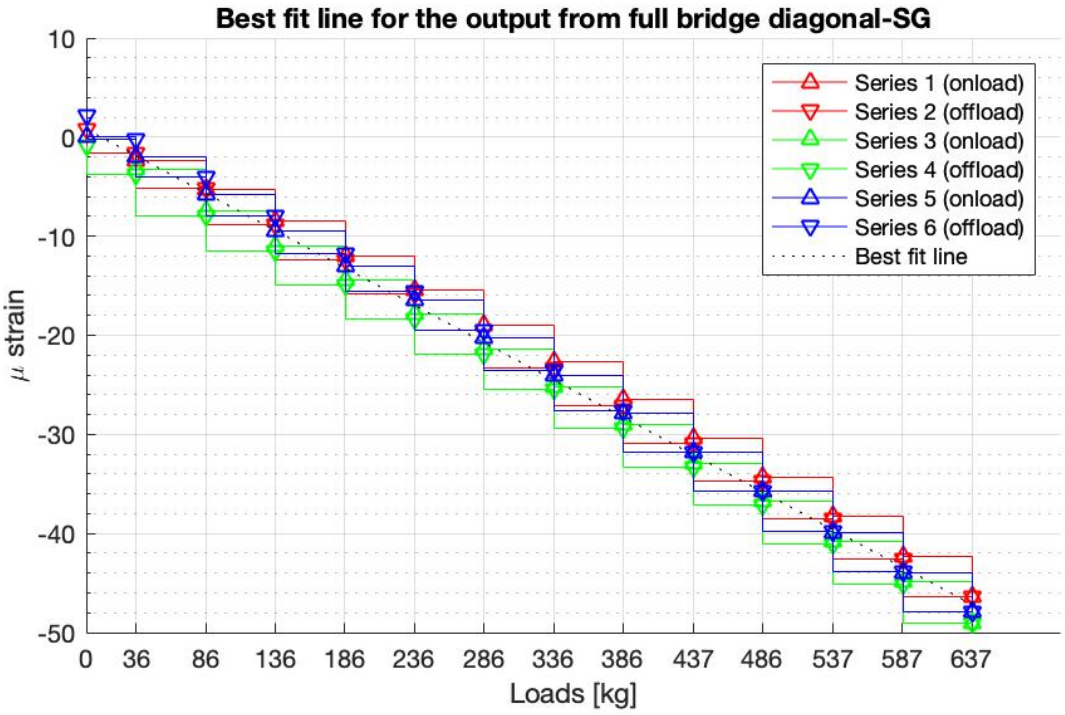

Figure 4.7: Case 1: The measured strain from the full-bridge diagonal-SGs and linear best fit line during axial load applied.

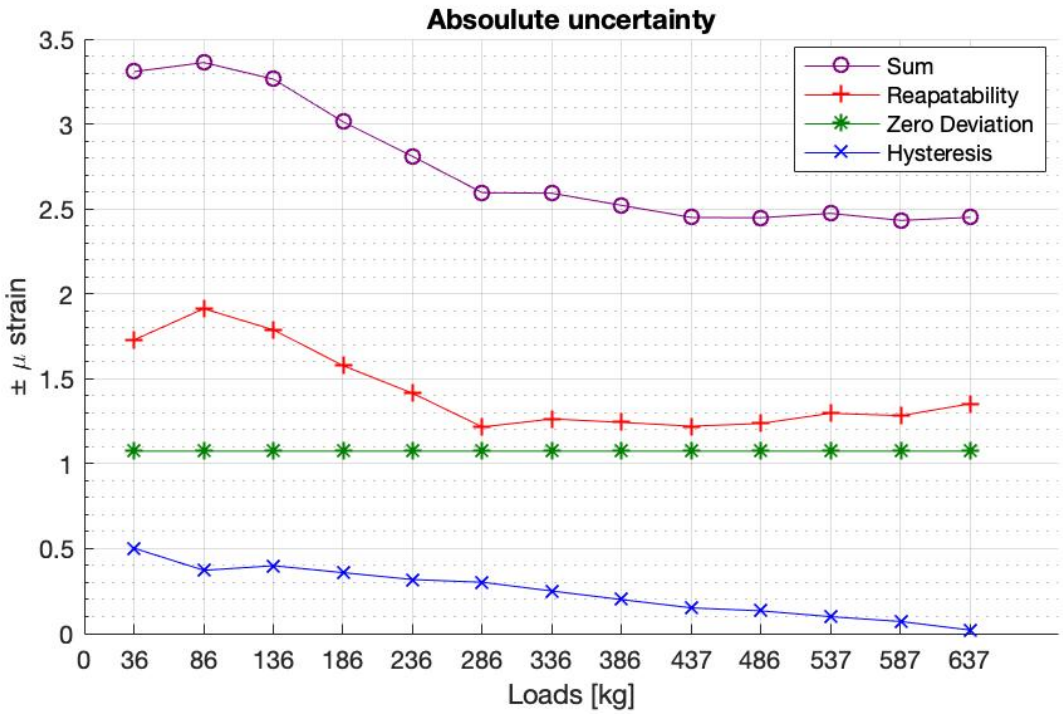

Figure 4.8: Case 1: Uncertainties in the output from the diagonal-SGs applied axial load.

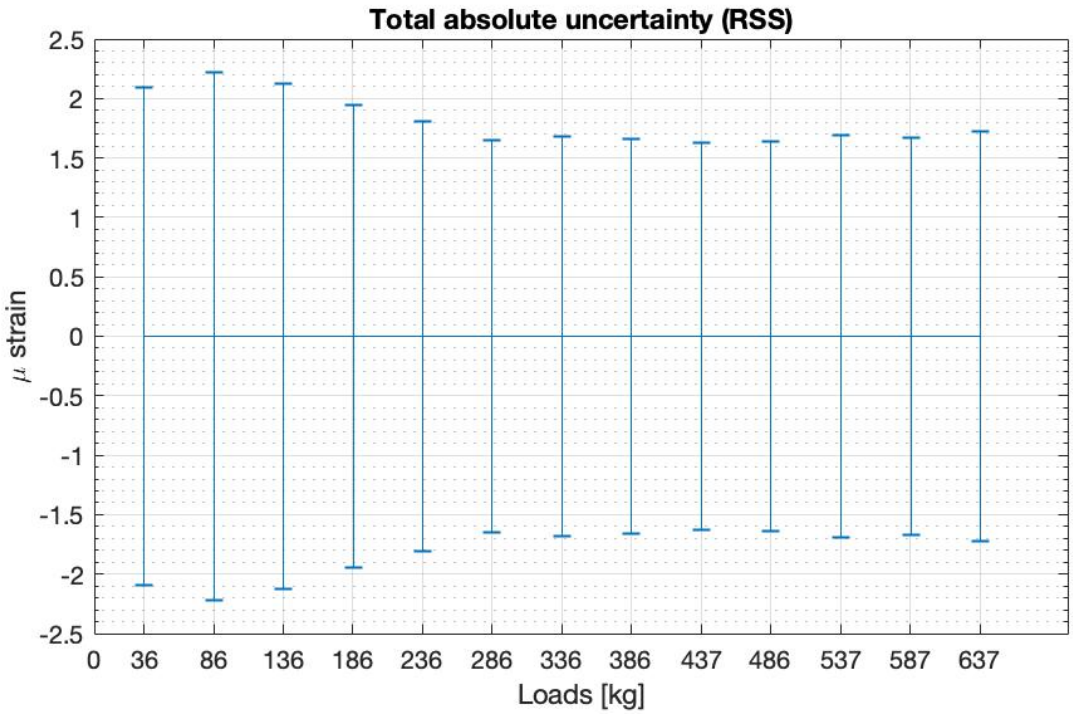

Figure 4.9: Case 1: The total absolute uncertainty in the output from the diagonal-SGs applied axial load.

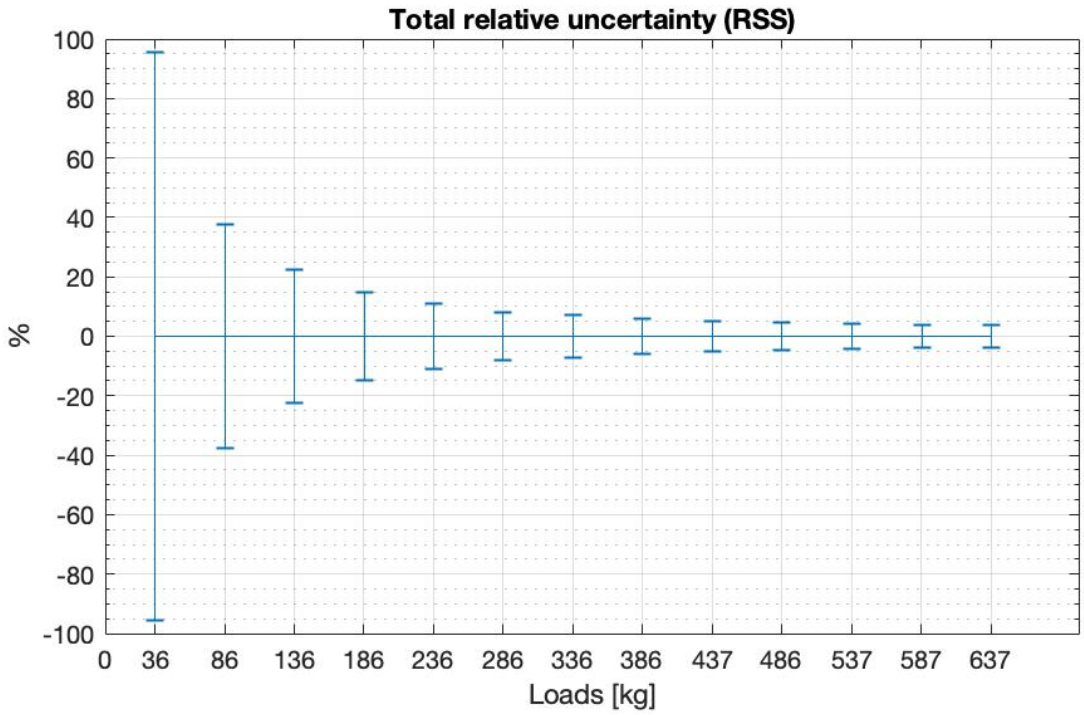

Figure 4.10: Case 1: The total relative uncertainty in the output from the diagonal-SGs applied axial load.

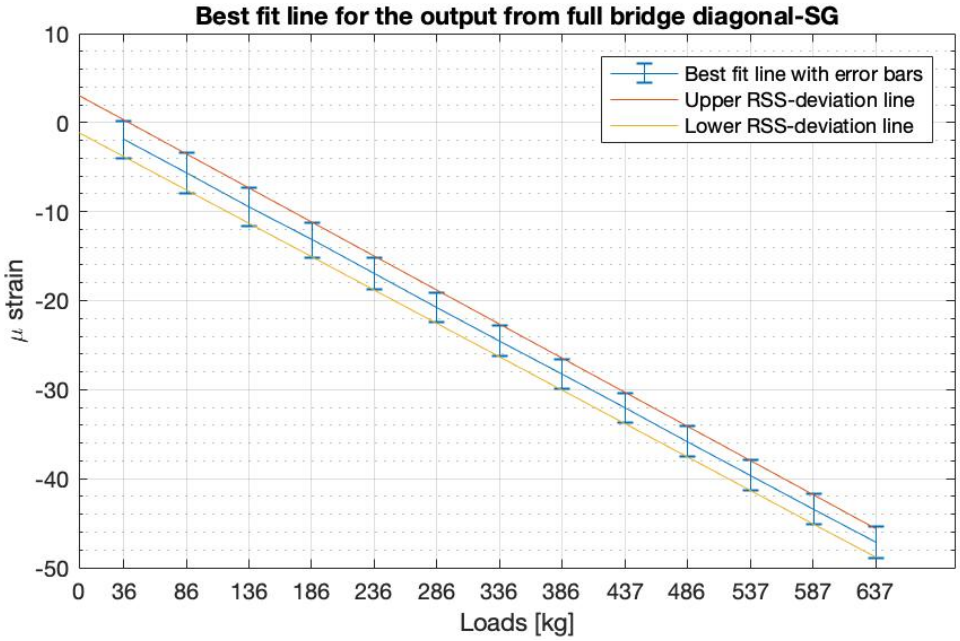

Figure 4.11: Case 1: Best fit line with upper and lower uncertainty band for the diagonal-SGs applied axial load.

4.1.2 Torque Load Applied

Output from Vertical-SG

Figure 4.12 shows the temperature development during the strain recording of torque applied, and Figure 4.13 shows the strain output from the vertical-SG. The temperature difference between the coldest and warmest measurement of 0.3 °C seems to not affect the strain output as the measured strain for the steps of applied torque is roughly the same for all the series.

The vertical-SGs seems to have more accurate results for torque load applied than for axial load. In Figure 4.14, it can be seen that the repeatability is no longer the biggest contributor to the uncertainty. The total absolute and relative uncertainty calculated is shown in Figure 4.15 and 4.16 respectively. By disregarding the first step with applied torque, which is the hanging system of 0.96 Nm, it can be seen that the total uncertainty is between 1 % and 3 %, which is quite low compared to other measurements. Figure 4.17 shows the best fit line with the upper and lower uncertainty band for the output of the vertical-SGs when applied torque. It can be seen that the linear best fit line fits quite good with the measured points and have low uncertainty.

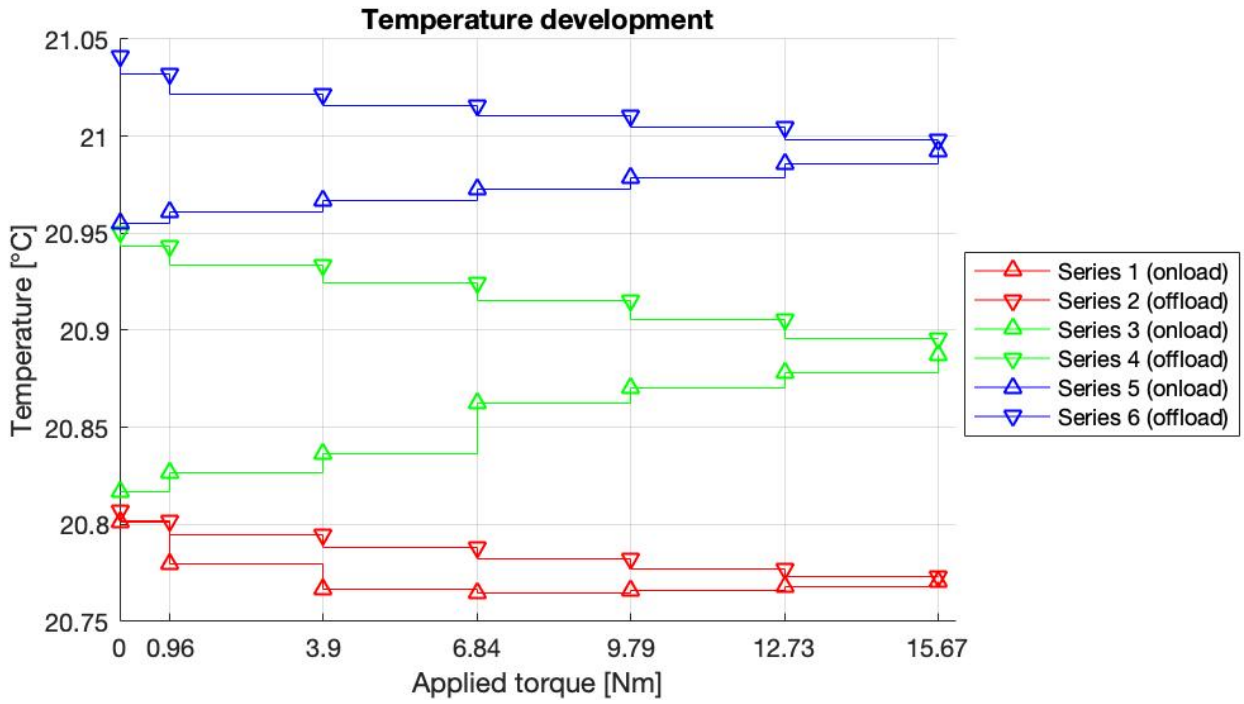

Figure 4.12: Case 1: Temperature development during torque applied.

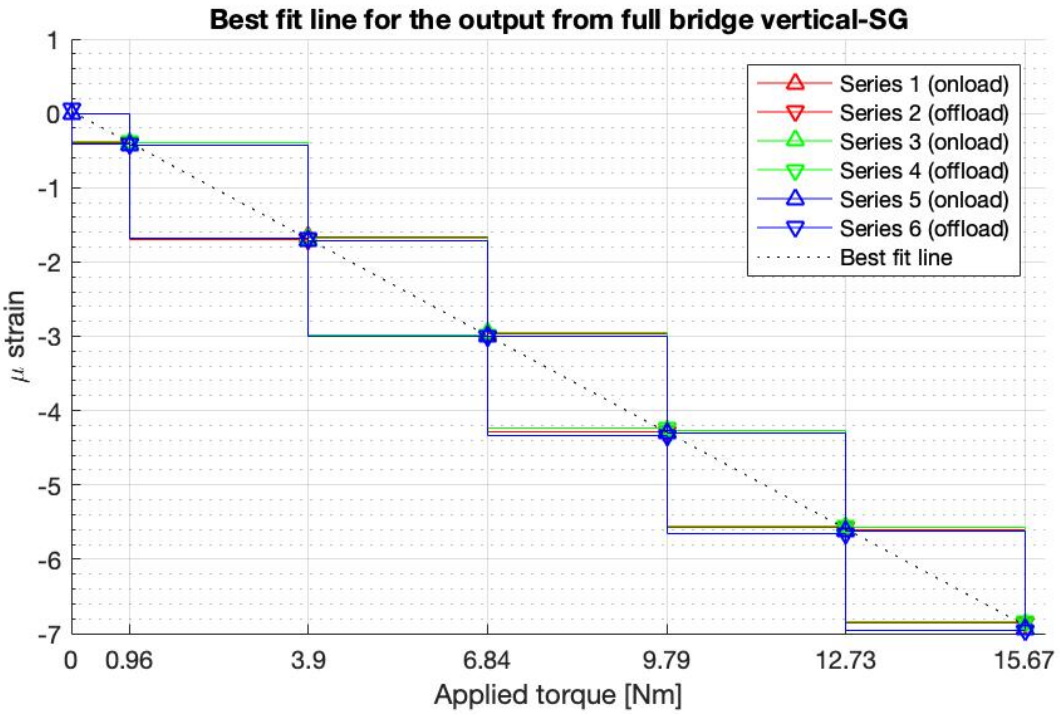

Figure 4.13: Case 1: Measured strain by vertical-SGs during torque load applied.

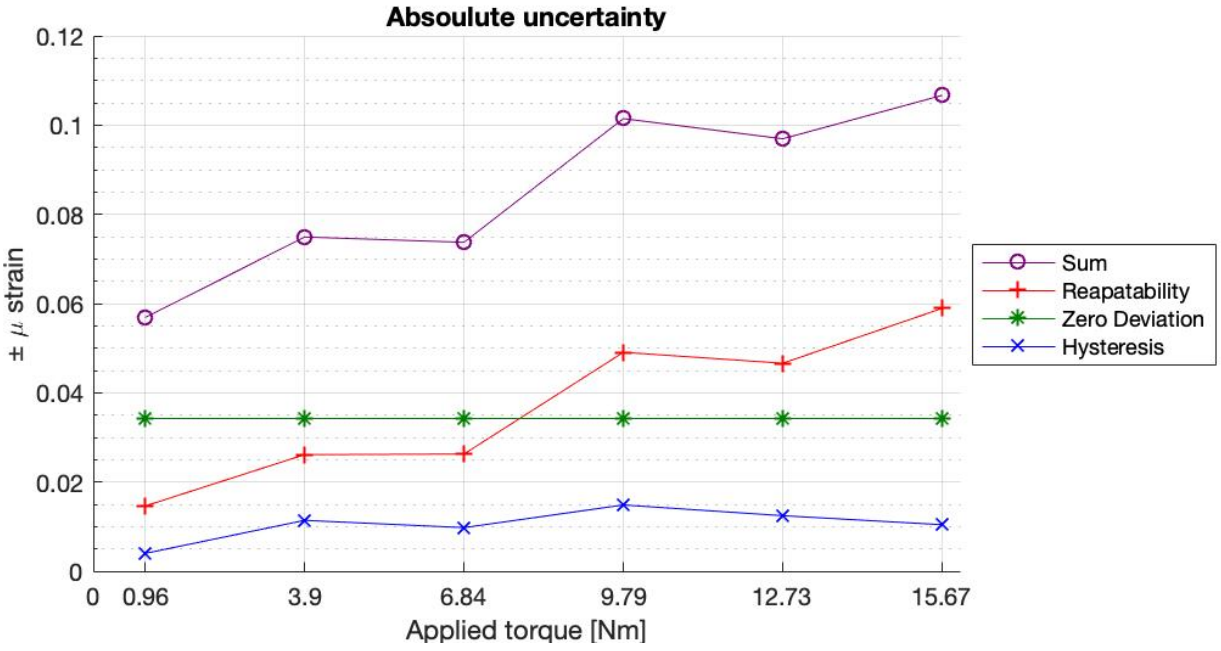

Figure 4.14: Case 1: Uncertainties in the output from the vertical-SGs applied torque load.

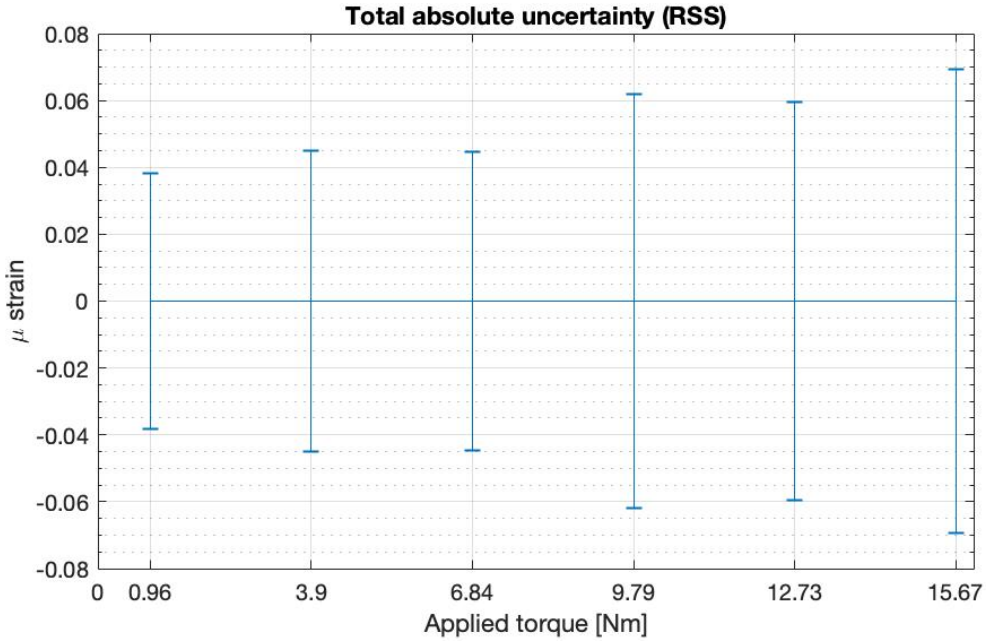

Figure 4.15: Case 1: The total absolute uncertainty in the output from the vertical-SGs applied torque load.

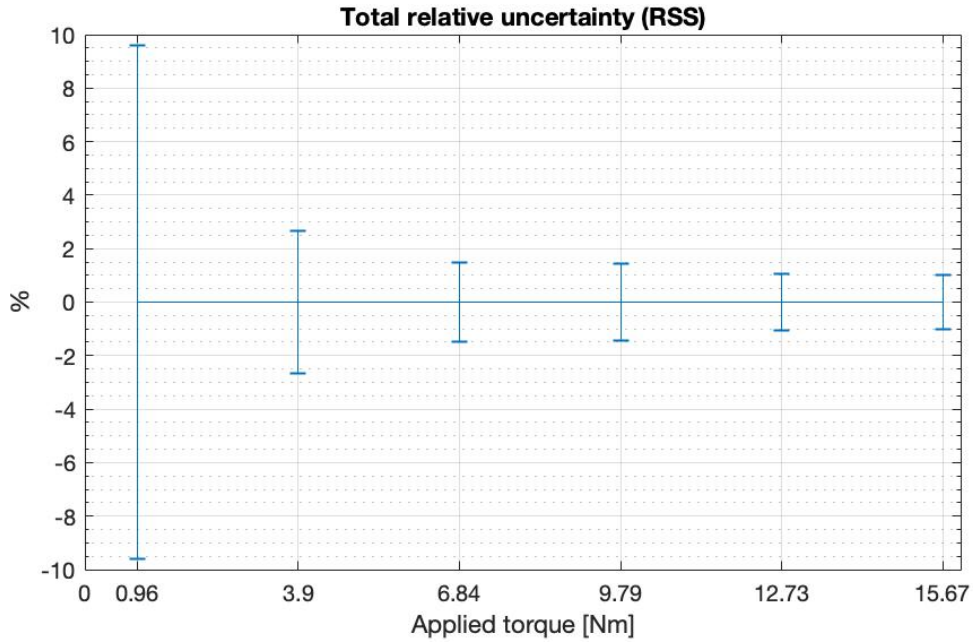

Figure 4.16: Case 1: The total relative uncertainty in the output from the vertical-SGs applied torque load.

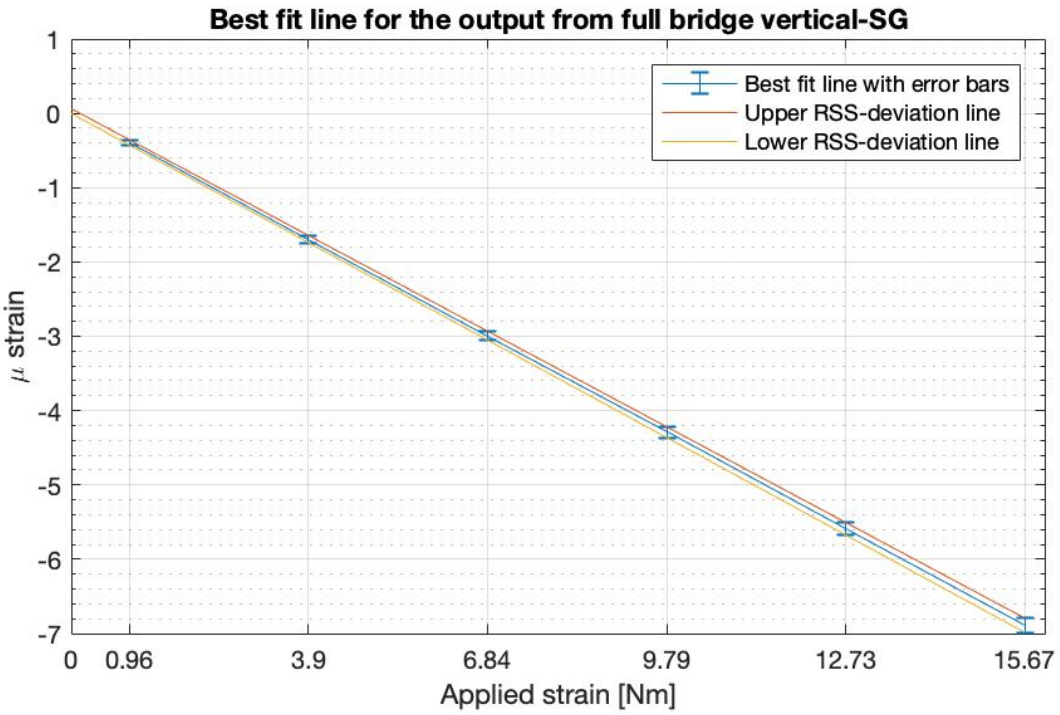

Figure 4.17: Case 1: Best fit line with upper and lower uncertainty band for vertical-SGs applied torque load.

Output from Diagonal-SG

The strain measured by the diagonal-SGs when applied torque is shown in Figure 4.18. The output range from 0.1 μstrain to -0.8 μstrain, which is a span of roughly 0.9 μstrain. Such small outputs are completely opposite of what to expect according to theory for a geometry without holes. This means that the strains act very differently in the ATMD with the diagonal slotted holes.

Even though the measurements looks messy in Figure 4.18, the calculated uncertainty is less than 0.1 μstrain for all measuring points, see Figure 4.19. As the measured values are very small, it is not suitable to regard the uncertainties as percentages. Figure 4.20 shows the linear best fit line with an upper and lower uncertainty band. The uncertainties for case 1 when applied torque is sufficiently low, but due to the uncertainties in the output of the diagonal-SGs when applied axial load, other test cases where investigated in the following.

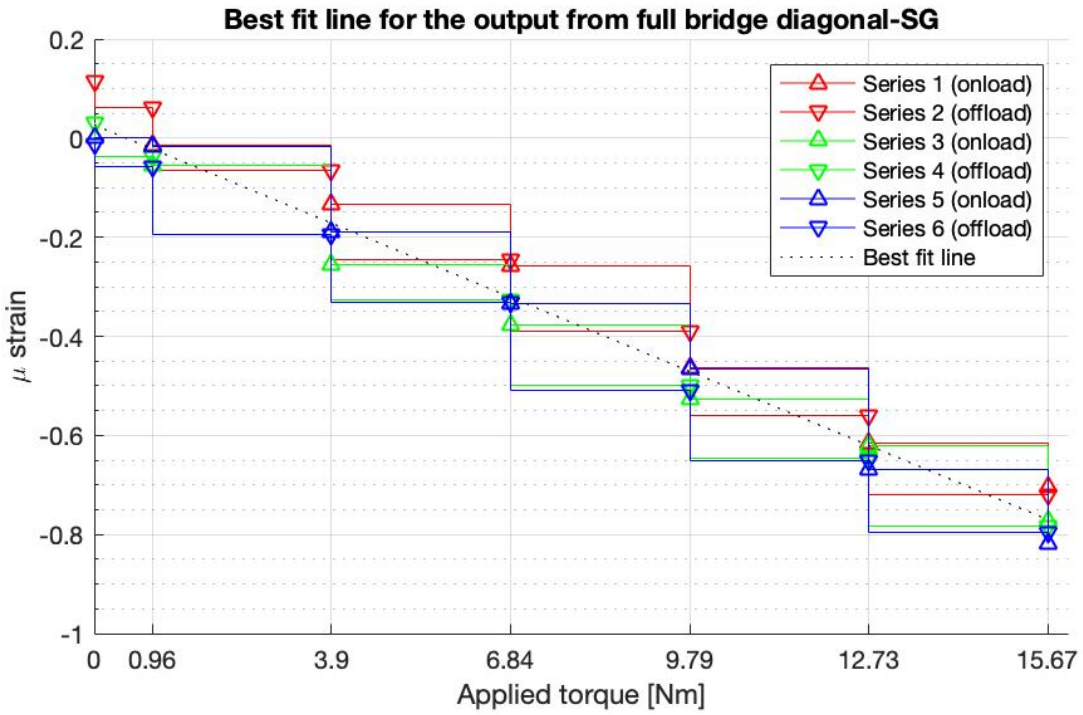

Figure 4.18: Case 1: The measured strain from the diagonal-SGs during torque load applied.

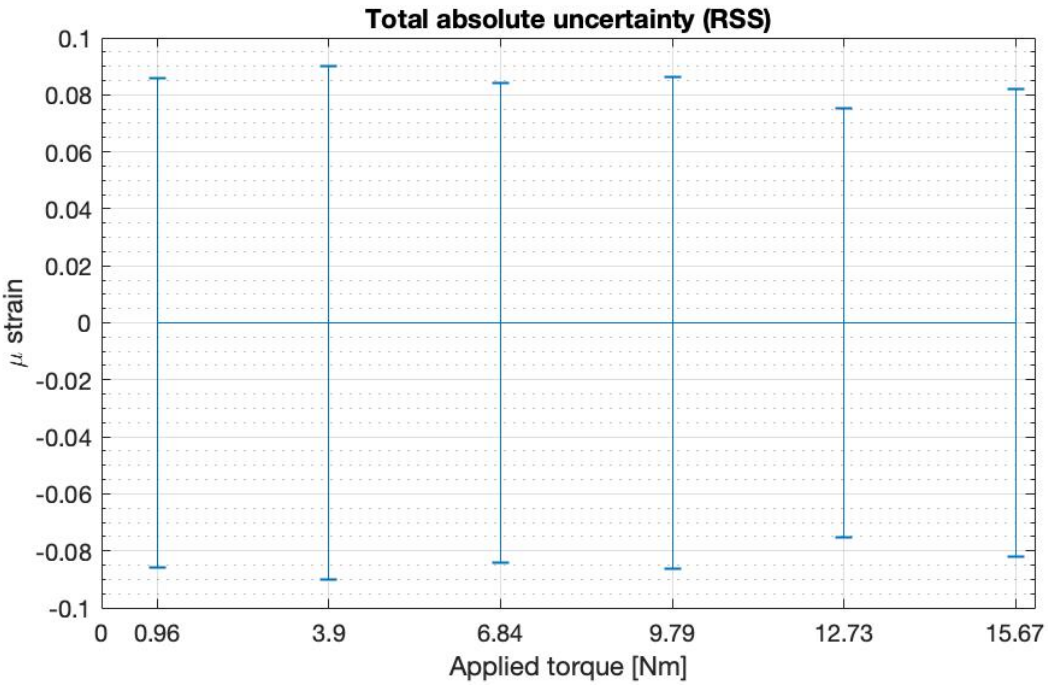

Figure 4.19: Case 1: The total absolute uncertainty in the output from the diagonal-SGs applied torque load.

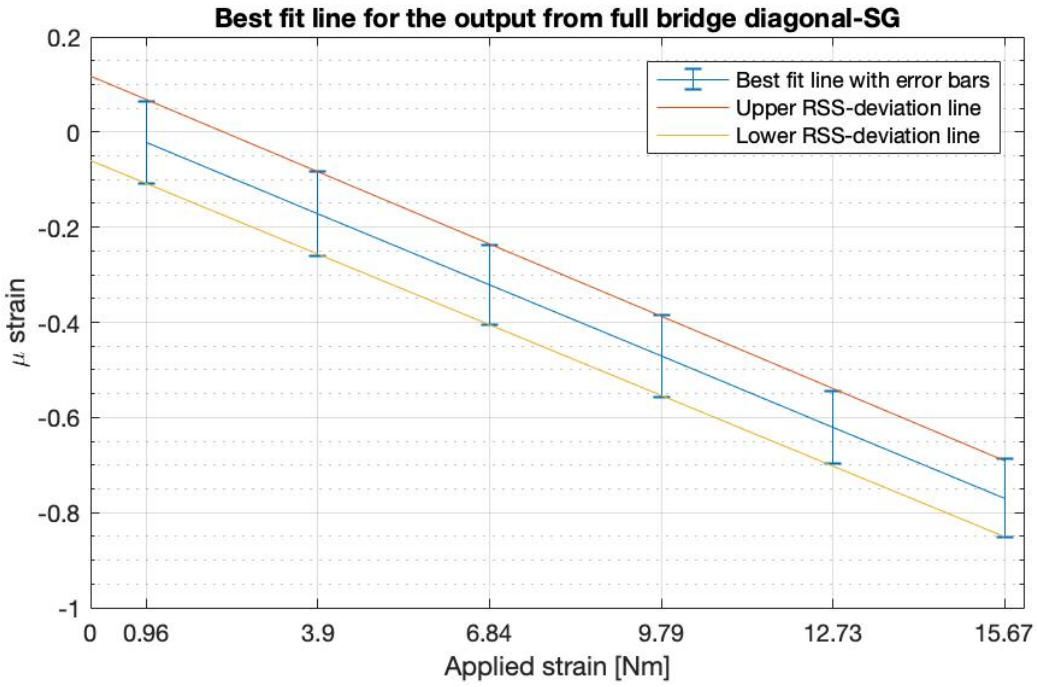

Figure 4.20: Case 1: Best fit line with upper and lower uncertainty band for the diagonal-SGs applied torque load.

4.2 Case 2: Vertical-SG in Full-bridge and Diagonal-SG in Half-bridge

As one strain gauge in one of the diagonal-SG-pairs was not placed in precisely 45°, it was suspected of causing uncertainties. This section is a compressed version of the investigation of whether a half-bridge configuration can replace the full-bridge diagonal-SGs from case 1, and serve as the second source of strain data. The complete investigation and more figures are included in Appendix B. The full-bridge vertical-SGs is kept as the first source.

4.2.1 Axial Load Applied

Output from Half-Bridge Diagonal-SGs

The recorded strain with a linear best fit line is shown in Figure 4.21. Even though the strains in case 1 and 2 have opposite sign, they are both applied the same compressing force, and the absolute value of the strains are comparable. This change to positive strain values is not intentional and can be disregarded as it is simply due to the wires being connected opposite. It can be seen that the blue series is drifting away from the other measurement series. This causes a big total uncertainty of above 4 μstrain, see Figure 4.22, which is twice as much as the total absolute uncertainty in the full-bridge diagonal-SGs in case 1. It can be concluded that to arrange the diagonal-SGs in a half-bridge is a worse alternative for axial load applied.

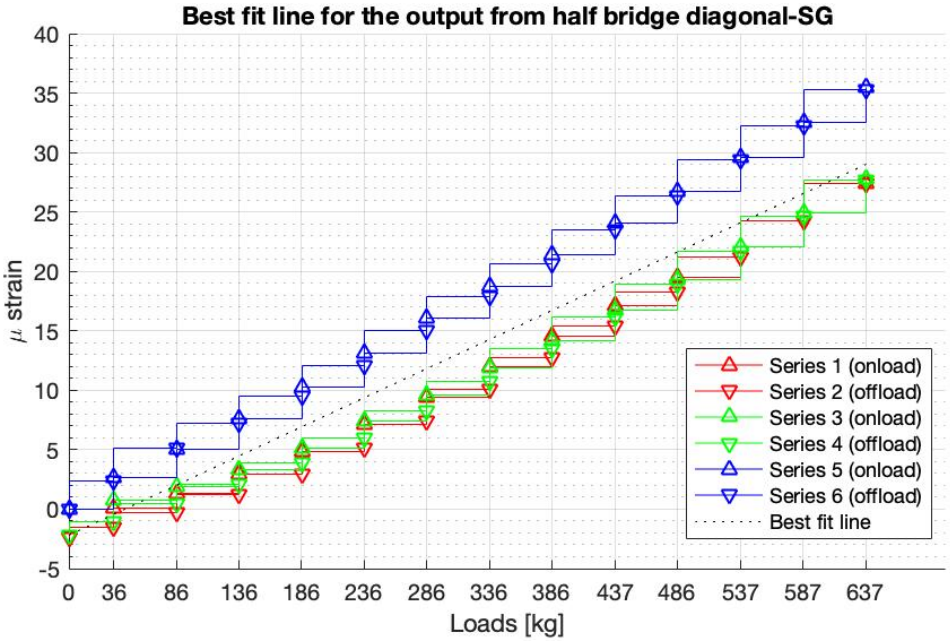

Figure 4.21: Case 2: The measured strain from the half-bridge diagonal-SGs during axial load applied.

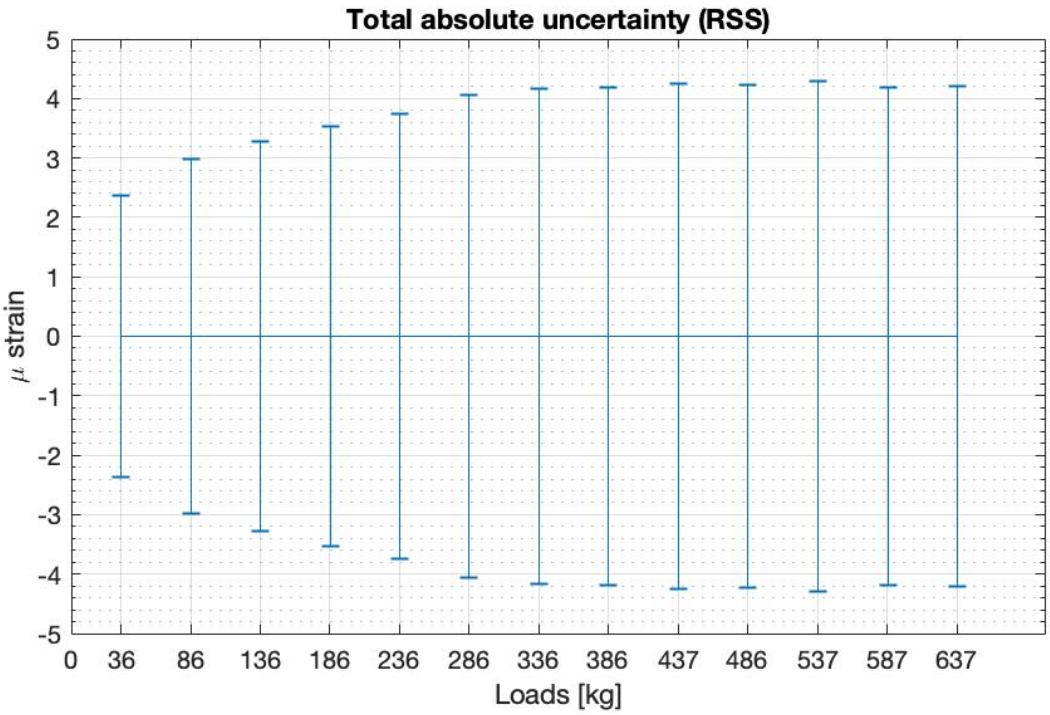

Figure 4.22: Case 2: The total absolute uncertainty in the output from the half-bridge diagonal-SGs applied axial load.

4.2.2 Torque Load Applied

Output from Half-Bridge Diagonal-SGs

For torque load applied to test case 2, the measured strain is presented in Figure 4.23. The strain range from -0.8 μstrain to 1.2 μstrain, with relatively large deviations in the strain output. This is mostly due to the green series, and partly the blue, dropping in strain value as the first torque load is applied. In Figure 4.24 it can be seen that the calculated uncertainty is around 0.6 μstrain. This is, in absolute terms, quite low, but it is almost ten times as high as the uncertainty for the full-bridge diagonal-SGs applied torque, case 1, which is around 0.08 μstrain, see Figure 4.19. By that, it can be concluded that case 2 is a worse alternative for torque load as well as for axial load.

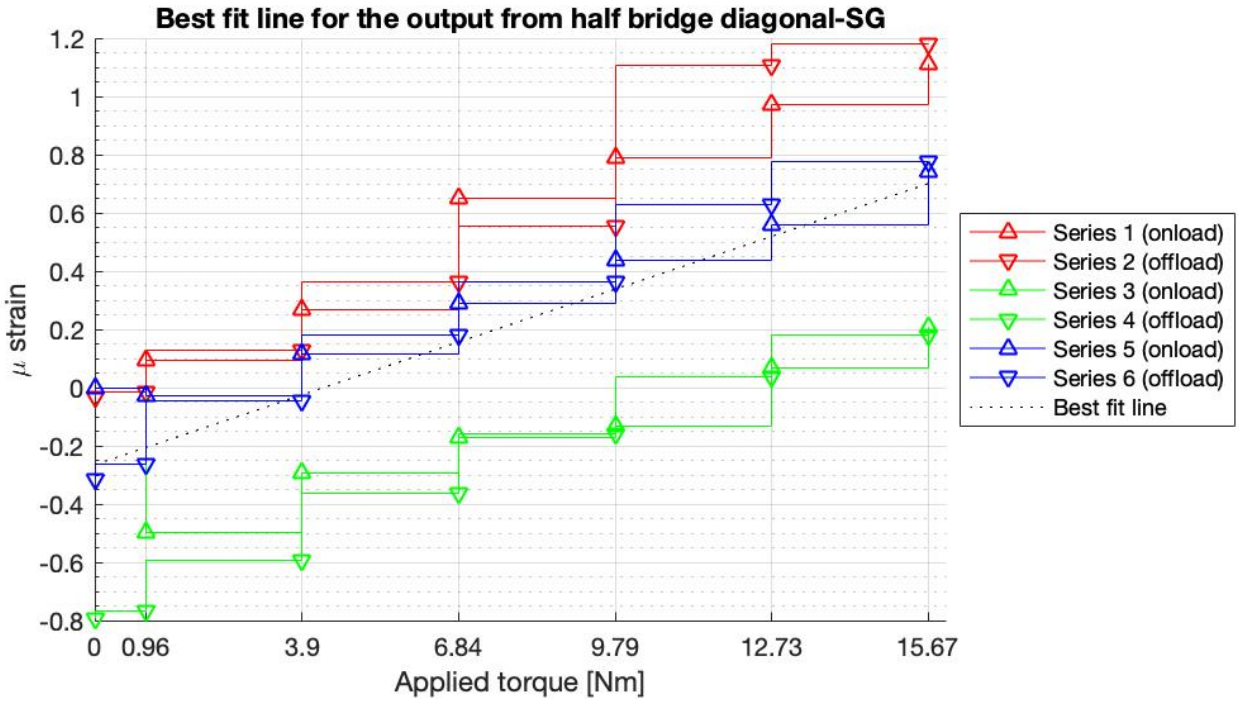

Figure 4.23: Case 2: The measured strain from the half-bridge diagonal-SGs during torque load applied.

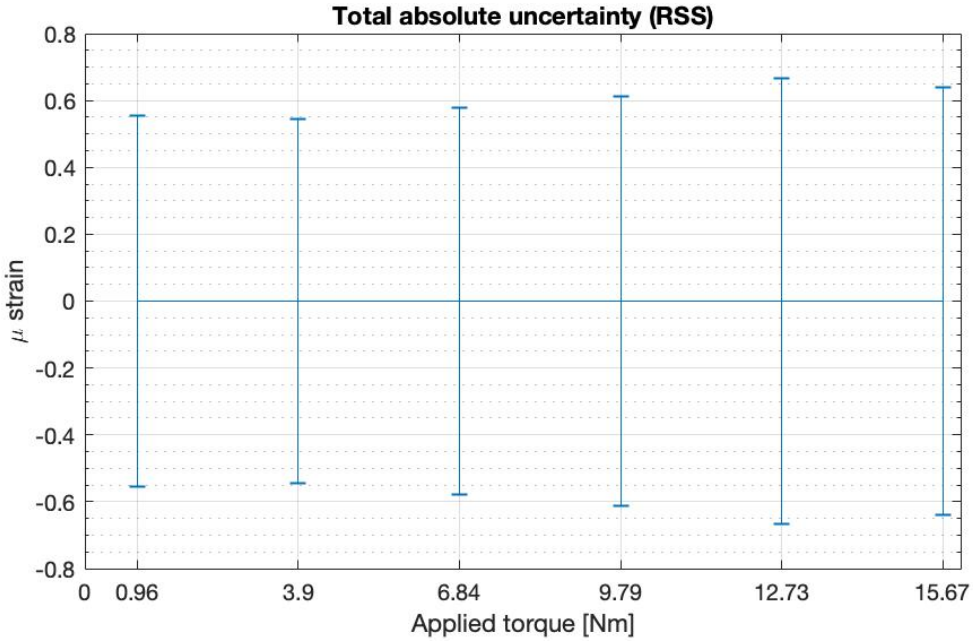

Figure 4.24: Case 2: The total absolute uncertainty in the output from the half-bridge diagonal-SGs applied torque load.

4.3 Case 3: Vertical-SG in Full-bridge and Single-SG in Quarter-bridge

The third test case was decided to contain a new strain gauge vertically placed in the upper part of the wall away from the holes and arranged in a quarter-bridge. It was thought that this strain gauge would get clean output from the axial load and minimal output from torque load. Additional plots may be found in appendix C.

4.3.1 Axial Load Applied

Output from Single-SGs

The temperature development during axial load applied is shown in Figure 4.25 and the strain measured is shown in Figure 4.26. As for case 2, due to the opposite cabling, the single-SG measure positive strain values, although the ATMD is applied compression forces. The different measurement series do not have an equal slope, even though they are applied the same load. This single strain gauge has no way of compensating for the temperature, and since the red series is both the most deviant and the warmest, the impact of the temperature must be investigated.

The strain gauges came along with a sheet of test data containing information about the strain gauges' behavior depending on temperature [24]. The tests were performed on SS400, a Japanese structural steel type similar to the German steel type ST44 [26], which is quite similar to the steel type ST52, used for the experimental version of the ATMD. The temperature influences the apparent strain with the relation

$$\epsilon_{app} = -2.33 \cdot 10^{1} + 1.57 \cdot T^{1} - 1.21 \cdot 10^{-2} \cdot T^{2} - 4.97 \cdot 10^{-4} \cdot T^{3} + 4.55 \cdot 10^{-6} \cdot T^{4} \quad (4.1)$$

and this curve is plotted in Figure 4.27. The blue measurement series has a temperature of around 21.4 °C for all measuring points, which gives a rise of 0.8 μstrain from the normalized 20 °C. The red measurement series, which is around 22.5 °C, has a rise of 1.4 μ strain. The deviation of 0.6 μstrain is removed in the offset nulling calibration procedure, described in section 3.3.1, that is ensuring all the measurements have the same starting position of close to zero strain for zero loads regardless of temperature. Since the temperature is not changing during on-loading and off-loading, this temperature-strain relation is not affecting the slope of the line.

There exists a small change in the gauge factor as a result of temperature change that could cause the slopes of the line to be different. For every 10th degree Celsius rise, the gauge factor rises by 0.1 % [24]. The gauge factor at the normalized 20 °C is 2.15 $\pm$1 %, and at 22.5 °C the gauge factor is 0.025% higher which is well within the uncertainty interval of the normalized gauge factor. This deviation in the gauge factor is too small to be the cause.

Even though no relation between the drift and the temperature was found, the article "How to battle drift in bonded foil strain gauge-based sensors" posted in Control Engineering argues that this kind of general drift is likely to be caused by temperature [27]. Further, it is argued that drifting is likely to occur even though the strain gauges and adhesive are matched with the surface material and the temperature range. Arranging the strain gauges in half-bridge or full-bridge in a temperature compensating arrangement is necessary. This statement is also supported by the data

found in this thesis as the full-bridge case 1 shows little indication of drifting, and the quarter-bridge of case 3 drifts a lot. Even though the series that is drifting in case 2 is neither especially warm or cold compared to the other series, the drifting might still be caused by temperature. Since the temperature probe is only measuring the surface temperature, and not the actual SG-temperature, drifting might occur as a result of the strain gauges self-heating [27].

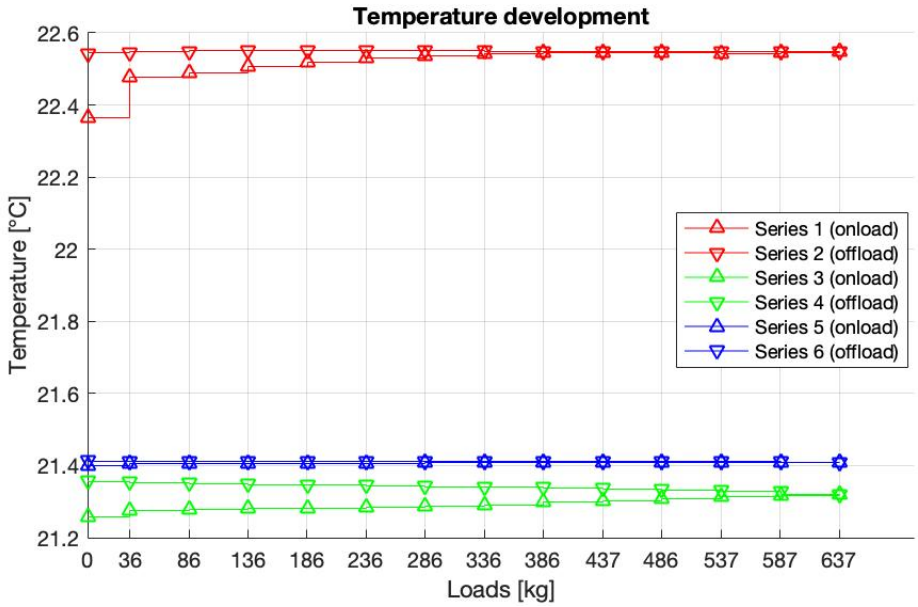

Figure 4.25: Case 3: Temperature development during axial load applied.

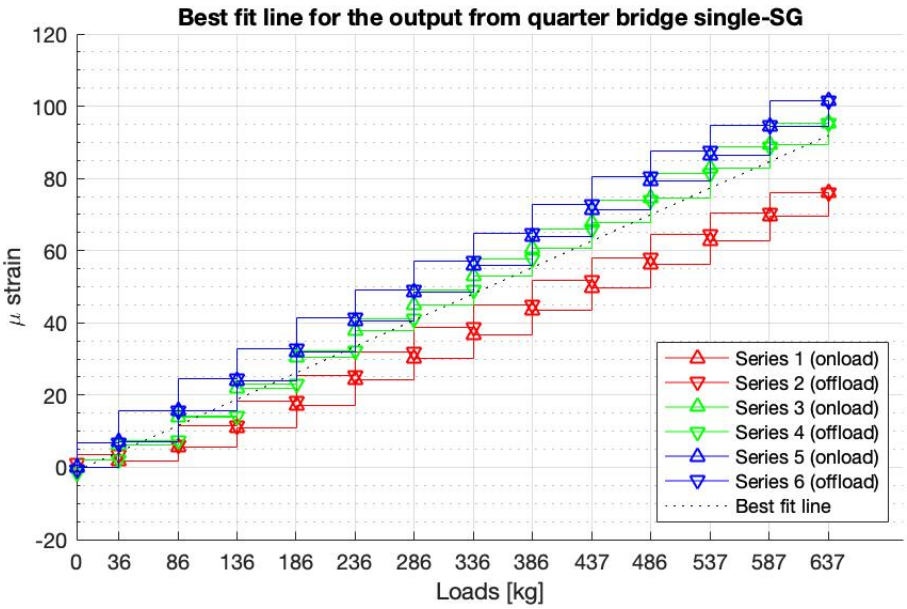

Figure 4.26: Case 3: The measured strain from the quarter-bridge single-SG applied axial load.

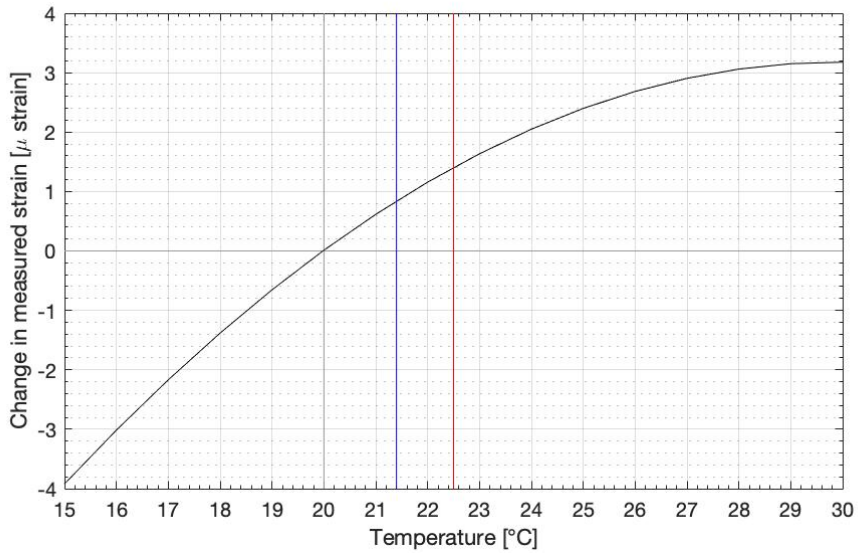

Figure 4.27: The change in measured strain due to change in temperature [24]. The blue and red line represent the approximate temperature in the blue and red measurement series respectively.

The total absolute uncertainty is given in Figure 4.28. It can be seen that the uncertainty is rising towards 13 μstrain, which is much higher than seen in any other of the test cases. As for case 2, the big uncertainties are mostly due to drifting series that cause low repeatability. The case with a single-SG arranged in a quarter-bridge is also concluded to be a worse alternative than case 1.

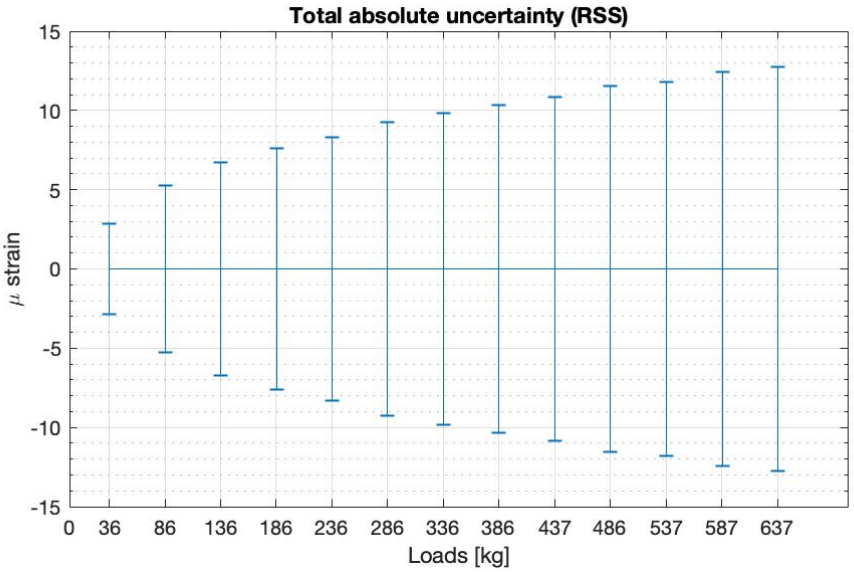

Figure 4.28: Case 3: The total absolute uncertainty in the output from the quarter-bridge single-SG applied axial load.

4.3.2 Torque Load Applied

Although case 3 is already concluded to be a worse alternative than case 1, the output for torque load is presented in the following for the sake of good order.

Output from Single-SGs

The temperature development during torque load applied to the single-SG is shown in Figure 4.29 and the strain measured is shown in Figure 4.30. These measurements show much less drifting than for axial load. A possible explanation is that the temperature is near-constant during the measurements and only varying by 0.04 °C, which means that the strain measured is not influenced by changing surface temperature. Another possible explanation is that the strain measured is very small. Since the strain measured when applied torque is around 3% of the strain measured when applied axial load, the drifting might have shown if the strains became larger. Figure 4.31 is showing the total absolute uncertainty. Even though the uncertainties calculated for the strain measurements for applied torque is much lower than for applied axial load, test case 3 is, in total, a worse alternative than case 1.

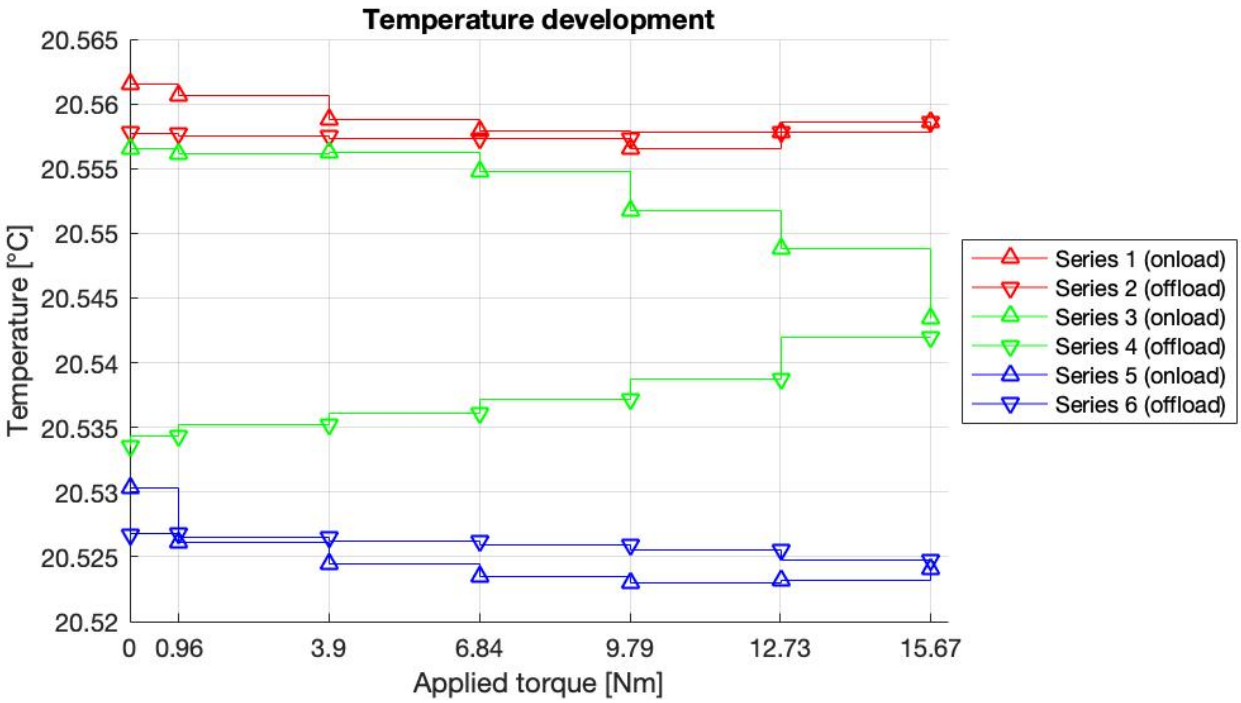

Figure 4.29: Case 3: Temperature development during torque load applied.

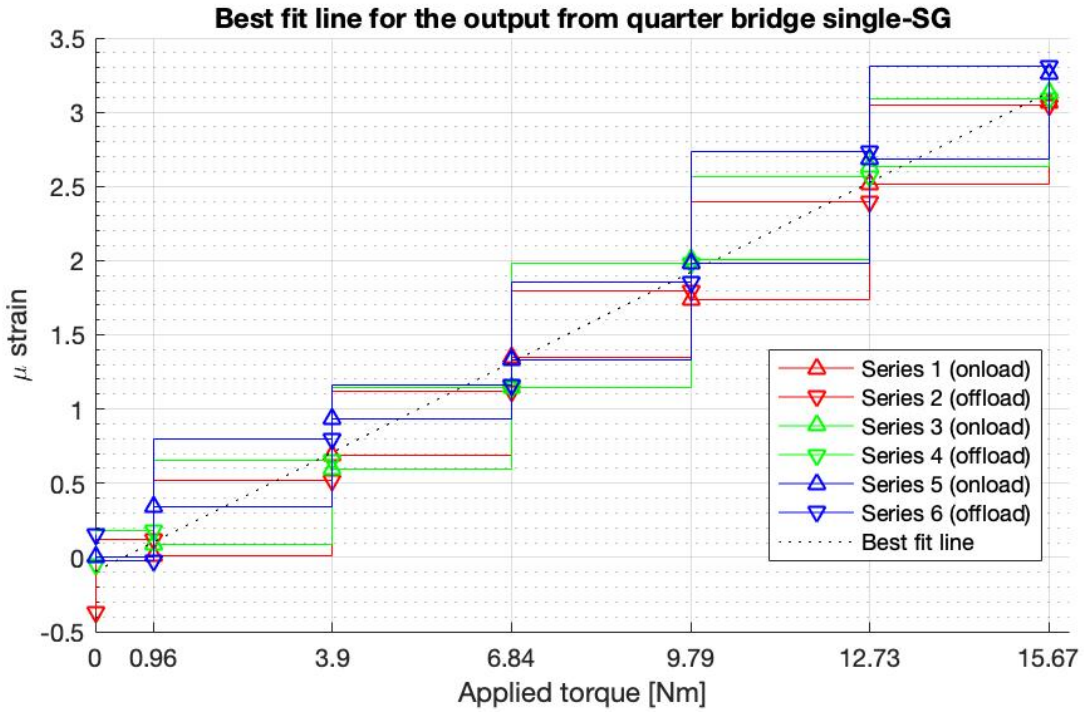

Figure 4.30: Case 3: The measured strain from the quarter-bridge single-SG during torque load applied.

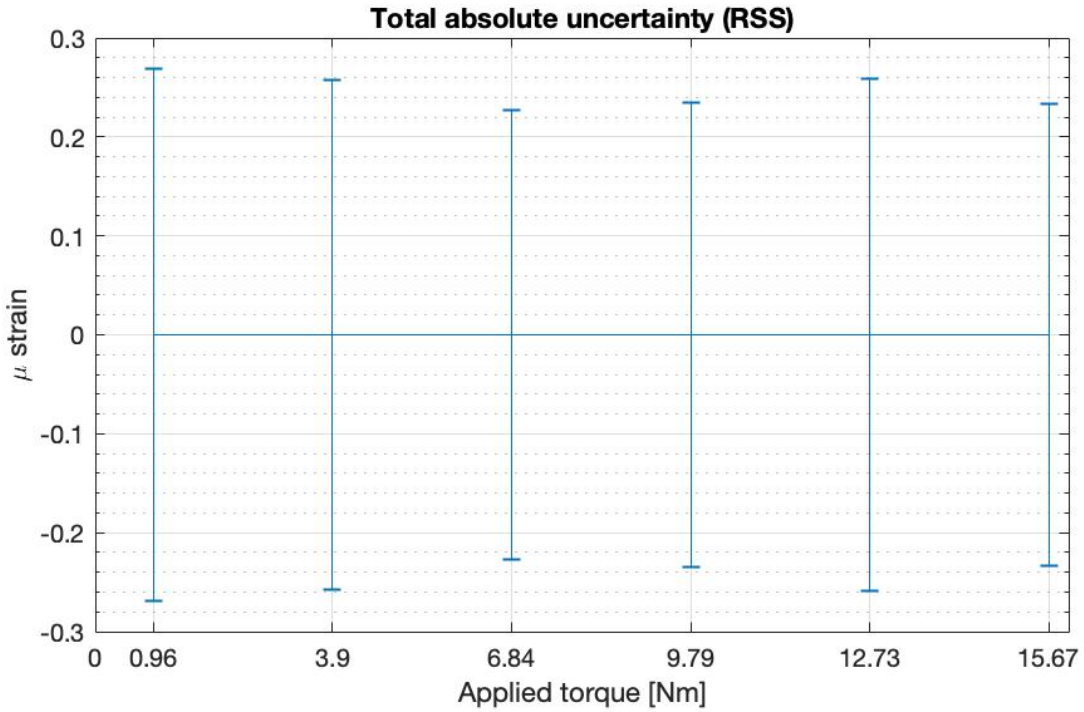

Figure 4.31: Case 3: The total absolute uncertainty in the output from the quarter-bridge single-SG applied torque load.

Chapter 5

Discussion

This chapter contains discussions based on the results from Chapter 4. In section 5.1, the direction of the strains is investigated through vector plots, and a better understanding of why the output was not as expected is obtained. In section 5.2 it is investigated whether it is possible to obtain calibration equations that depend on both strain gauge set. As the calculated uncertainties are too high, an improved design is presented in section 5.3, and this design is the final recommended version of the ATMD.

5.1 Direction of Strain

As the holes are diagonal with a 45° tilt, the forces working through the ATMD must also aggregate in that same direction. Figure 5.2 and 5.3 show numerically calculated vector plots of the strains working along the holes for 7000 N and 20 Nm applied respectively. Elongation and compression are occurring on either side of the holes, ensuring strain to work in multiple directions. The yellow and the green squares represent the approximate placement of the vertical-SGs and diagonal-SGs, respectively. In the figures, blue arrows represent compression, red arrows represent elongation, and the size of the arrowhead represents the size in absolute value.

For only axial forces applied, it can be seen in Figure 5.2 that the vertical compression is the dominant strain component as the blue arrowheads are larger than the red. The vertically placed strain gauges are getting quite clean output in the experiments because the strain gauges are only affected by the vertical compression components. The diagonally placed strain gauges, on the other hand, are inflicted by both the vertical compression and horizontal elongation, which causes the output to be a lower absolute value than the vertical-SGs. Since all four diagonal-SGs are placed in the same small place, the exact placement of the strain gauges might affect the output and causing a bigger uncertainty than in the results from the vertical-SG.

When the ATMD only is applied torque, see Figure 5.3, neither the blue vertical compression arrows nor the red horizontal elongation arrows are the clear dominant strain component. As the vertical-SGs mostly are affected by the vertical compression and mostly independent of the horizontal elongation, they have quite clean output also for solely torque applied. The diagonally placed strain gauges, in the other hand, are both compressed and elongated at the same time, see

Figure 5.1. If the compression and elongation are approximately the same sizes, this explains their near-zero output. As the vector plots confirm the experimental results, these kinds of plots are used in the development of an improved design in section 5.3.

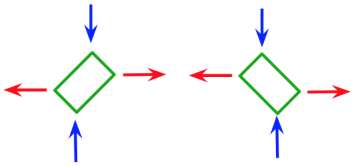

Figure 5.1: The strain acting on the diagonal-SGs when applied torque. Red arrows are elongation and blue arrows compression.

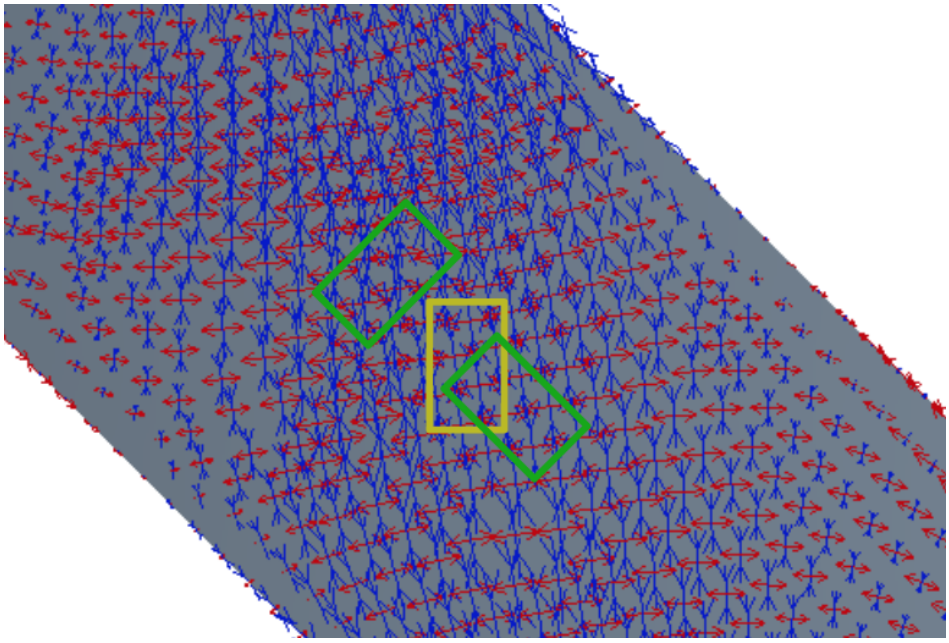

Figure 5.2: Vector plot of the strains in the ATMD when applied axial compression (7000 N). Red arrows are elongation and blue arrows compression.

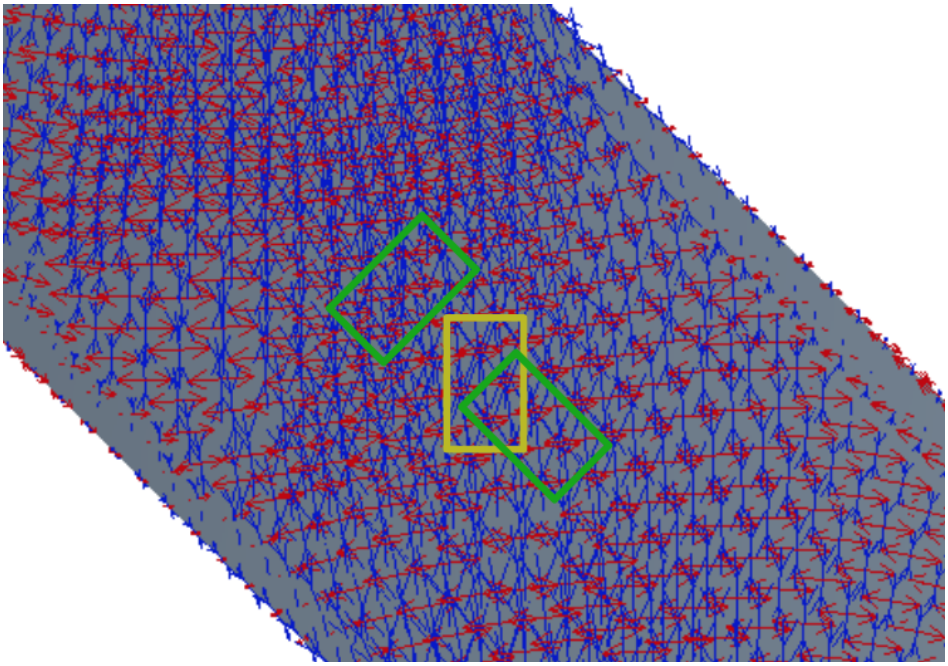

Figure 5.3: Vector Plot of the strains in the ATMD when applied torque (20 Nm). Red arrows are elongation and blue arrows compression.

5.2 Choosing Case 1 to Complete the Measurement System

The goal of the data collection and analysis in the previous chapter is to obtain two final calibration equations. The two unknowns, applied axial load *F* and friction torque *T*, will be functions of the two measurable variables, strain output from vertical-SGs and diagonal-SGs. The easiest way would have been to have two sets of strain gauges that only had output for one type of load each. The vertical-SGs was meant only to measure axial load and would, for a geometry with no holes in the wall, have no output for torque load or temperature change [19], meaning *F=f(vertical-SG)*. The diagonal-SGs would, for a geometry with no holes in the wall, only have output for torque load and cancel out any strain caused by axial load and temperature change [19], meaning *T=f(diagonal-SG)*.

As seen in the previous section, the diagonal slotted holes caused both vertical-SGs and diagonal-SGs to have output for both axial and torque load, which means *F=f(vertical-SG, diagonal-SG)* and *T=f(vertical-SG, diagonal-SG)*. In other words, the final calibration equations will describe two planes as they are linearly dependent on two variables. With this method, the uncertainty in the data for both the strain gauge sets when applied both axial and torque load must be accounted for, which leaves cases 2 and 3 not usable due to their big uncertainties.

In Figure 5.4, the strain measured by vertical-SGs and diagonal-SGs are shown when applied axial load only. Case 2 and 3 were tested because the uncertainties for diagonal-SGs when applied axial load were relatively higher than preferred, but it can be seen that in absolute terms and compared to the uncertainties in the vertical-SGs, the uncertainties are not that big.

In the following equations, axial force is given in *kg* added load and torque is given in *Nm*. The lines are expressed on the form $y = A \cdot x + B$ where the subscript *v* and *d* means vertical-SGs and diagonal-SGs respectively, and *a* and *t* means axial and torque load applied respectively. Figure 5.4 show strain output for solely axial load applied so the lines can be express as a function of applied force *F* as the lines lay in the zero-torque-load-plane. The best fit line for the vertical-SGs, the blue line, is given by

$$\epsilon_{vertSG,AxLoad(T=0)} = A_{v,a} \cdot F + B_{v,a} \qquad [-] \tag{5.1}$$

and the best fit line for diagonal-SGs, the green line, is given by

$$\epsilon_{diagSG,AxLoad(T=0)} = A_{d,a} \cdot F + B_{d,a} \qquad [-] \tag{5.2}$$

In Figure 5.5, there is not applied any axial force, and the lines can be express only as a function of applied torque *T* as the lines lay in the zero-axial-load-plane. The best fit line for the vertical-SGs, the blue line, is given by

$$\epsilon_{vertSG,ToLoad(F=0)} = A_{v,t} \cdot T + B_{v,t} \qquad [-] \tag{5.3}$$

and the best fit line for diagonal-SGs, the green line, is given by

$$\epsilon_{diagSG,ToLoad(F=0)} = A_{d,t} \cdot T + B_{d,t} \qquad [-] \tag{5.4}$$

where the numerical values of *A* and *B* is given in Table 5.1.

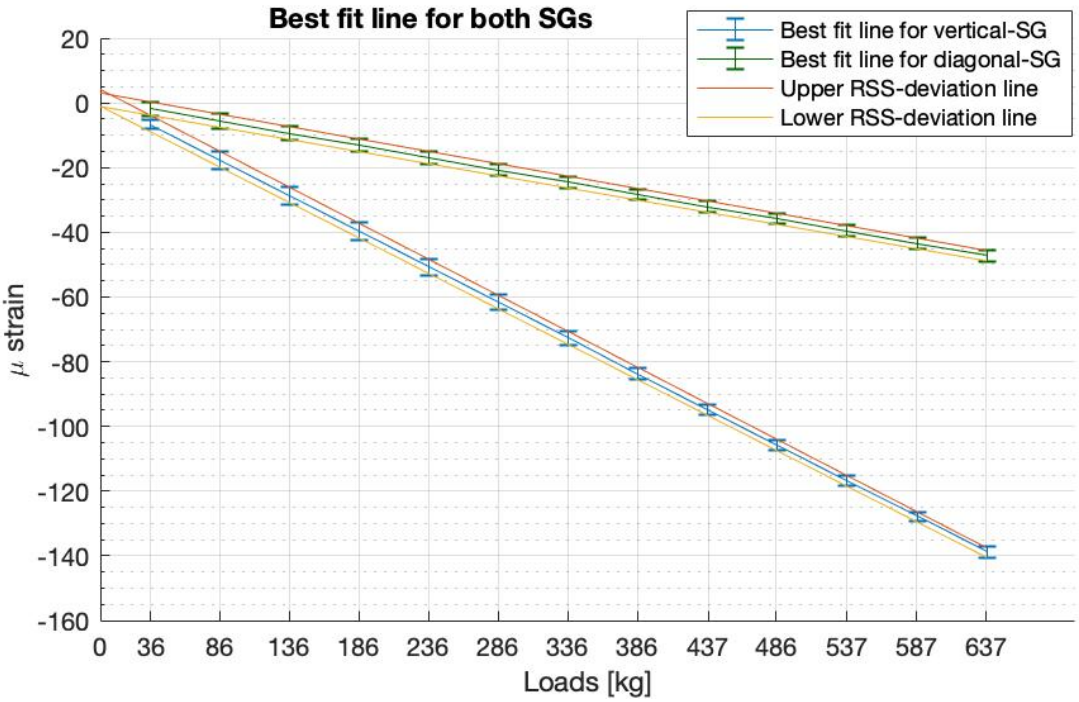

Figure 5.4: Output from vertical-SGs and diagonal-SGs applied axial load.

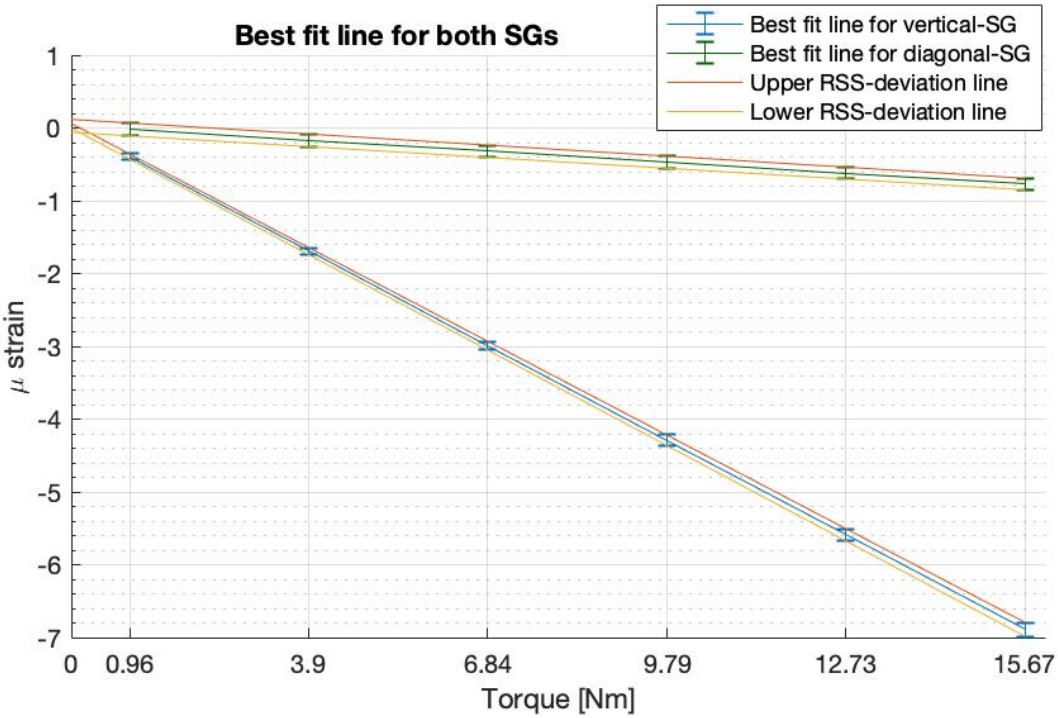

Figure 5.5: Output from vertical-SGs and diagonal-SGs applied torque load.

Coefficent	Numerical value
$A_{v,a}$	- 0.2197
$A_{d,a}$	- 0.0753
$A_{v,t}$	- 0.4415
$A_{d,t}$	- 0.0508

Coefficent	Numerical value
$B_{v,a}$	1.1621
$B_{d,a}$	0.8072
$B_{v,t}$	0.0300
$B_{d,t}$	0.0265

Table 5.1: The numerical values of the best fit lines in Figure 5.4 and Figure 5.5.

To be able to calculate the unknown axial forces and friction torque, these lines and equations must be combined. The strain measured by each strain gauge set is independent of the other, and as the zero-torque-load-plane and the zero-axial-load-plane are perpendicular, the strain measured in each plane is independent of the other. If the two lines describing the output of the vertical-SGs, equation 5.1 and 5.3, and the two lines describing the output of the diagonal-SGs, equation 5.2 and 5.4, had been exactly zero for zero load, then to combine the pair of lines to two planes would be done by simply adding them together [28]. As the lines to combine do not intersect, there is no mathematically way to combine them into a plane. This however, is possible to bypass. The plane's point of intersection with the strain axis is chosen to be the mean value of the two lines intersection points with the strain axis. This adjustment places the resulting plane between the lines in the zero-torque-load-plane and zero-axial-load-plane while their slope is kept. Then, by introducing a deviation that covers the actual intersection of the two lines, the approximation is taken into account.

The resulting planes are given in Figure 5.6. The blue plane is the output from the vertical-SGs when applied both axial and torque load, and is given by

$$\epsilon_{vertSG} = A_{v,a} \cdot F + A_{v,t} \cdot T + (B_{v,a} + B_{v,t})/2 \quad \pm (B_{v,a} - B_{v,t})/2 \qquad [-] \tag{5.5}$$

The green plane is the output from the diagonal-SGs when applied both axial and torque load, and is given by

$$\epsilon_{diagSG} = A_{d,a} \cdot F + A_{d,t} \cdot T + (B_{d,a} + B_{d,t})/2 \quad \pm (B_{d,a} - B_{d,t})/2 \qquad [-] \tag{5.6}$$

In both equations, when only applied axial force (T=0) the strain output is slightly underestimated compared to the actual value, and when only applied torque (F=0) the strain output is slightly overestimated compared to the actual value. This is because the lines in the zero-torque-plane crosses the strain axis at a point of higher value than the lines in the zero-axial-force-plane.

The preceding equations may be compared to Figure 5.4 and 5.5 in order to verify them. For maximum axial load applied of 637 kg and no torque applied, the equations should give output similar to the maximum absolute values shown in Figure 5.4. Equation 5.5, describing the blue line, gives -139 $\pm$ 0.5661 μstrain, and equation 5.6, describing the green line, gives -48 $\pm$ 0.3904 μstrain. The calculated values match well, and the deviation is relatively small. For the maximum torque of 15.67 Nm and no axial load applied, the equations should give values similar to the maximum absolute values shown in Figure 5.5. Equation 5.5, describing the blue line, gives -6.32 $\pm$ 0.5661 μstrain, and equation 5.4, describing the green line, gives -0.38 $\pm$ 0.3904 μstrain. The calculated values do match the values given in the figures when including the relatively high deviations. The relative deviation becomes high for torque load because the preceding equations

and the corresponding deviations are results of the strain measured when applied both solely axial load and solely torque load. Note that the output for axial load is about 20 and 60 times as high as for torque load for vertical-SGs and diagonal-SGs, respectively.

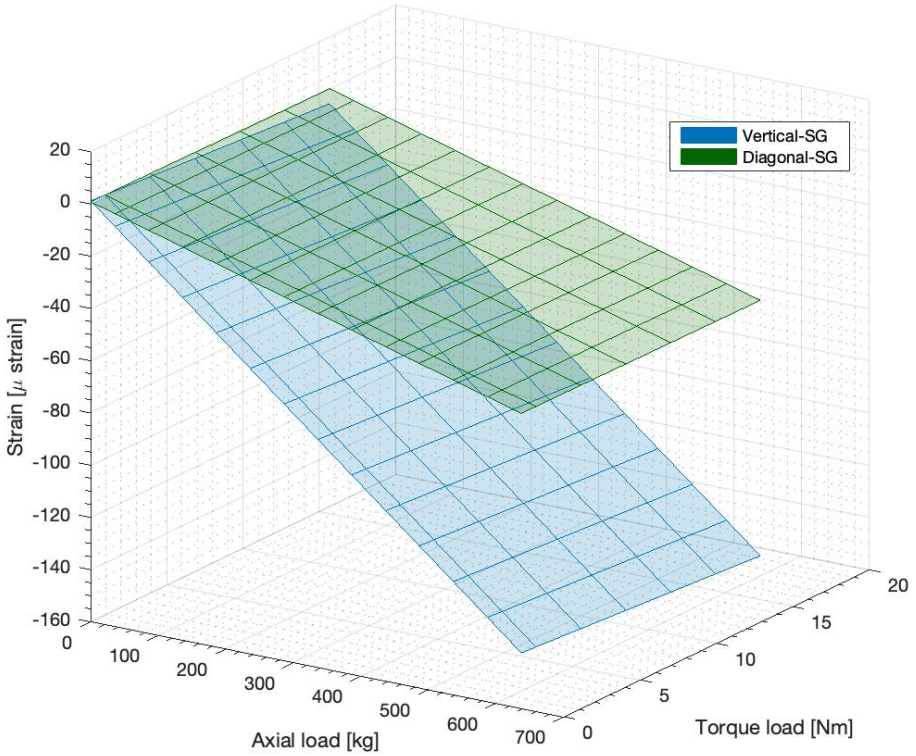

Figure 5.6: The two resulting planes for the output of the vertical-SGs and diagonal-SGs.

Equations 5.5 and 5.6 are a pair of equations that can be solved for the two unknowns. The force is given by

$$F = \frac{A_{d,t} \cdot \epsilon_{vertSG} - A_{v,t} \cdot \epsilon_{diagSG} + (A_{v,t} \cdot (B_{d,a} + B_{d,t}) - A_{d,t} \cdot (B_{v,a} + B_{v,t}))/2}{A_{v,a} \cdot A_{d,t} - A_{v,t} \cdot A_{d,a}} \qquad [kg] \tag{5.7}$$

New coefficients are introduced to simplify the equation, so the force may be expressed as

$$F = C_{f,1} \cdot \epsilon_{vertSG} + C_{f,2} \cdot \epsilon_{diagSG} + C_{f,3} \quad \pm d_f \qquad [kg] \tag{5.8}$$

where the coefficients expressed in known terms and their numerical values can be found in Table 5.2. The deviation in equations 5.5 and 5.6 will follow as well, and the resulting deviation d_f is calculated with by the the *Root Sum Square* method, given by

$$d_f = \left(\left(C_{f,1} \cdot \frac{(B_{v,a} - B_{v,t})}{2} \right)^2 + \left(C_{f,2} \cdot \frac{(B_{d,a} - B_{d,t})}{2} \right)^2 \right)^{1/2} \qquad [kg] \tag{5.9}$$

Coefficient	In terms of $A_{i,j}$ and $B_{i,j}$	Numerical value
$C_{f,1}$	$\frac{A_{d,t}}{A_{v,a}\cdot A_{d,t}-A_{v,t}\cdot A_{d,a}}$	2.3003
$C_{f,2}$	$\frac{-A_{v,t}}{A_{v,a}\cdot A_{d,t}-A_{v,t}\cdot A_{d,a}}$	- 19.9917
$C_{f,3}$	$\frac{A_{v,t}\cdot(B_{d,a}+B_{d,t})-A_{d,t}\cdot(B_{v,a}+B_{v,t})}{2\cdot(A_{v,a}\cdot A_{d,t}-A_{v,t}\cdot A_{d,a})}$	6.9624
d_f	Equation 5.9	7.9116

Table 5.2: The numerical values of the coefficients in the preliminary calibration equation for axial load.

The torque is given by

$$T = \frac{-A_{d,a}\cdot\epsilon_{vertSG} + A_{v,a}\cdot\epsilon_{diagSG} + (-A_{v,a}\cdot(B_{d,a}+B_{d,t}) + A_{d,a}\cdot(B_{v,a}+B_{v,t}))/2}{A_{v,a}\cdot A_{d,t} - A_{v,t}\cdot A_{d,a}} \quad [\mathrm{N}\cdot\mathrm{m}] \tag{5.10}$$

New coefficients are introduced to simplify the equation, so the torque may be expressed as

$$T = C_{t,1}\cdot\epsilon_{vertSG} + C_{t,2}\cdot\epsilon_{diagSG} + C_{t,3} \quad \pm d_t \qquad [\mathrm{N}\cdot\mathrm{m}] \tag{5.11}$$

where the coefficients expressed in known terms and their numerical values can be found in Table 5.3, and the deviation is calculated by

$$d_t = \left(\left(C_{t,1}\cdot\frac{(B_{v,a}-B_{v,t})}{2}\right)^2 + \left(C_{t,2}\cdot\frac{(B_{d,a}-B_{d,t})}{2}\right)^2\right)^{1/2} \qquad [\mathrm{N}\cdot\mathrm{m}] \tag{5.12}$$

Coefficient	In terms of $A_{i,j}$ and $B_{i,j}$	Numerical value
$C_{t,1}$	$\frac{-A_{d,a}}{A_{v,a}\cdot A_{d,t}-A_{v,t}\cdot A_{d,a}}$	-3.4097
$C_{t,2}$	$\frac{A_{v,a}}{A_{v,a}\cdot A_{d,t}-A_{v,t}\cdot A_{d,a}}$	9.9483
$C_{t,3}$	$\frac{-A_{v,a}\cdot(B_{d,a}+B_{d,t})+A_{d,a}\cdot(B_{v,a}+B_{v,t})}{2\cdot(A_{v,a}\cdot A_{d,t}-A_{v,t}\cdot A_{d,a})}$	-2.1146
d_t	Equation 5.12	4.3365

Table 5.3: The numerical values of the coefficients in the preliminary calibration equation for torque.

Note that the axial force as a function of the strain is slightly overestimated, and the torque is slightly underestimated. This is because in the process of choosing the planes' point of intersection with the strain axis in equation 5.5 and 5.6, the strain output is slightly underestimated for solely axial load (T=0) and slightly overestimated for solely torque load (F=0). This explains why

equations 5.8 and 5.11, when both SG-pairs have zero output, give 6.96 $\pm$ 7.91 kg of applied axial force and -2.11 $\pm$ 4.34 Nm of applied torque. The deviation is relatively small compared to the maximum axial load of 700 kg, and relatively big compared to the maximum applied torque of 16 Nm. As for the previous equations, this is due to the best fit lines not crossing the strain axis at exactly zero and the need for approximation. Conveniently, if the ATMD is installed at TTL, it will always be applied a minimum of 50 kg of axial load as it will carry the weight of the turbine runner, the shaft, and other parts. This makes the strain gauges always to give output bigger than zero, which makes the deviations relatively lower.

The upper and lower uncertainty bands in Figure 5.4 and 5.5 are unrelated to the deviations in the preceding equations and are results of the uncertainty due to hysteresis, zero deviation, and repeatability, described in section 4.1. As these lines also vary with both axial and torque load, they must be calculated in the same matter as the procedure leading to equation 5.8 and 5.11. In short, the coefficients describing the upper and lower uncertainty bands are combined to form an upper and a lower deviation plane in three dimensions. The intersection with the strain axis is chosen to be the maximum and minimum value for the upper and lower deviation, respectively. Then the equations are solved to be functions of the measured strain values. See Appendix D for the full deduction. In the calculations of the upper and lower uncertainty limits, the deviations in equation 5.8 and 5.11 are accounted for, and may be disregarded.

The final calibration equations are given in the following. The axial force is given by

$$F = C_{f,1} \cdot \epsilon_{vertSG} + C_{f,2} \cdot \epsilon_{diagSG} + C_{f,3} \qquad [kg] \tag{5.13}$$

the upper uncertainty limit is given by

$$F_{Upper} = C_{f,1,up} \cdot \epsilon_{vertSG} + C_{f,2,up} \cdot \epsilon_{diagSG} + C_{f,3,up} \qquad [kg] \tag{5.14}$$

and the lower uncertainty limit of the axial force is given by

$$F_{Lower} = C_{f,1,low} \cdot \epsilon_{vertSG} + C_{f,2,low} \cdot \epsilon_{diagSG} + C_{f,3,low} \qquad [kg] \tag{5.15}$$

The torque is given by

$$T = C_{t,1} \cdot \epsilon_{vertSG} + C_{t,2} \cdot \epsilon_{diagSG} + C_{t,3} \qquad [\mathrm{N \cdot m}] \tag{5.16}$$

the upper uncertainty limit is given by

$$T_{Upper} = C_{t,1,up} \cdot \epsilon_{vertSG} + C_{t,2,up} \cdot \epsilon_{diagSG} + C_{t,3,up} \qquad [\mathrm{N \cdot m}] \tag{5.17}$$

and the lower uncertainty limit of the torque is given by

$$T_{Lower} = C_{t,1,low} \cdot \epsilon_{vertSG} + C_{t,2,low} \cdot \epsilon_{diagSG} + C_{t,3,low} \qquad [\mathrm{N \cdot m}] \tag{5.18}$$

where the numerical values of the coefficients are found in Table 5.4.

Coefficient	Numerical value
$C_{f,1}$	2.3003
$C_{f,2}$	- 19.9917
$C_{f,3}$	6.9624
$C_{f,1,up}$	2.3512
$C_{f,2,up}$	-19.9301
$C_{f,3,up}$	50.9491
$C_{f,1,low}$	2.2627
$C_{f,2,low}$	-19.9610
$C_{f,3,low}$	-20.2542
$C_{t,1}$	-3.4097
$C_{t,2}$	9.9483
$C_{t,3}$	-2.1146
$C_{t,1,up}$	-3.4812
$C_{t,2,up}$	10.1291
$C_{t,3,up}$	-16.4188
$C_{t,1,low}$	-3.3560
$C_{t,2,low}$	9.8035
$C_{t,3,low}$	7.5711

Table 5.4: The numerical values of the coefficients in the final calibration and uncertainty equations 5.13 to 5.18.

For zero output from the strain gauges, the upper and lower deviation of the applied force is 51 kg and -20 kg, and the deviation of applied torque is 7.6 Nm and -16 Nm. It can be seen in Figure 5.4 that the slope of the upper RSS-deviation line for the diagonal-SGs has such a small negative incline that the point of intersection with the zero-strain-line is at the point of about 40 kg of axial load. This is one of the contributors to the big deviations.

A numerical example is used to demonstrate the use equations 5.14 to 5.18. For an unknown combination of axial load and friction torque, the vertical-SGs may give an output of -100 μstrain, and the diagonal-SGs may give an output of -33 μstrain. This case is visualized in Figure 5.7 and Figure 5.8, where the blue and green lines represent all possible combinations of axial load and friction torque that could give each strain gauge's output. The intersection of these two lines gives the answer.

Equation 5.13 and 5.16 are used to calculate the applied force and torque to be 437 kg and 10.6 Nm respectively. The equations for the upper and lower uncertainties give that the true axial load is between 412 kg and 474 kg, which is -5.6% and +8.4%. The true torque load is between -2.6 Nm and 19.7 Nm, giving a range of 22.3 Nm, which is bigger than the tested range of 0-16 Nm. These numbers conclude that the uncertainties in the system are too high to provide useful information.

From the uncertainty analysis, it can be concluded that the calibration equations for axial load and friction torque must be functions of separate and independent sets of strain gauges. If not, the uncertainty for the strain gauges when applied axial load is present in the final calibration equations for both the axial load and friction torque. As the output from the strain gauges due to axial load is

20 and 60 times as high as for the output due to friction torque for the vertical-SGs and diagonal-SGs, respectively, see Figure 5.4 and 5.5, the relative uncertainty in the friction torque calculations become huge.

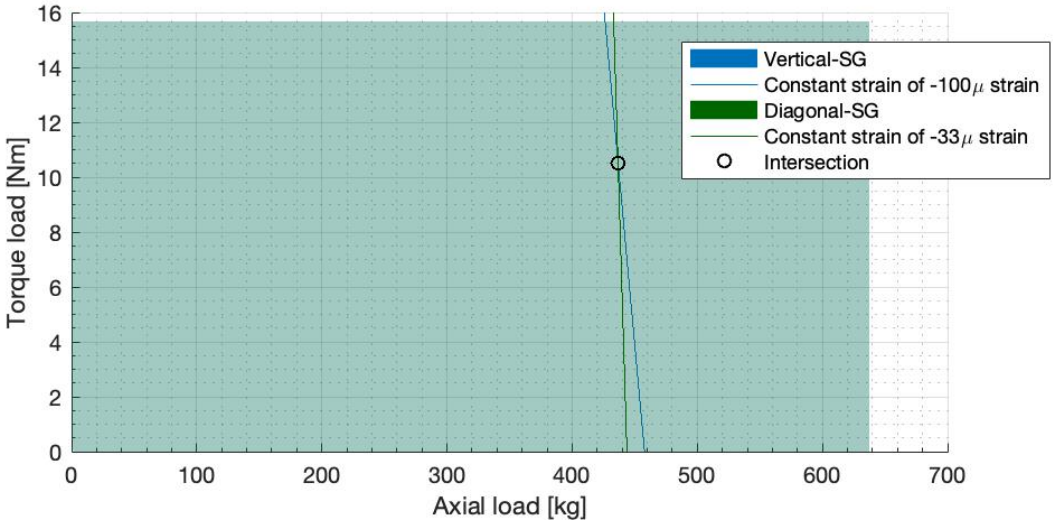

Figure 5.7: The intersection of two constant strain lines emphasized with a circle. The strain axis pointing out put the paper plane.

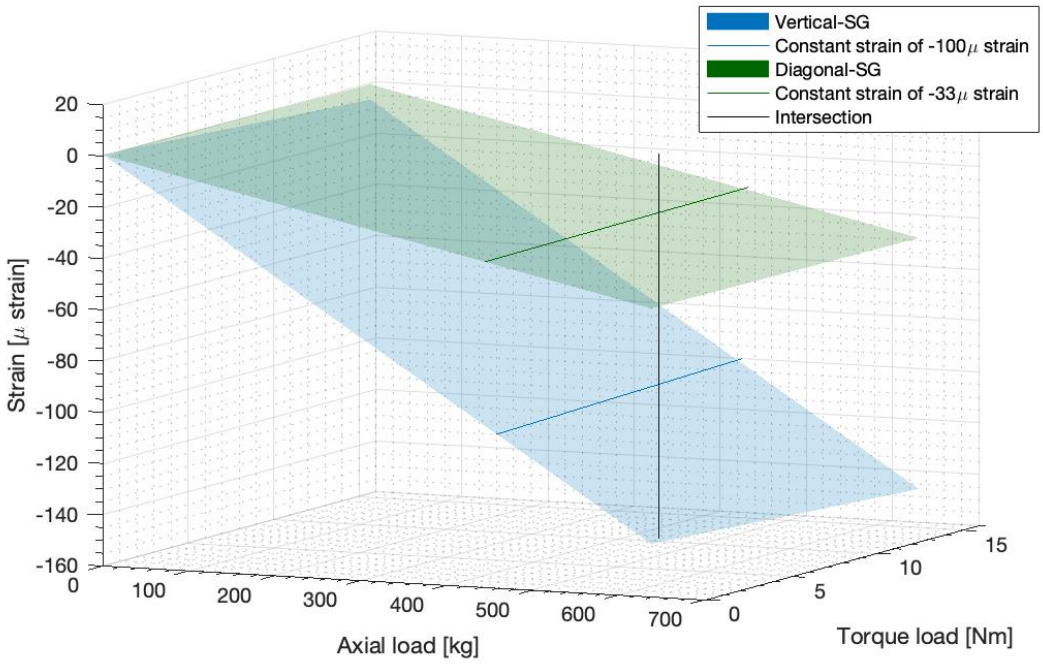

Figure 5.8: The intersection of two constant strain lines emphasized with a line.

5.3 Suggested Final Design

During the work of this thesis, it is obtained knowledge about how the design of the ATMD could be improved so that the output from the strain gauges would be as preferred.

As described in Section 3.2, there was early on decided to investigate designs of 2 mm wall thickness due to the unplanned holes in the wall that would appear if downsizing to 1 mm wall thickness. This limitation resulted in the diagonal slotted holes with the unfortunate strain output and big uncertainties. In hindsight, the design could have been adjusted so that the planned holes covered the unplanned appearing holes. The suggested final design of the ATMD does not have such limitations, so this version is chosen to have a wall thickness of 1 mm, and dimensions as shown in Figure 5.9.

The reason for this design choice is based on numerical results obtained using Ansys Mechanical. When the ATMD is applied both 7000 N and 20 Nm, the strain distribution is as in Figure 5.10 and the direction of the strains are shown as a vector plot in Figure 5.11. The strain distribution for only 20 Nm applied torque is shown in Figure 5.12, and the vector plot of the direction of strains are shown in Figure 5.13. The vector plots show that the strains are working in the same directions as in theory, see section 2.2.2. This means that the calibration equations for the axial load and friction torque will be unrelated and dependent on separate strain gauges, which will cause the uncertainties to be drastically lowered compared to the results from the experimental version. The strains when only applied torque is numerically calculated to be 20 μstrain, which is big enough to be measured. The stress calculated for the maximum amount of forces is 74 MPa, which is 36 % of the yield strength for a stainless steel type with 205 MPa as yield limit [23].

In addition to the final design, there is written a compendium to ease the process of completion. The compendium contains a description of the ATMD, the necessary theoretical foundation, and instruction for how to perform the calibration. The content of the compendium was presented and discussed with technical staff at TTL during a visit to Kathmandu University. A 3D-printed model of the ATMD was used to show the final design and to emphasize the correct placement of the strain gauges. The calibration process was demonstrated, and the steps practiced were: cabling of strain gauges, setup of the logger program, collecting strain data by applying and removing weights, and analysing of the data in Matlab to obtain calibration data.

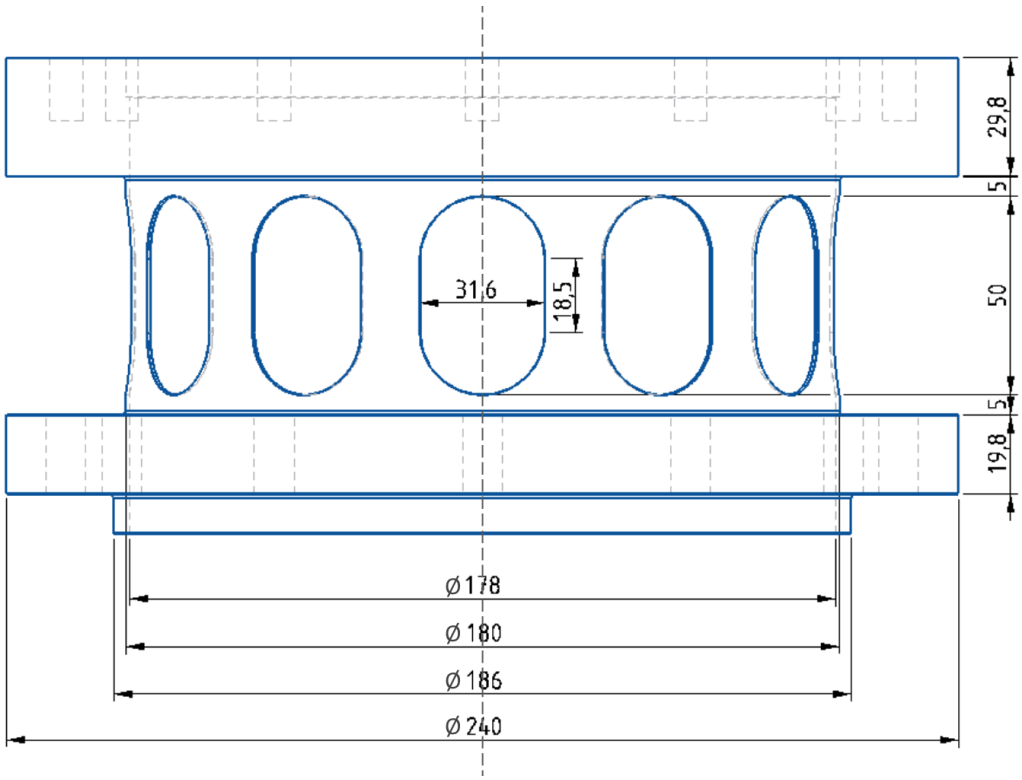

Figure 5.9: The final design of the measuring system.

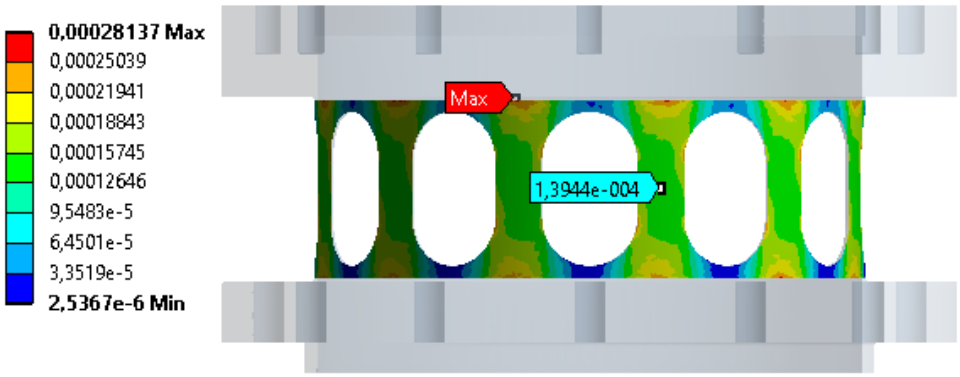

Figure 5.10: The strain distribution when the final design is applied 7000 N and 20 Nm.

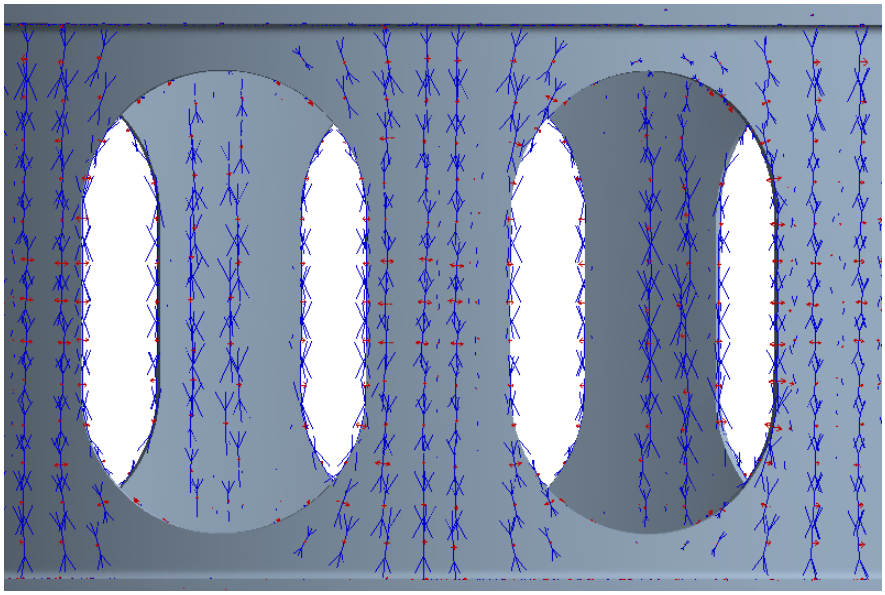

Figure 5.11: Vector plot of the strains when the final design is applied 7000 N and 20 Nm.

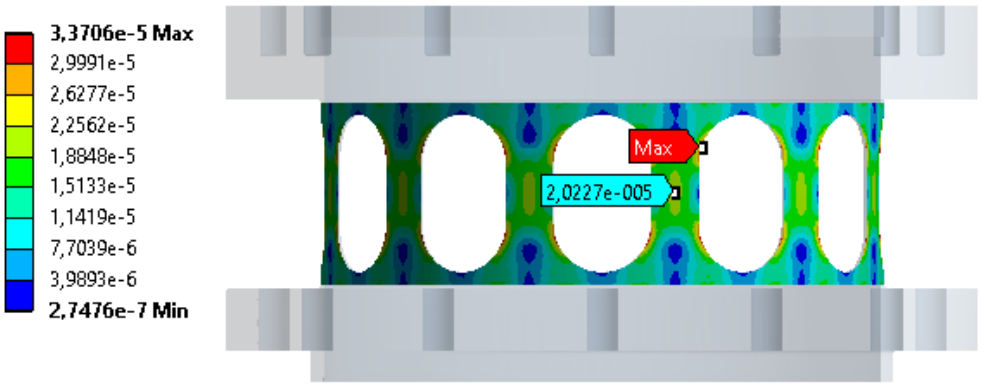

Figure 5.12: Strain distribution when the final design is applied solely 20 Nm.

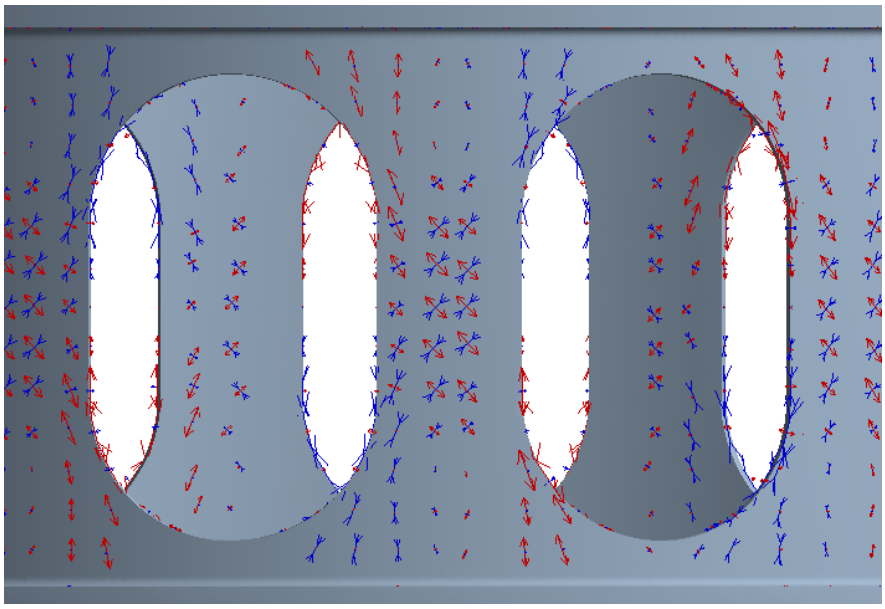

Figure 5.13: Vector plot of the strains when the final design is applied solely 20 Nm.

Chapter 6

Conclusions

The objective of this thesis was to develop a measuring system for axial load and friction torque for the Turbine Testing Lab (TTL) at Kathmandu University (KU), and two designs have been investigated. The initial design, shown in Figure 6.1, was tested in the lab, calibration equations were obtained, and uncertainty analysis was performed. As a result of the insight obtained, an improved design, shown in Figure 6.2, was developed.

The measuring device is a part of the bearing block, placed between the bearing housing and the head cover top, see Figure 1.1. The weight of the runner, shaft and other parts, and the hydraulic axial forces acting on the runner are aggregated to the device as compression. The device is also applied a small torque due to the friction in the bearings. The axial load and the torque are the two sources of strain the device will be measuring with strain gauges. The main challenge is that the strain caused by the axial forces is much larger than the strain caused by the friction torque. The goal was to find a design of the device that was susceptible to the strain caused by both sources while still strong enough to be safe for all operation points in the test rig. By the use of CAD-drawing in Creo Parametric different designs of the device were investigated and tested numerically in Ansys Mechanical.

In the development of the first design, shown in Figure 6.1, the wall thickness was limited to 2 mm. To achieve big enough strains from the torque applied, the slotted holes in the wall had to be diagonal so that two weaker points were grouped into an area of larger strain values. In the experiments, two sets of strain gauges were used. They were placed to measure axial forces and friction torque individually. The slotted holes being diagonal prevented this, which made the final calibration equations dependent on the data from both strain gauge sets. As the strains caused by axial forces were at most 60 times larger than the strains due to torque, the uncertainties became unacceptable. From this, it is confirmed that the calculations of axial load and friction torque must be functions of separate and independent strain gauges. Numerically calculated vector plots of the strains concur with the experimental results, and these types of plots are therefore used in the development of the improved design.

The final design, shown in Figure 6.2, has a wall thickness of 1 mm and vertical slotted holes. The vector plots of the strains working on this design show that the direction matches well with theory. This will cause the calibration equations to be functions of only one strain gauge set each, which will lower the uncertainties drastically. The remaining procedures and possible challenges

are described in detail in the compendium accompanying the final design, see Appendix E. During a visit to Kathmandu University in November 2019, the final design was presented and the calibration process was demonstrated to technical staff at TTL. Hopefully, with the compendium and this demonstration, the staff at TTL feel well equipped to perform the final phase of the development of the measuring system themselves.

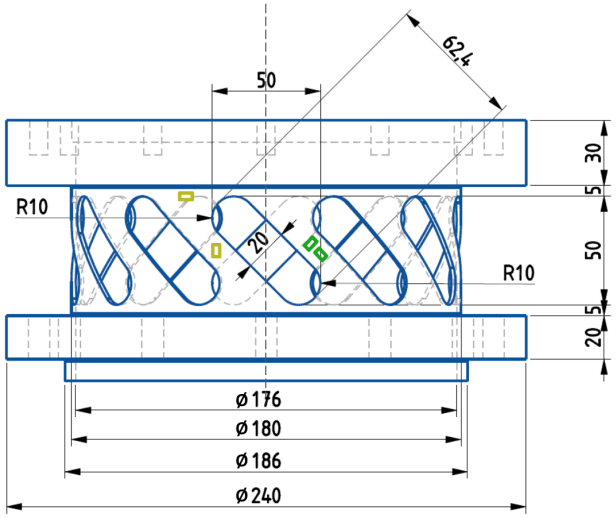

Figure 6.1: The first design of the measuring device with dimensions in millimeter. The yellow and green squares show the placement of the two strain gauge sets.

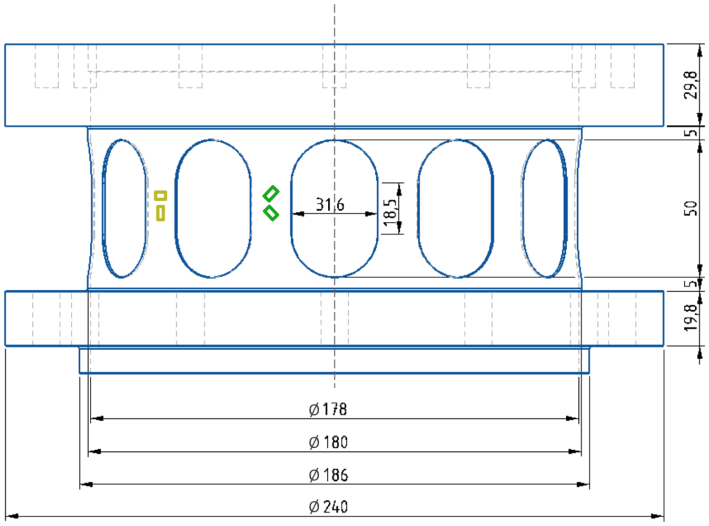

Figure 6.2: The final and recommended design of the measuring device with dimensions in millimeter. The placement of the axial load measuring strain gauges is represented by the yellow squares, and the placement of the friction torque measuring strain gauges is represented by the green squares.

Chapter 7

Further Work

The main work remaining is to test the final design experimentally. The suggested actions are listed and described in detail in the compendium in Appendix E. The method used for uncertainty analysis in this thesis is conservative, so the uncertainties may be lowered if the analysis is redone with a different method. Another aspect to consider is the fact that there is water on the inside of the ATMD due to drainage of the seal water. In the compendium, there is suggested some possible solutions. A possible impact of electromagnetic interference from the surroundings should also be investigated. In this thesis, the semi-conductor strain gauge types are rejected. As the general opinion of these types is good, it might be useful to investigate possible actions that may lower the hysteresis effects.

Production:

- It is preferred that the final design, shown in Figure 6.2, is made of stainless steel.

Calibration:

- Order (at least) 8 strain gauges that are matched to the material of the ATMD
- Attach strain gauges
- Obtain weights of 700 kg, calibrate and systematically label the weights
- Make experimental setups so that the ATMD can be applied purely axial load and purely torque load
- Perform axial load and torque load data collection
- Analyse the gathered data to obtain calibration equations and to perform uncertainty analysis. If the results are satisfactory, linear, and with low uncertainties, the device may be installed.

Installation:

- Decide a solution to the challenge with water on the inside of the ATMD
- Replace the Axial Block Spare Section with the ATMD and update the existing drawings and CAD-models.
- Implement the output from the ATMD in the main data acquisition program in the control room with the calibration equation calculating axial load and friction torque.

Bibliography

[1] S. Haugan. (24.07.2019) *Nepal*. [Online]. Available: https://snl.no/Nepal

[2] NORAD. (10.01.2017) *Nepal*. [Online]. Available: https://norad.no/landsider/asia-og-oseania/nepal/

[3] A. Vinjar and K. Rosvold. (22.09.2018) *Vannkraft*. [Online]. Available: https://snl.no/vannkraft

[4] NTNU. (2019) *Vannkraftlaboratoriet*. [Online]. Available: https://www.ntnu.no/ept/om_vklab

[5] International Electrotechnical Commision, *Hydraulic turbines, storage pumps and pump-turbines - Model acceptance tests*, 1999.

[6] A. Kjerschow, *Development of a Francis Turbine Test Rig at Kathmandu University*. NTNU, 2017.

[7] Kathmandu University. (2019) *Background and Introduction*. [Online]. Available: http://ttl.ku.edu.np/background-and-introduction/

[8] B. R. Halwai, *Design of a Francis turbine test rig*. NTNU, 2012.

[9] I. J. Rasmussen, *Design of a Francis Model Test Rig at Kathmandu University*. NTNU, 2014.

[10] M. Selmurzaev, *Design of the measurment setup for the friction torque and axial load on the Francis turbine test rig*. NTNU, 2016.

[11] M. Grefstad, *Development of a Francis Turbine Test Rig at Kathmandu University*. NTNU, 2017.

[12] J. Bådsvik, *Development of a Francis Turbine Test Rig at Kathmandu University*. NTNU, 2019.

[13] H. Johansen. (08.04.2010) *Lager*. [Online]. Available: https://docplayer.me/10802488-Henning-johansen-lager.html

[14] A. Engøy, *Development of a Francis Turbine Test Rig at Kathmandu University*. NTNU, 2019.

[15] H. Brekke, *Pumper og Turbiner*. Vannkraftlaboratoriet NTNU, 2003.

[16] K. Bell, *Konstruksjonsmekanikk Del 2 Fasthetslære*. Fagbokforlaget, 2015.

[17] A. J. Wheeler and A. R. Ganji, *Introduction to Engineering Experimentation*. Pearson, 2010.

[18] K. Hoffmann. (2019) *Applying the Wheatstone Bridge Circuit*. [Online]. Available: http://eln.teilam.gr/sites/default/files/Wheatstone%20bridge.pdf

[19] K. Jakobsen, *Måling med strekklapper*. Tapir, 1979.

[20] Physikalisch Technische Bundesanstalt. (2004) *Calibration of Pressure Gages*. [Online]. Available: https://www.ptb.de/cms/fileadmin/internet/dienstleistungen/dkd/archiv/Publications/Guidelines/DKD-R_6-1_2016_englisch.pdf

[21] Kulite. (2011) *Kulite Strain Gauge Manual*. [Online]. Available: https://www.kulite.com/assets/media/2017/05/StrainGageManualDigital.pdf

[22] Hebei Jinshi. (2019) *DIN ST52-2 Angle Steel*. [Online]. Available: https://www.steel-sections.com/steelsections/st52-3-angle-steel.html

[23] Atlas Steels Technical Department. (2013) *Stainless Steel Grade Datasheets*. [Online]. Available: http://www.worldstainless.org/Files/issf/non-image-files/PDF/Atlas_Grade_datasheet_-_all_datasheets_rev_Aug_2013.pdf

[24] Tokyo Measuring Instruments Lab, *Datasheet: TML Strain Gauge Test Data*, 2018.

[25] National Instruments. (2019) *Connecting Strain Gages to a DAQ Device*. [Online]. Available: http://www.ni.com/getting-started/set-up-hardware/data-acquisition/strain-gages

[26] Ju Feng Special Steel Co., Ltd. (2019) *SS400*. [Online]. Available: https://www.jfs-steel.com/en/product/SS400/SS400.html

[27] W. Bowden. (28.09.2016) *How to battle drift in bonded foil strain gauge-based sensors*. [Online]. Available: https://www.controleng.com/articles/how-to-battle-drift-in-bonded-foil-strain-gauge-based-sensors/

[28] J. Hass, M. D. Weir, and G. B. Thomas Jr., *Calculus Part 2*. Pearson, 2009.

[29] M. Rovitto. (December 2016) *4.1.2 Principles of Finite Element Method*. [Online]. Available: http://www.iue.tuwien.ac.at/phd/rovitto/node63.html

[30] Ansys Inc. (2009) *Ansys Fluent 12.0 Getting Started Guide*. [Online]. Available: https://www.afs.enea.it/project/neptunius/docs/fluent/html/gs/node19.htm

Appendices

A Numerical Analysis

This section is taken from this thesis' author's project thesis as the procedure is the same for both theses [14].

Ansys Academic Mechanical is used for the numerical analysis, with the purpose of testing the ATMD digitally for the forces to be tested experimentally. The theory in this section is from conversations with Hove in EDRMedeso.

In reality, forces and strain propagate through a body evenly and continuous, but computations of these forces performed by computers must be handled at discrete positions and cannot be exactly as in reality. These discrete points represent the mesh and make up the grid the computer is computing through. The more discrete points in the grid, the finer mesh and the closer to reality the computation is, see Figure A.1. Unfortunately, it is not possible to have thousands of millions of nodes as the execution time of the computer grows out of manageable proportions and it is, therefore, necessary to make a mesh economically. This means, in areas of the modeled body where changes are big, there should be many nodes, and in areas with small changes, the steps between each node can be bigger.

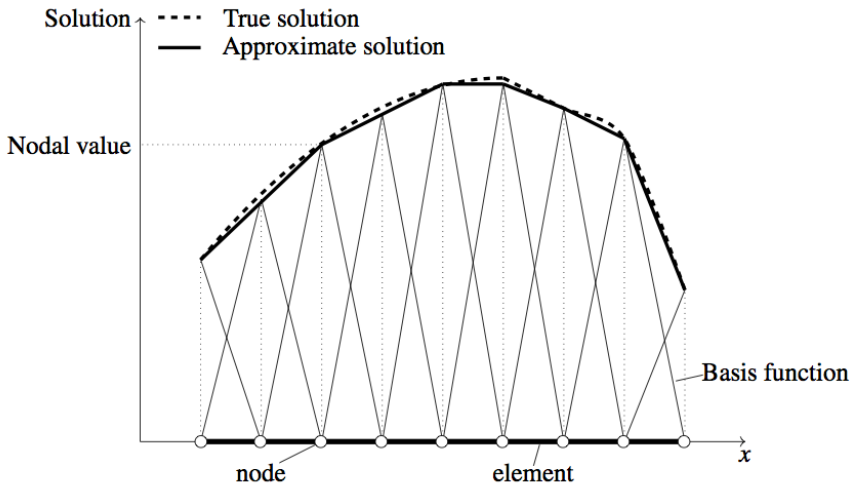

Figure A.1: Discrete points on a continuous line [29].

To check whether the number of nodes chosen in different areas was good, it is possible to test for convergence in a calculated value. Convergence works in the way that the program first calculates the desired value in all the nodes. Then, for areas where the calculated values in the neighboring nodes have a big difference, the program makes a refinement and redo the calculation. If the change after the refinement is small, the original number of nodes was enough and the values first calculated close to the truth. If the change is big, then the first calculation is too far from the truth and the program makes another refinement.

Another way to check the mesh quality is to check the element quality. A score is given to each element based on its shape, where a good score is given to an element that is not twisted or warped. Ansys Mechanical uses four different element types, the two most common are presented in Figure

A.2. The hexahedron-type is considered as the best, but in places of the geometry where hexahedrons are not possible to use, Ansys Mechanical patch the geometry up with wedges which is the worse type. The hexahedron-dominant method is, therefore, best for geometries where the number of wedges is small, which is typical square-like geometries. The tetrahedron-type is the second best element type and pyramids, which is considered as the third best, are the type used where tetrahedrons cannot be used. The tetrahedron-dominant method is more flexible and therefore a good choice for complicated or circular-like geometries like the ATMD.

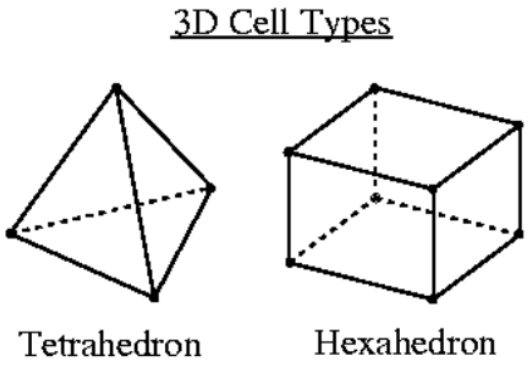

Figure A.2: The two main element types [30].

To start constructing the mesh an automated tetrahedron-dominant mesh was generated with a global element size of 5 mm and this mesh was then improved by several techniques. By applying a convergence condition in the strain calculation of the whole body, the areas that needed smaller elements were highlighted. Since the forces are transferred through the screw holes and the edges between the flange and the middle part, these were areas where the element size was reduced. The belt in the middle of the ATMD was also given smaller element size since this was an area interest. The final mesh was given a convergence condition on the strain calculation in the whole body, and the mesh converged at the first iteration with a change of less than 1%, which means that the originally mesh before any refinements have small enough elements in the necessary places. The average element quality was 0.77 which is a good score, meaning that most of the elements are satisfactorily shaped.

The resulting mesh is given in Figure A.3 and has 1.1 million nodes and 0.70 million elements. The placement of the strain gauges is in the middle belt between the blue dotted lines. A mesh independent test was performed to check the validity of this mesh, and the value used for comparison was the maximum strain in the belt area for a force of 7000 N. The reason for this choice was based on the fact that the belt area is the area of most interest and the maximum force applied would give the biggest error if the final mesh was poorly made. The test mesh had element size of 1 mm, resulting in 5.1 million nodes and 3.4 million elements. The calculated maximum strain in the belt area for the test mesh was 26.686 μstrain and the calculated maximum strain for the final mesh was 26.774 μstrain giving a deviation of 0.088 μstrain. This confirms mesh independence and by only using a fifth of the number of nodes, the final mesh is economically made.

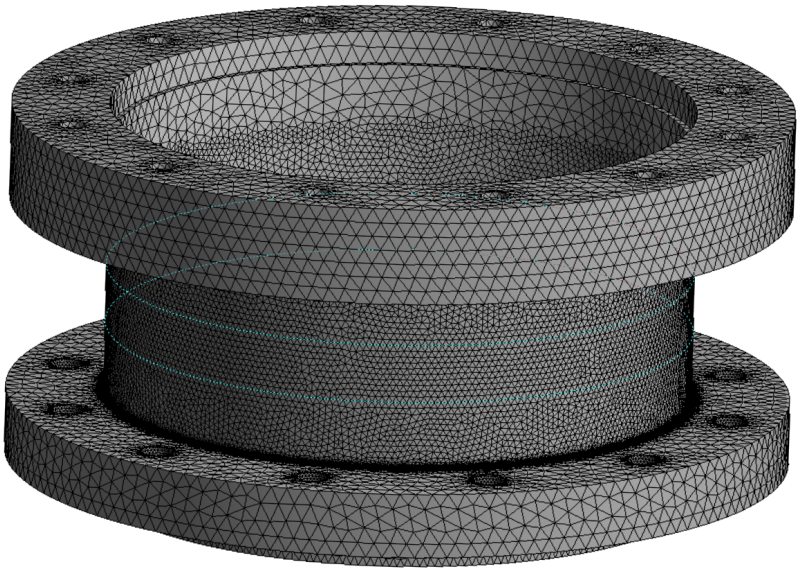

Figure A.3: The final mesh.

B Elaboration of Test Case 2

This section discusses the results from experimental case 2 and is an elaboration of section 4.2.

Axial Load Applied

Output from Half-Bridge Diagonal-SGs

The temperature development during axial load applied to the half-bridge diagonal-SGs is shown in Figure B.1 and the recorded strain with a linear best fit line is shown in Figure B.2. Even though the strains in case 1 and 2 have opposite sign, they are both applied the same compressing force, and the absolute value of the strains are comparable. This change to positive strain values is not intentional and can be disregarded as it is simply due to the wires being cabled opposite. It can be seen that the blue series is drifting away from the other measurement series. However, it does not seem like the drifting is caused by the difference in temperature as the warmest and coldest series, the red and green respectively, have the most similar output.

The diagonal-SGs cabled in a half-bridge should have numerical values half the size of the full-bridge as there is half the number of strain gauges applied strain [19], see Chapter 2.2.2 and equation 2.31. For the maximum axial load of 637 kg, the full-bridge diagonal-SGs measured a strain around -50 μstrain, and the red and green measurement series are measuring a maximum strain around 27 μstrain, which is within the expected size. This gives reason to believe that the blue measurement series is not to be trusted, as the maximum measured strain is above 35 μstrain, even though this series looks more linear than the others.

In Figure B.3, it can be seen that repeatability is a big contributor to the uncertainty and the blue measurement series drifting off is the reason for this. This causes a big total uncertainty of above 4 μstrain, see Figure B.4, which is twice as much as the total absolute uncertainty in the full-bridge diagonal-SGs in case 1. Figure B.5 show the best fit line and the total uncertainty in combination. When comparing this figure to the corresponding figure of case 1, Figure 4.11, it can be concluded that to arrange the diagonal-SGs in a half-bridge is a worse alternative for axial load applied.

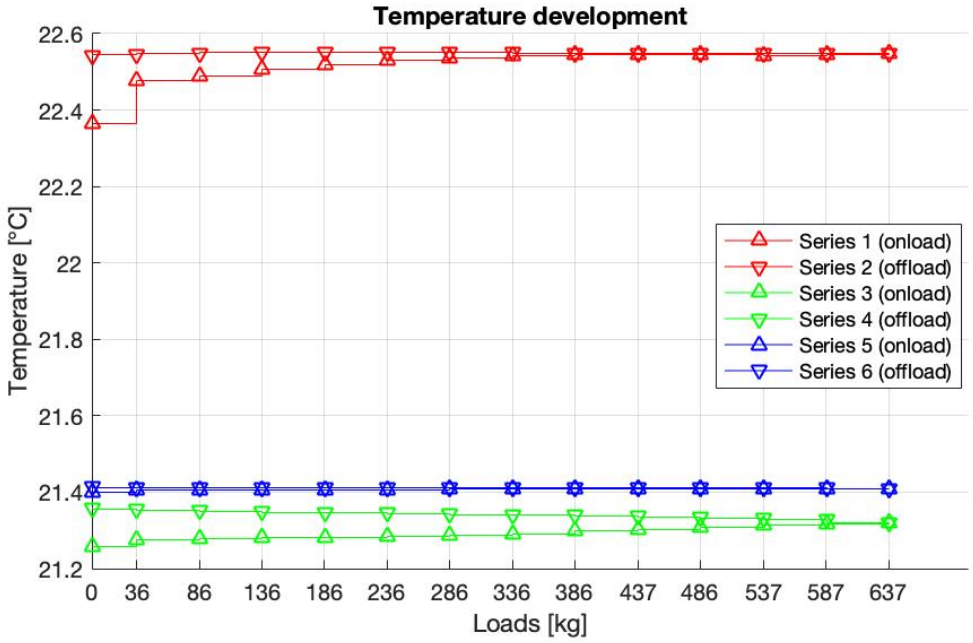

Figure B.1: Case 2: Temperature development during axial load measurements applied to the half-bridge diagonal-SG.

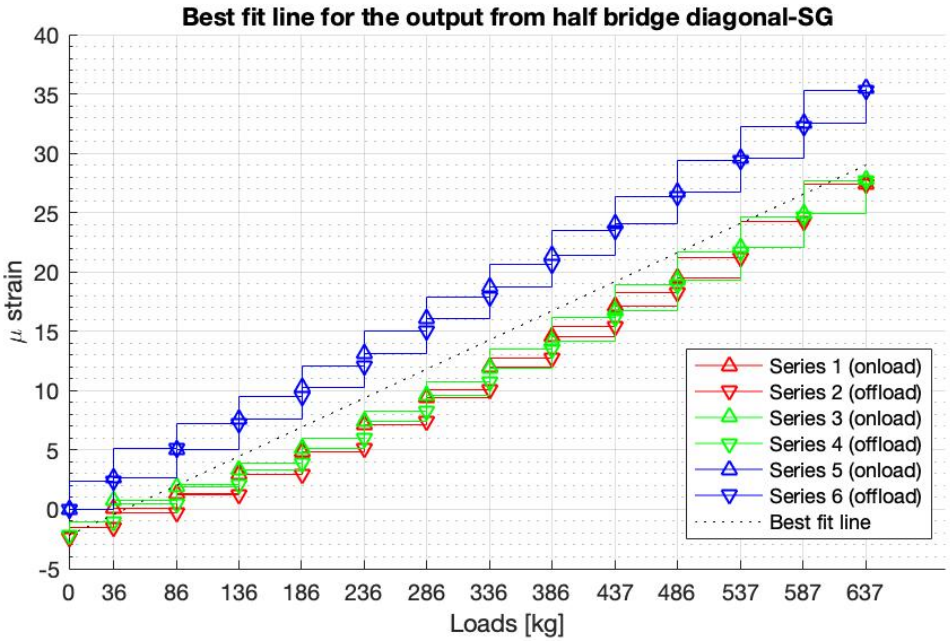

Figure B.2: Case 2: The measured strain from the half-bridge diagonal-SGs with axial load applied with a linear best fit line.

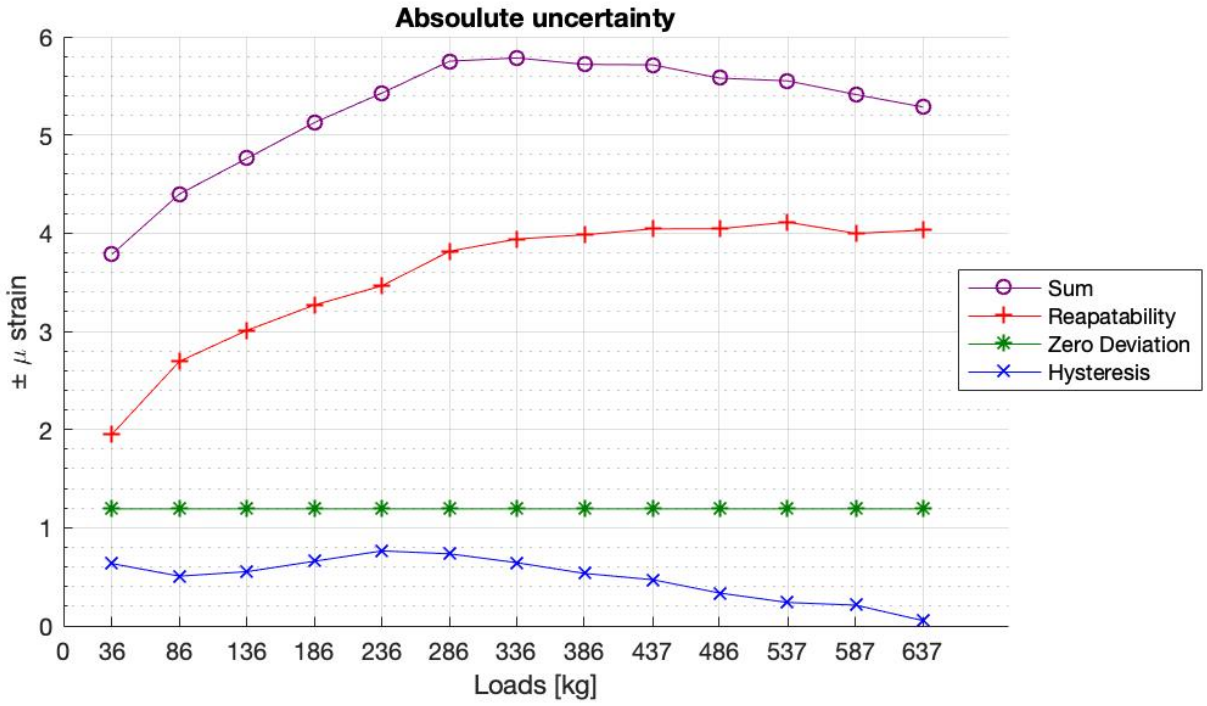

Figure B.3: Case 2: Summation of uncertainty in the half-bridge diagonal-SGs for axial load applied.

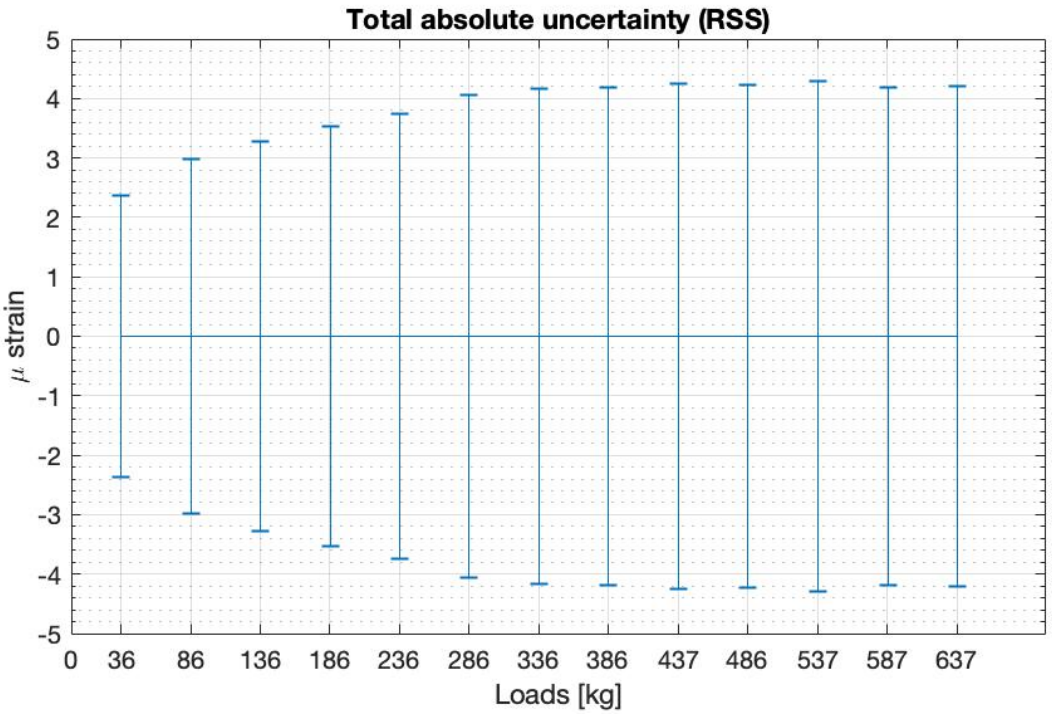

Figure B.4: Case 2: The absolute total uncertainty in the half-bridge diagonal-SGs for axial load applied.

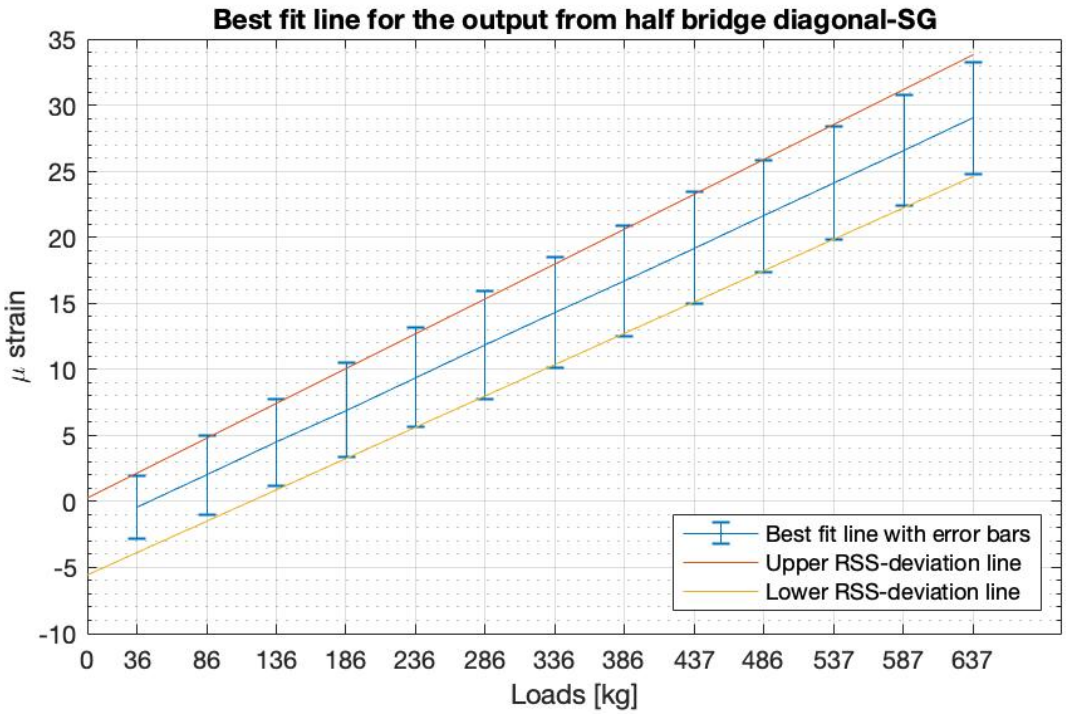

Figure B.5: Case 2: Best fit line with upper and lower total uncertainty for the half-bridge diagonal-SGs with axial load applied.

Torque Load Applied

Output from Half-Bridge Diagonal-SGs

For torque load applied to test case 2, the temperature development is presented in Figure B.6 and the measured strain is presented in Figure B.7. The strain range from -0.8 μstrain to 1.2 μstrain, with relatively large deviations in the strain output. This is mostly due to the green series, and partly the blue series, dropping in strain value as the first torque load is applied. In Figure B.8 it can be seen that the calculated uncertainty is around 0.6 μstrain. This is, in absolute terms, quite low, but it is almost ten times as high as the uncertainty for the full-bridge diagonal-SGs applied torque, case 1, which is around 0.08 μstrain, see Figure 4.19. By that, it can be concluded that case 2 is a worse alternative for torque load as well as for axial load.

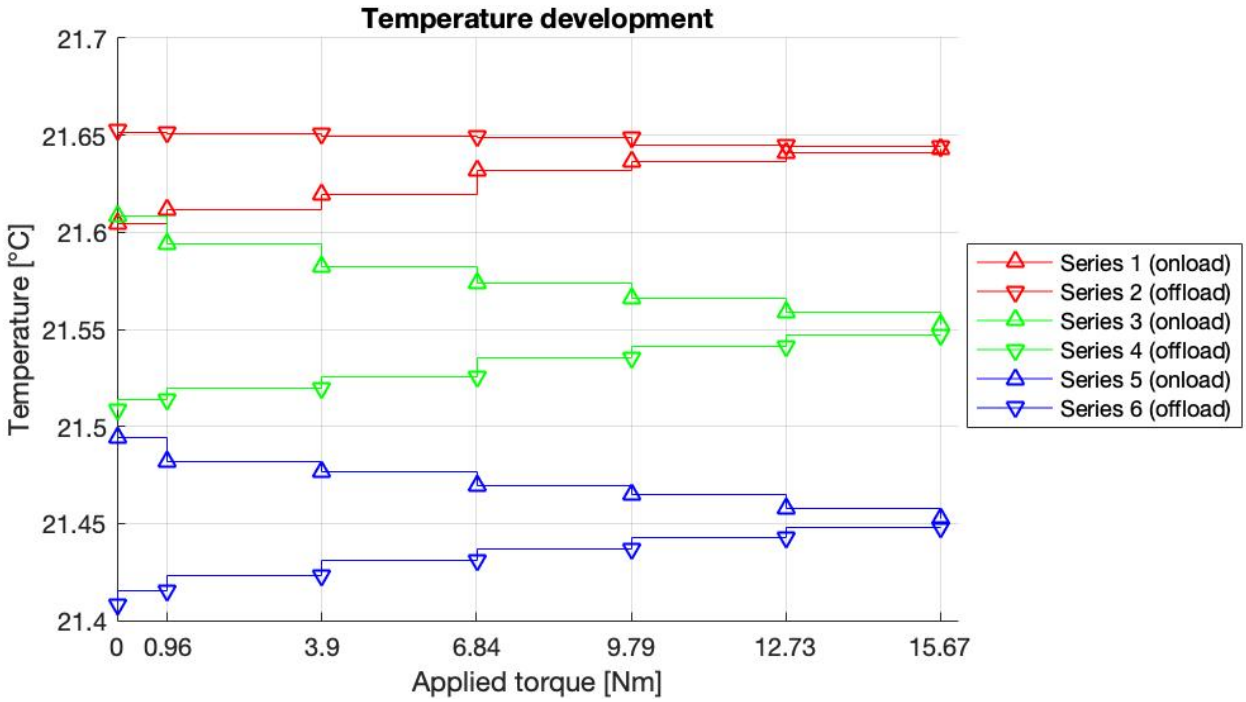

Figure B.6: Case 2: Temperature development during torque load applied.

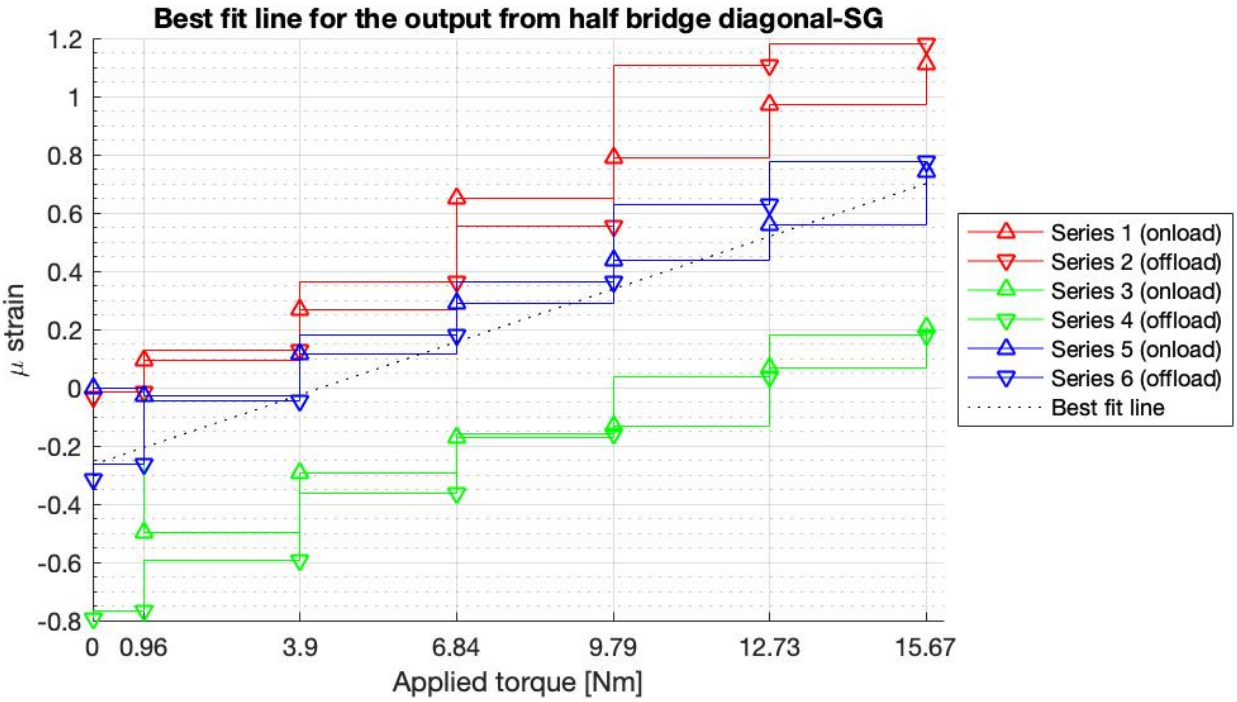

Figure B.7: Case 2: The measured strain from the half-bridge diagonal-SGs applied torque load.

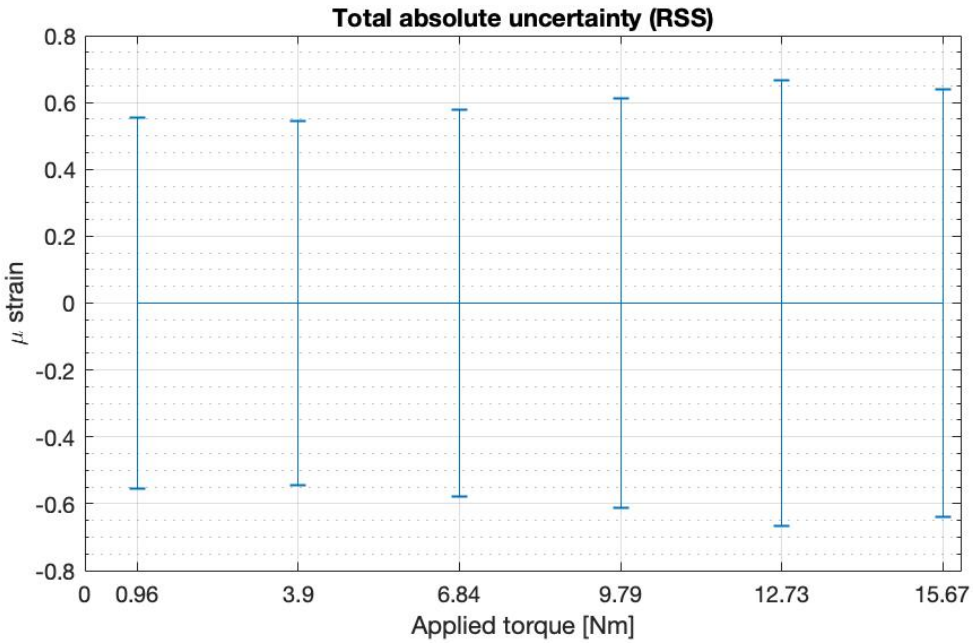

Figure B.8: Case 2: The absolute total uncertainty in the half-bridge diagonal-SGs applied torque load.

C Additional Plots for Test Case 3

Axial Load Applied

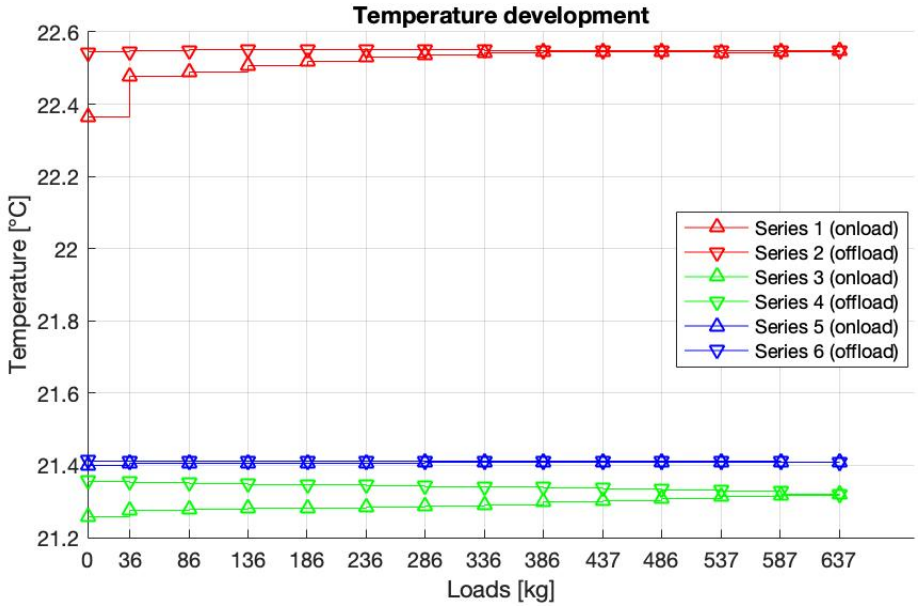

Figure C.1: Case 3: Temperature development during axial load.

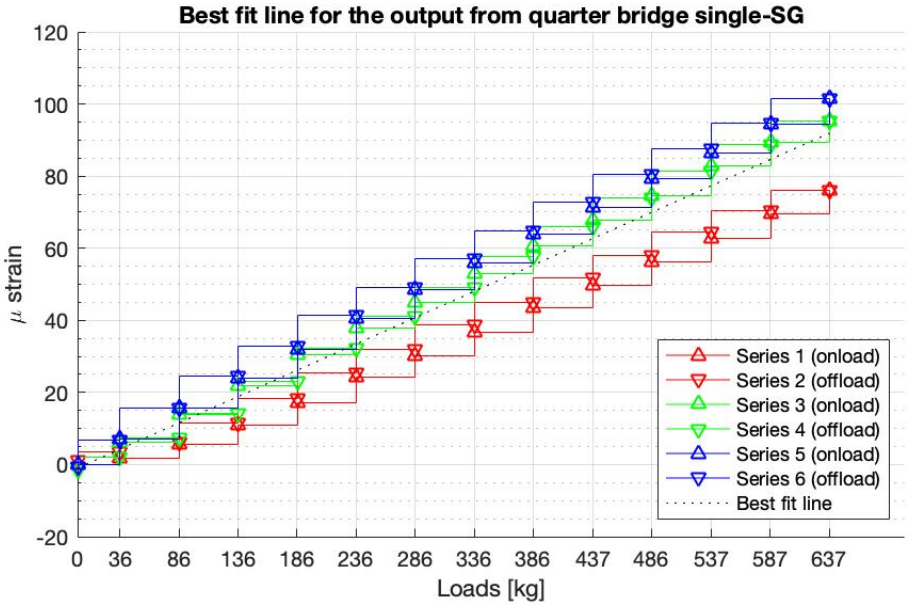

Figure C.2: Case 3: The measured strain from the quarter-bridge single-SG applied axial load.

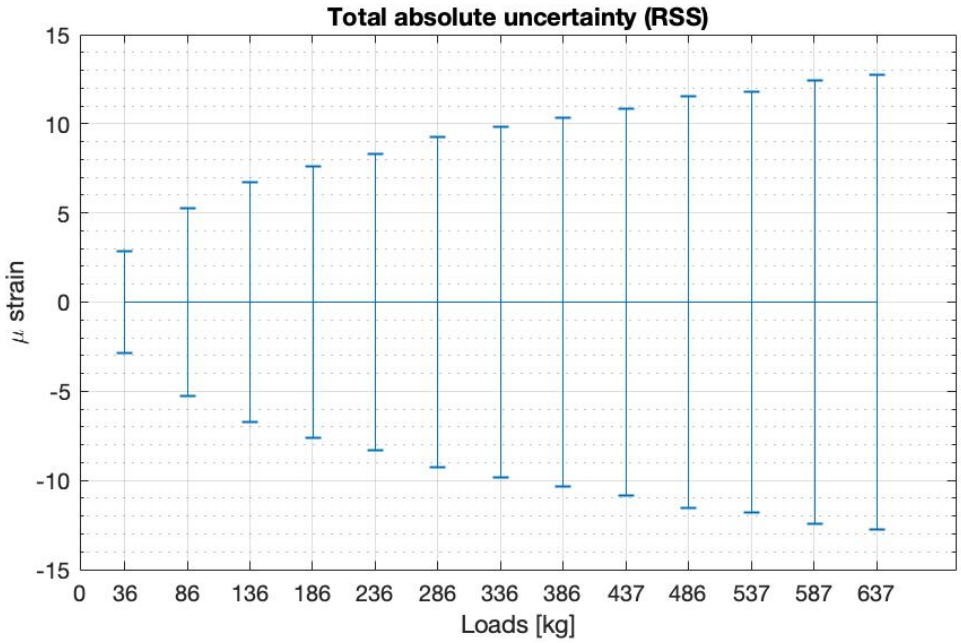

Figure C.3: Case 3: The absolute total uncertainty in the quarter-bridge single-SG applied axial load.

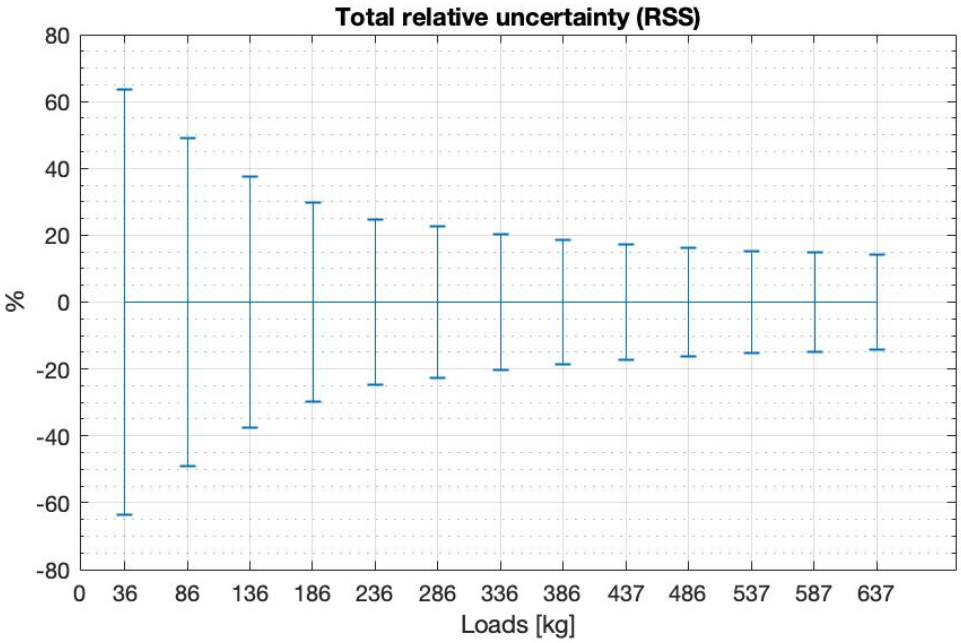

Figure C.4: Case 3: The total uncertainty in the quarter-bridge single-SG applied axial load in percentage of the measured value.

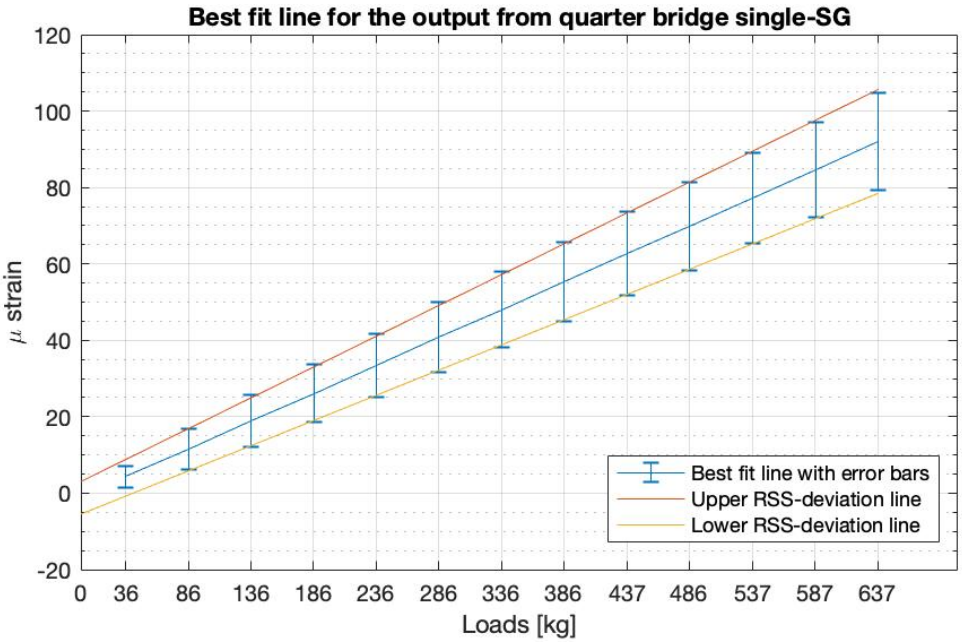

Figure C.5: Case 3: Best fit line with upper and lower total uncertainty for the quarter-bridge single-SG applied axial load.

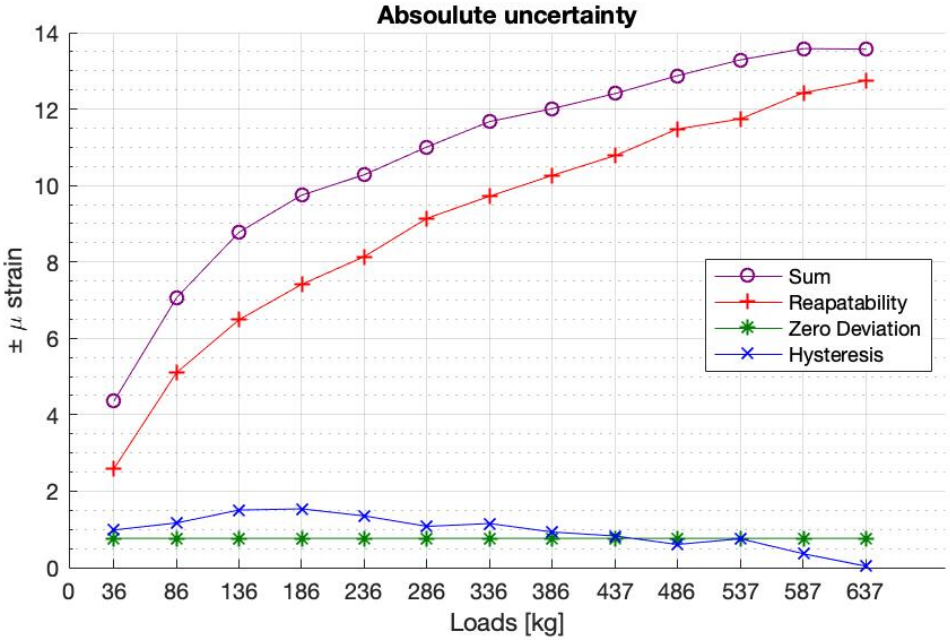

Figure C.6: Case 3: Summation of the uncertainties in the quarter-bridge single-SG applied axial load.

Torque Load Applied

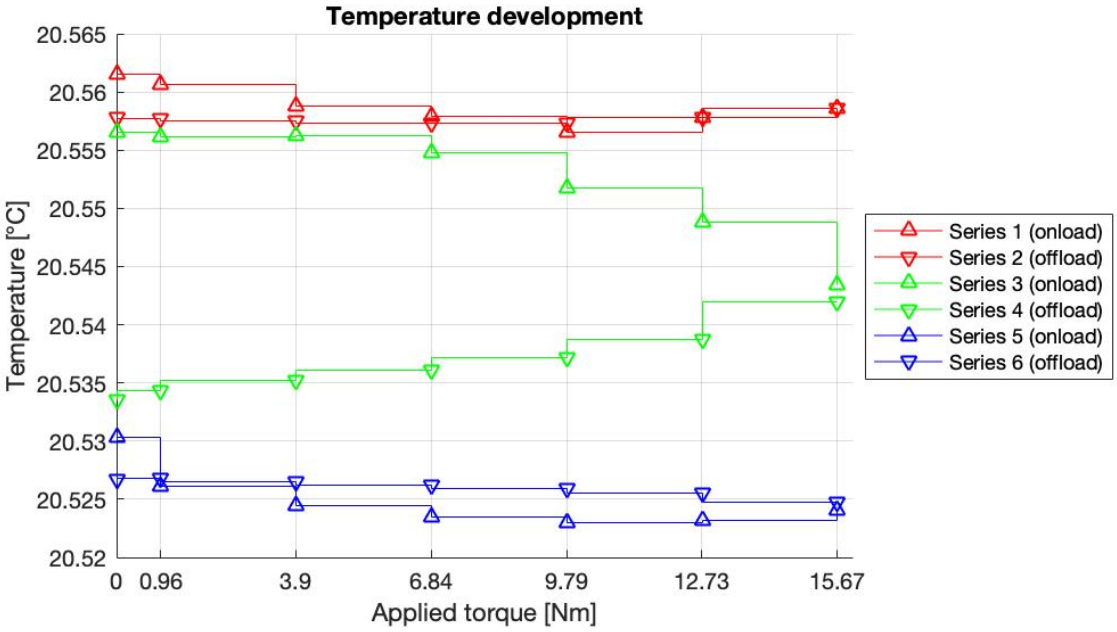

Figure C.7: Case 3: Temperature development during torque load.

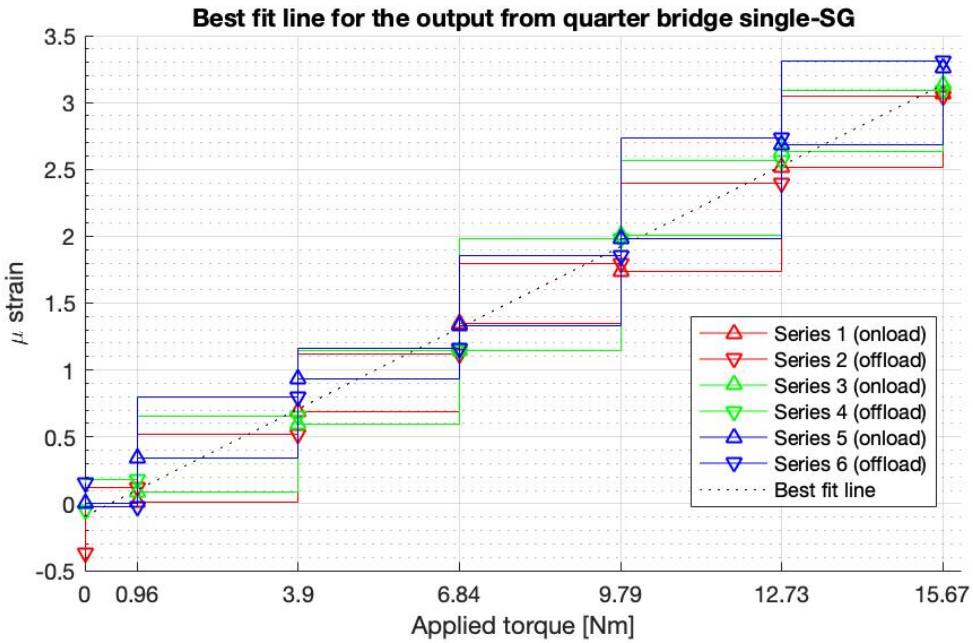

Figure C.8: Case 3: The measured strain from the quarter-bridge single-SG applied torque load.

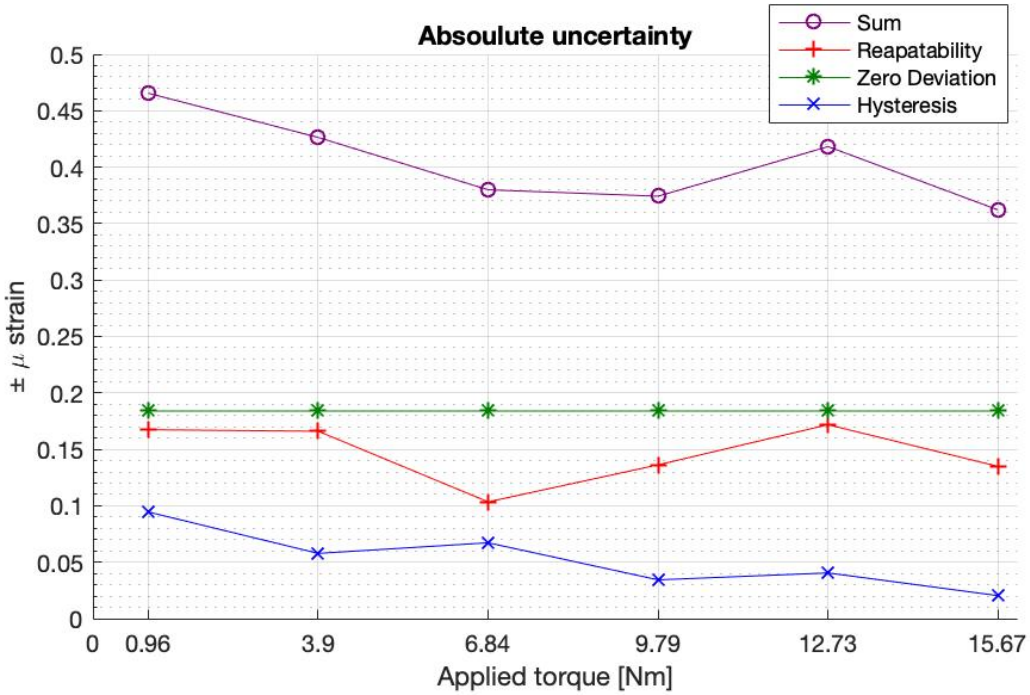

Figure C.9: Case 3: Summation of the uncertainties in the quarter-bridge single-SG for torque load applied.

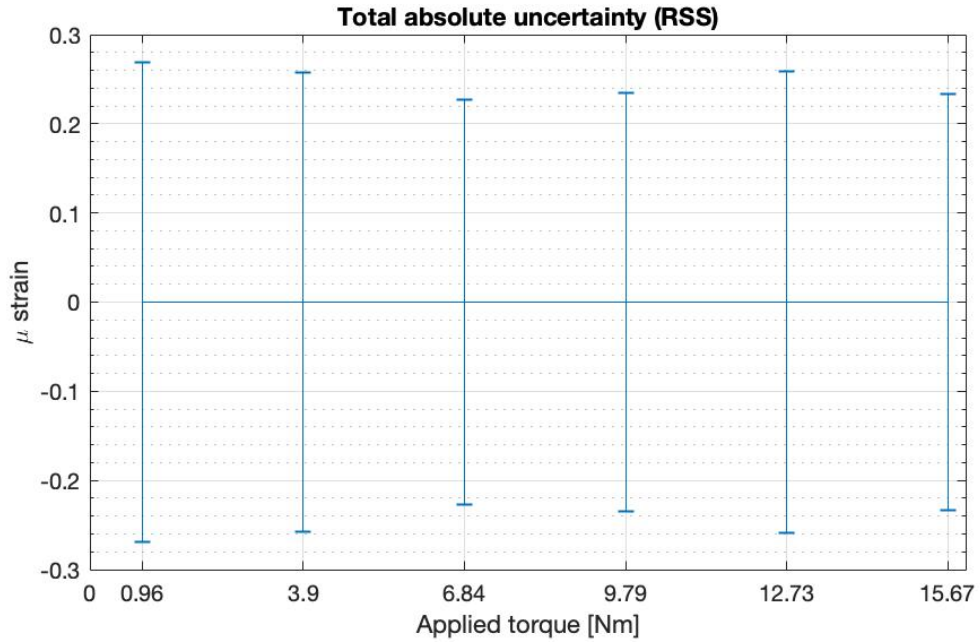

Figure C.10: Case 3: The absolute total uncertainty in the quarter-bridge single-SG applied torque load.

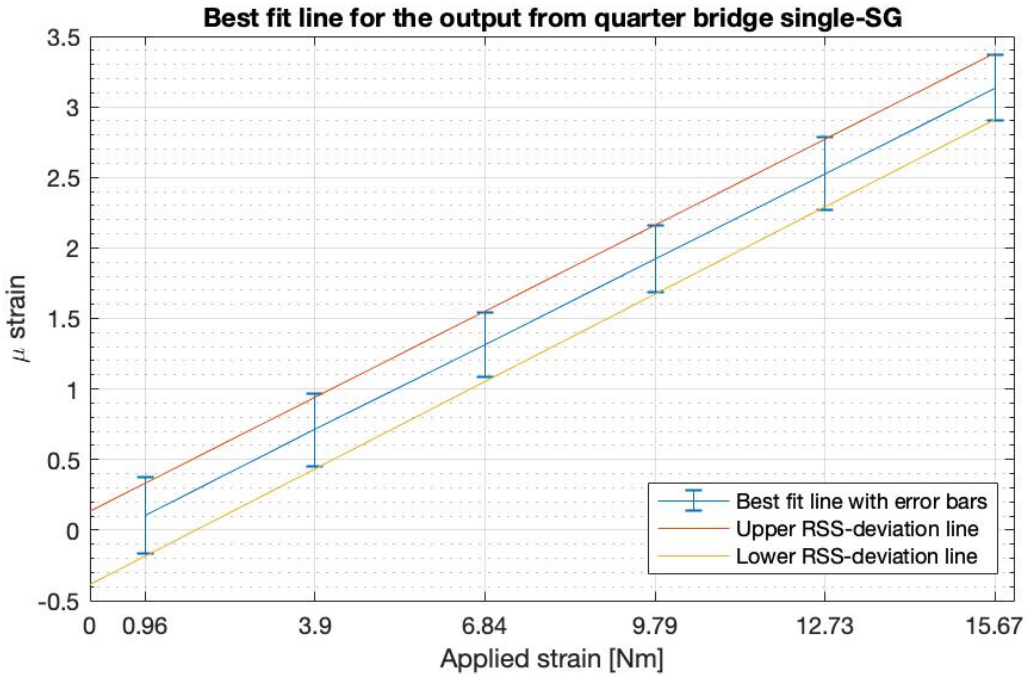

Figure C.11: Case 3: Best fit line with upper and lower total uncertainty for the quarter-bridge single-SG applied torque load.

D Calculations of Uncertainty

This is the complete deduction of the equations giving the uncertainty as a function of the measured strain values, equations 5.14 to 5.18 in chapter 5.2. The best fit lines, shown in Figure D.1 and D.2, are written in the form $y = A \cdot x + B$ and the subscripts in the coefficients *A* and *B* are: *v* and *d* that means vertical and diagonal strain gauges, *a* and *t* that means axial and torque load applied, and *up* and *low* that means upper and lower deviation. When the following equations are simplified and coefficients are introduced, then the first subscript is either *f* or *t* and corresponds to the calculation of force or torque respectively.

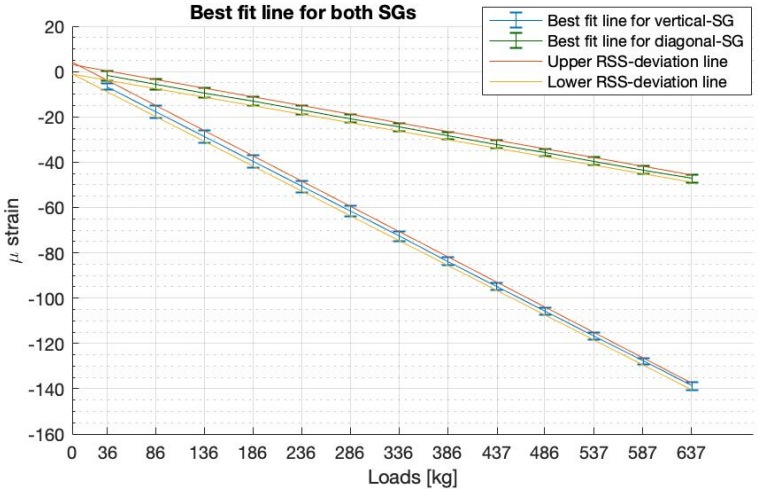

Figure D.1: Output from vertical-SGs and diagonal-SGs applied axial load.

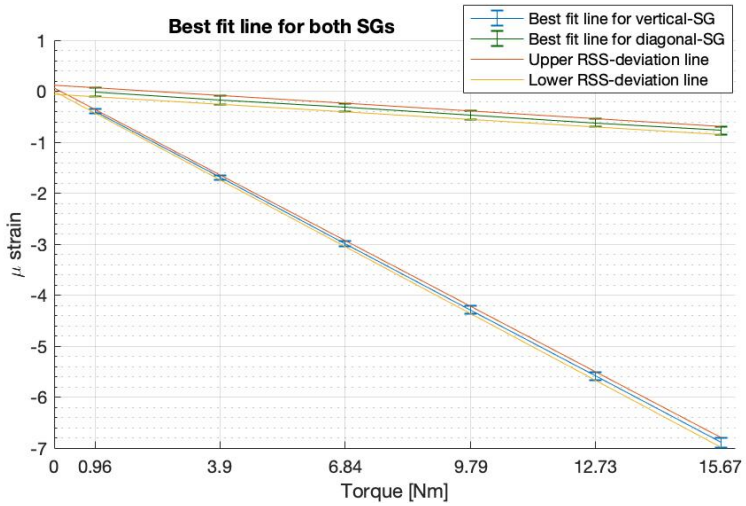

Figure D.2: Output from vertical-SGs and diagonal-SGs applied torque load.

The Upper Deviation Line

The best fit line to the upper RSS-deviation for the output of the vertical-SGs with axial load applied, the red line above the blue line in Figure D.1, is given by

$$\epsilon_{v,a} = A_{v,a,up} \cdot F_{upper} + B_{v,a,up} \qquad [-] \tag{D.1}$$

The best fit line to the upper RSS-deviation for the output of the vertical-SGs with torque load applied, the red line above the blue line in Figure D.2, is given by

$$\epsilon_{v,t} = A_{v,t,up} \cdot T_{upper} + B_{v,t,up} \qquad [-] \tag{D.2}$$

Equation D.1 and D.2 combined to describe the upper RSS-deviation plane for the vertical-SGs in three dimensions. As this is the *upper* deviation line, the intersection with the strain-axis is chosen to be the maximum point of intersection, and the plane is described by

$$\epsilon_v = A_{v,a,up} \cdot F_{up} + A_{v,t,up} \cdot T_{up} + max(B_{v,a,up}, B_{v,t,up}) \qquad [-] \tag{D.3}$$

where the numerical values of the coefficients are given in Table D.1.

Coefficient	Numerical value
$A_{v,a,up}$	- 0.2223
$B_{v,a,up}$	4.1444
$A_{v,t,up}$	- 0.4374
$B_{v,t,up}$	0.0620

Table D.1: The numerical values of the best fit lines of the upper deviation for the vertical-SGs, the red lines in Figure 5.4 and 5.5.

The best fit line to the upper RSS-deviation for the output of the diagonal-SGs with axial load applied, the red line above the green line in Figure D.1, is given by

$$\epsilon_{d,a} = A_{d,a,up} \cdot F_{up} + B_{d,a,up} \qquad [-] \tag{D.4}$$

The best fit line to the upper RSS-deviation for the output of the diagonal-SGs with torque load applied, the red line above the green line in Figure D.2, is given by

$$\epsilon_{d,t} = A_{d,t,up} \cdot T_{up} + B_{d,t,up} \qquad [-] \tag{D.5}$$

Equation D.4 and D.5 combined to describe the upper RSS-deviation plane for the diagonal-SGs in three dimensions and is given by

$$\epsilon_d = A_{d,a,up} \cdot F_{up} + A_{d,t,up} \cdot T_{up} + max(B_{d,a,up}, B_{d,t,up}) \qquad [-] \tag{D.6}$$

Also here, the planes intersection with the strain axis is chosen to be the maximum of the two line's intersection. The numerical values of the coefficients are given in Table D.2.

Coefficient	Numerical value
$A_{d,a,up}$	- 0.0764
$B_{d,a,up}$	3.0453
$A_{d,t,up}$	- 0.0516
$B_{d,t,up}$	0.1177

Table D.2: The numerical values of the best fit lines of the upper deviation for the diagonal-SG, the red lines in Figure 5.4 and 5.5.

When solving equation D.3 and D.6 for *F* and *T*, we get upper deviation of the force expressed as

$$F_{up} = \frac{A_{d,t,up} \cdot \epsilon_v - A_{v,t,up} \cdot \epsilon_d + A_{v,t,up} \cdot max(B_{d,a,up}, B_{d,t,up}) - A_{d,t,up} \cdot max(B_{v,a,up}, B_{v,t,up})}{A_{v,a,up} \cdot A_{d,t,up} - A_{v,t,up} \cdot A_{d,a,up}} \quad [kg] \tag{D.7}$$

When introducing new coefficients the equation may be simplified to

$$F_{up} = C_{f,1,up} \cdot \epsilon_v + C_{f,2,up} \cdot \epsilon_d + C_{f,3,up} \qquad [kg] \tag{D.8}$$

where the coefficients *C* are expressed in terms of the known coefficients *A* and *B*, and their numerical values are given in Table D.3.

Coefficient	**In terms of $A_{i,j,up}$ and $B_{i,j,up}$**	**Numerical value** [-]
$C_{f,1,up}$	$\frac{A_{d,t,up}}{A_{v,a,up} \cdot A_{d,t,up} - A_{v,t,up} \cdot A_{d,a,up}}$	2.3512
$C_{f,2,up}$	$\frac{-A_{v,t,up}}{A_{v,a,up} \cdot A_{d,t,up} - A_{v,t,up} \cdot A_{d,a,up}}$	-19.9301
$C_{f,3,up}$	$\frac{A_{v,t,up} \cdot max(B_{d,a,up}, B_{d,t,up}) - A_{d,t,up} \cdot max(B_{v,a,up}, B_{v,t,up})}{A_{v,a,up} \cdot A_{d,t,up} - A_{v,t,up} \cdot A_{d,a,up}}$	50.9491

Table D.3: The numerical values of the coefficients in equation D.8 describing the upper limit of axial load applied.

Torque is given by

$$T_{up} = \frac{-A_{d,a,up} \cdot \epsilon_v + A_{v,a,up} \cdot \epsilon_d - A_{v,a,up} \cdot max(B_{d,a,up}, B_{d,t,up}) + A_{d,a,up} \cdot max(B_{v,a,up}, B_{v,t,up})}{A_{v,a,up} \cdot A_{d,t,up} - A_{v,t,up} \cdot A_{d,a,up}} \quad [\mathrm{N} \cdot \mathrm{m}] \tag{D.9}$$

and the simplified version of that equation is

$$T_{up} = C_{t,1,up} \cdot \epsilon_v + C_{t,2,up} \cdot \epsilon_d + C_{t,3,up} \qquad [\mathrm{N} \cdot \mathrm{m}] \tag{D.10}$$

where the coefficients *C* are expressed in terms of the known coefficients *A* and *B*, and their numerical values are given in Table D.4.

Coefficient	In terms of $A_{i,j,up}$ and $B_{i,j,up}$	Numerical value [-]
$C_{t,1,up}$	$\frac{-A_{d,a,up}}{A_{v,a,up} \cdot A_{d,t,up} - A_{v,t,up} \cdot A_{d,a,up}}$	-3.4812
$C_{t,2,up}$	$\frac{A_{v,a,up}}{A_{v,a,up} \cdot A_{d,t,up} - A_{v,t,up} \cdot A_{d,a,up}}$	10.1291
$C_{t,3,up}$	$\frac{-A_{v,a,up} \cdot max(B_{d,a,up}, B_{d,t,up}) + A_{d,a,up} \cdot max(B_{v,a,up}, B_{v,t,up})}{A_{v,a,up} \cdot A_{d,t,up} - A_{v,t,up} \cdot A_{d,a,up}}$	-16.4188

Table D.4: The numerical values of the coefficients in the equation D.10 describing the upper limit of torque load applied.

The Lower Deviation Line

Then the complete procedure is almost identical for the lower RSS-deviation, where the difference is that the point of intersection with the strain axis is chosen to be the minimum value. The best fit line to the lower RSS-deviation for the output of the vertical-SGs with axial load applied, the yellow line below the blue line in Figure D.1, is given by

$$\epsilon_{v,a} = A_{v,a,low} \cdot F_{lower} + B_{v,a,low} \qquad [-] \tag{D.11}$$

The best fit line to the lower RSS-deviation for the output of the vertical-SGs with torque load applied, the yellow line below the blue line in Figure D.2, is given by

$$\epsilon_{v,t} = A_{v,t,low} \cdot T_{lower} + B_{v,t,low} \qquad [-] \tag{D.12}$$

Equation D.11 and D.12 combined to describe the lower RSS-deviation plane for the vertical-SGs in three dimensions and is given by

$$\epsilon_{v} = A_{v,a,low} \cdot F_{low} + A_{v,t,low} \cdot T_{lower} + min(B_{v,a,low}, B_{v,t,low}) \qquad [-] \tag{D.13}$$

Here, the lowest value is chosen as the point of intersection as the plane will be used to describe the *lower* deviation. The numerical values of the coefficients are found in Table D.5.

Coefficient	Numerical value
$A_{v,a,low}$	- 0.2188
$B_{v,a,low}$	-1.0587
$A_{v,t,low}$	- 0.4455
$B_{v,t,low}$	-0.0021

Table D.5: The numerical values of the best fit lines of the lower deviation for the vertical-SGs, the yellow lines in Figure 5.4 and 5.5.

The best fit line to the lower RSS-deviation for the output of the diagonal-SGs with axial load applied, the yellow line below the green line in Figure D.1, is given by

$$\epsilon_{d,a} = A_{d,a,low} \cdot F_{low} + B_{d,a,low} \qquad [-] \tag{D.14}$$

The best fit line to the lower RSS-deviation for the output of the diagonal-SGs with torque load applied, the yellow line below the green line in Figure D.2, is given by

$$\epsilon_{d,t} = A_{d,t,low} \cdot T_{low} + B_{d,t,low} \qquad [-] \tag{D.15}$$

Equation D.14 and D.15 are combined to describe the lower RSS-deviation plane for the diagonal-SGs in three dimensions and is given by

$$\epsilon_d = A_{d,a,low} \cdot F_{low} + A_{d,t,low} \cdot T_{low} + min(B_{d,a,low}, B_{d,t,low}) \qquad [-] \tag{D.16}$$

Coefficient	Numerical value
$A_{d,a,low}$	-0.0749
$B_{d,a,low}$	-1.1347
$A_{d,t,low}$	-0.0505
$B_{d,t,low}$	-0.0599

Table D.6: The numerical values of the best fit lines of the lower deviation for the diagonal-SGs, the yellow lines in Figure 5.4 and 5.5.

When solving equation D.13 and D.16 for *F* and *T*, we get

$$F_{low} = \frac{A_{d,t,low} \cdot \epsilon_v - A_{v,t,low} \cdot \epsilon_d + A_{v,t,low} \cdot min(B_{d,a,low}, B_{d,t,low}) - A_{d,t,low} \cdot min(B_{v,a,low}, B_{v,t,low})}{A_{v,a,low} \cdot A_{d,t,low} - A_{v,t,low} \cdot A_{d,a,low}} \qquad [kg] \tag{D.17}$$

When introducing new coefficients equation D.17 may be simplified

$$F_{low} = C_{f,1,low} \cdot \epsilon_v + C_{f,2,low} \cdot \epsilon_d + C_{f,3,low} \qquad [kg] \tag{D.18}$$

where the coefficients *C* are expressed in terms of the known coefficients *A* and *B*, and their numerical values are given in Table D.7.

Coefficient	**In terms of $A_{i,j,low}$ and $B_{i,j,low}$**	**Numerical value** [-]
$C_{f,1,low}$	$\frac{A_{d,t,low}}{A_{v,a,low} \cdot A_{d,t,low} - A_{v,t,low} \cdot A_{d,a,low}}$	2.2627
$C_{f,2,low}$	$\frac{-A_{v,t,low}}{A_{v,a,low} \cdot A_{d,t,low} - A_{v,t,low} \cdot A_{d,a,low}}$	-19.9610
$C_{f,3,low}$	$\frac{A_{v,t,low} \cdot min(B_{d,a,low}, B_{d,t,low}) - A_{d,t,low} \cdot min(B_{v,a,low}, B_{v,t,low})}{A_{v,a,low} \cdot A_{d,t,low} - A_{v,t,low} \cdot A_{d,a,low}}$	-20.2542

Table D.7: The numerical values of the coefficients in equation D.18 describing the lower deviation of axial load applied.

Torque is given by

$$T_{low} = \frac{-A_{d,a,low} \cdot \epsilon_v + A_{v,a,low} \cdot \epsilon_d - A_{v,a,low} \cdot min(B_{d,a,low}, B_{d,t,low}) + A_{d,a,low} \cdot min(B_{v,a,low}, B_{v,t,low})}{A_{v,a,low} \cdot A_{d,t,low} - A_{v,t,low} \cdot A_{d,a,low}} \quad [\mathrm{N \cdot m}] \tag{D.19}$$

and the simplified version of equation D.19 is

$$T_{low} = C_{t,1,low} \cdot \epsilon_v + C_{t,2,low} \cdot \epsilon_d + C_{t,3,low} \qquad [\mathrm{N \cdot m}] \tag{D.20}$$

where the coefficients *C* are expressed in terms of the known coefficients *A* and *B*, and their numerical values are given in Table D.8.

Coefficient	**In terms of $A_{i,j,low}$ and $B_{i,j,low}$**	**Numerical value** [-]
$C_{t,1,low}$	$\frac{-A_{d,a,low}}{A_{v,a,low} \cdot A_{d,t,low} - A_{v,t,low} \cdot A_{d,a,low}}$	-3.3560
$C_{t,2,low}$	$\frac{A_{v,a,low}}{A_{v,a,low} \cdot A_{d,t,low} - A_{v,t,low} \cdot A_{d,a,low}}$	9.8035
$C_{t,3,low}$	$\frac{-A_{v,a,low} \cdot min(B_{d,a,low}, B_{d,t,low}) + A_{d,a,low} \cdot min(B_{v,a,low}, B_{v,t,low})}{A_{v,a,low} \cdot A_{d,t,low} - A_{v,t,low} \cdot A_{d,a,low}}$	7.5711

Table D.8: The numerical values of the coefficients in equation D.18 describing the lower deviation of torque applied.

E Recommendations to the Turbine Testing Lab at Kathmandu University

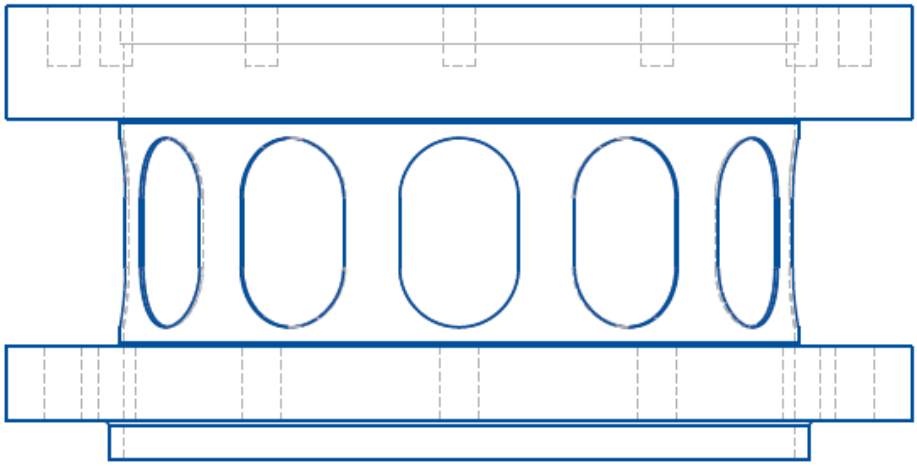

Axial Load and Friction Torque Measuring Device Developed for the Turbine Testing Lab at Kathmandu University

Andrea Engøy

December
2019

Table of Contents

List of Tables

List of Figures

Abbreviations

ATMD	Axial load and friction Torque Measuring Device
BEP	Best Efficiency Point
DAQ	Data Acquisition
GF	Gage Factor
KU	Kathmandu University
LIFO	Last In First Out
NI	National Instruments
NTNU	Norwegian University of Science and Technology
RSS	Root of the Sum of the Squares
SG	Strain Gauges
TTL	Turbine Testing Lab

List of Symbols

Symbol	Description	Unit
A	Cross section Area	m^2
b’	Repeatability	-
E	Elasticity Module	N/m^2
ϵ	Strain	-
F	Force	N
f_0	Zero Deviation	-
g	Gravitational constant	m/s^2
h_{mean}	Hysteresis	-
L	Length	m
N	Normal force	N
n_{S_x}	Size of sample	-
n_x	Number of measurement series pair	-
ν	Poisson Ration	-
R	Resistance	Ω
S_x	Standard deviation	-
σ	Stress	Pa
t	Student-t distribution number	-
$\vec{T_z}$	Torque	Nm
U	Voltage	V
w	Uncertainty	-
x_{ij}	Data from measurement series i in measurement point j	-

Chapter 1

Introduction

This document is a complete guide to the measurement system for axial load and friction torque measurements, from now on called *ATMD*, to be installed at the Turbine Testing Laboratory (TTL) at Kathmandu University (KU) and is developed by Engøy [1] during her Master's Thesis at NTNU. The following contains of a description of the final design, the theoretical foundation, and instruction in how to perform the calibration. The ATMD uses strain gauges to measure the strain applied to the device. Then, calibration lines obtained in the calibration process are functions of the measured strain, and are used to calculate the applied axial forces and friction torque. When the ATMD is ready to be installed it will replace the *Axial Thrust Block Spare Section*, colored yellow in Figure 1.1. The figure shows the assembly of the turbine and the parts are listed in Table 1.1.

The ATMD is resting on part 20, the *Head Cover Top*, and all the axial forces working on the runner and shaft is aggregated to the ATMD from above leaving the ATMD to be compressed. The sources for the axial loads are the weight of the runner, shaft and other parts, and hydraulic forces of about 7000N. The ball bearing, detail B, shown in Figure 1.2a, and the cylindrical bearing, part 10, detail C, shown in Figure 1.2b are the sources of the friction torque the ATMD are to measure. Because the friction loss in such bearings is very low, the maximum friction torque to measure is around 20 Nm [2].

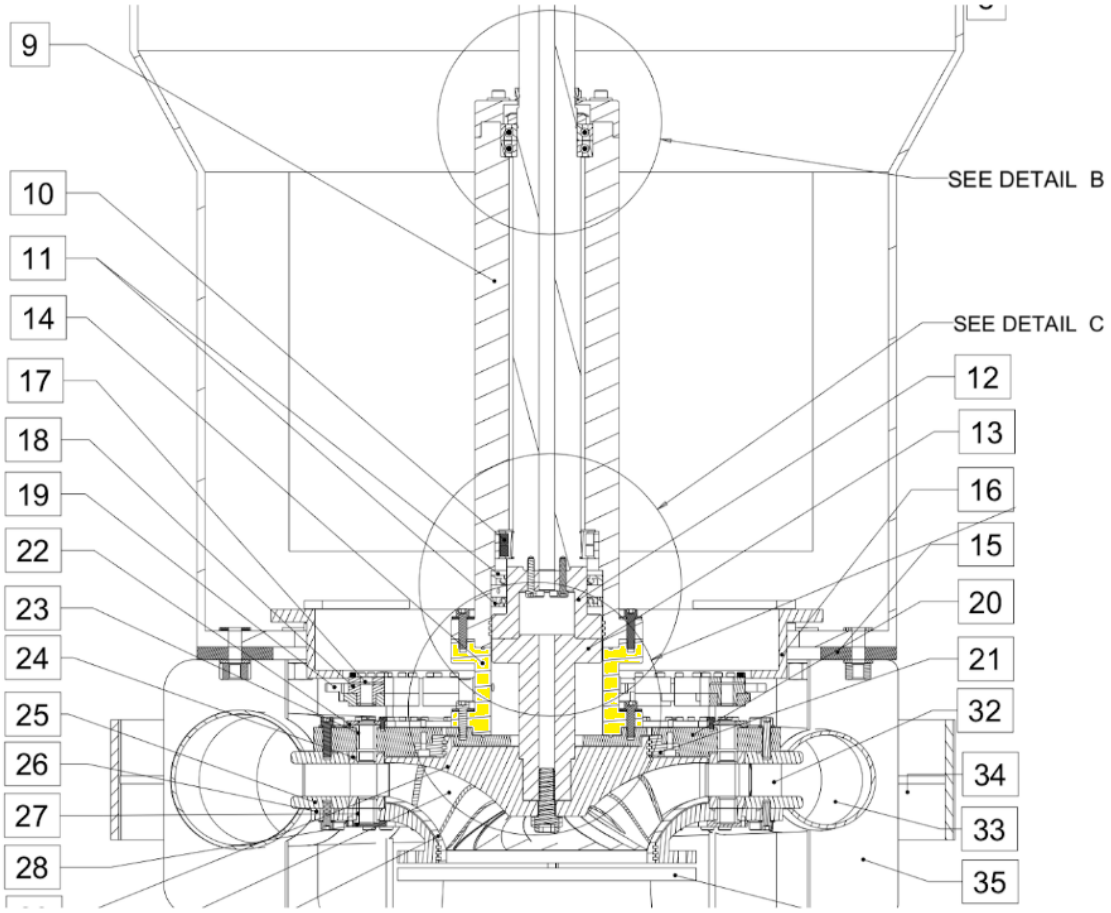

Figure 1.1: The assembly of the turbine and related parts, where the ATMD will replace the yellow colored part.

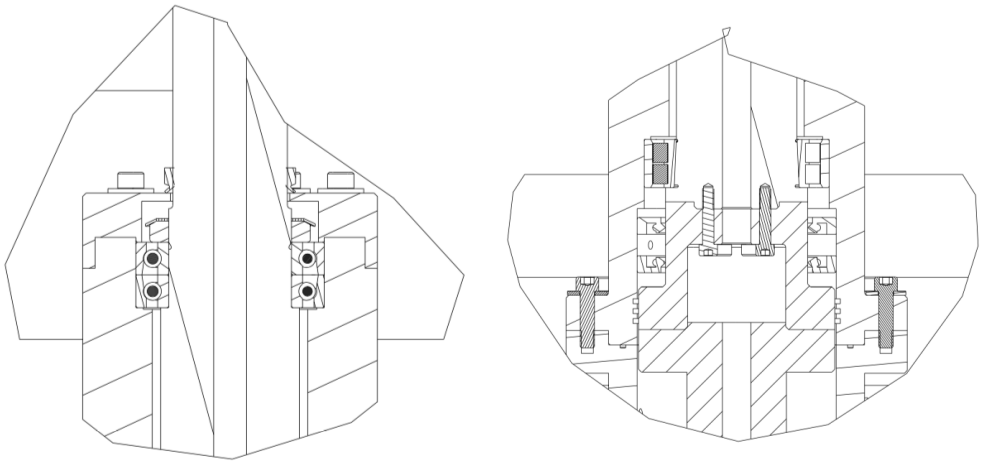

(a) Detail B: Ball bearings.

(b) Detail C: Cylindrical Bearings.

Figure 1.2: The bearings causing the friction torque.

Part number	Part name
9	Bearing housing
10	Cylindrical roller bearing
11	Shaft seal
12	Turbine intermediate shaft
13	Turbine shaft to runner
14	**Axial block spare section (ATMD)**
15	Turbine support spiral casing top plate
16	Guide vane control ring
17	Guide vane
18	ETP bushing
19	Guide vane control ring link
20	Head cover top
21	Head cover top labyrinth seal
22	Guide vane cover top
23	Guide vane top flange bushing
24	Guide ring
25	Stay ring
26	Stay vane support
27	Guide vane bottom flange bushing
28	Guide vane cover bottom
29	Runner Hub
30	Runner blade
31	Runner shroud
32	Stay vane
33	Spiral casing
34	Spiral casing radial supports
35	Spiral casing plate support

Table 1.1: List of the parts in Figure 1.1.

1.1 Design of the Measuring Device

The main challenge in the design of the ATMD is that the strains caused by the friction torque is much smaller than strains caused by the axial forces. The key is to find the balance between making the ATMD strong enough to be safe for all operation points and ”weak” enough to be able to measure small values with low uncertainties. The final design of the ATMD is shown in Figure 1.3, note that the wall thickness is 1 mm, and it is planned to be made of 316 stainless steel. The choice for this design is based on numerical results obtained using Ansys Mechanical.

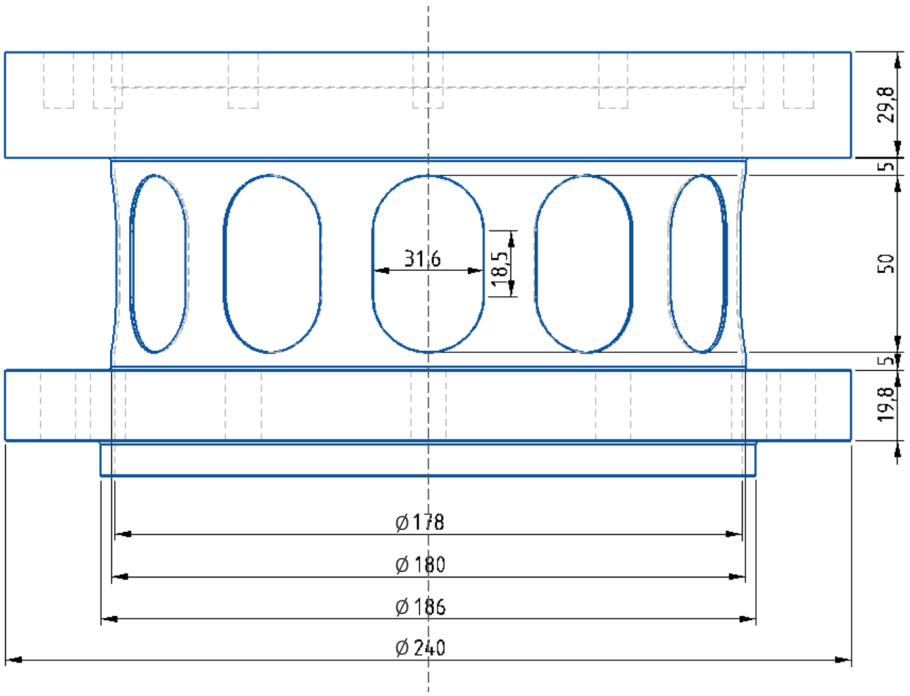

Figure 1.3: Final design of the ATMD with dimensions in mm.

When the ATMD is applied both 7000 N and 20 Nm the strain distribution is as in Figure 1.4 and the direction of the strain is shown as a vector plot in Figure 1.5. The yellow squares in the figure are where the axial load measuring strain gauges will be attached. The strain distribution for only 20 Nm applied torque is shown in Figure 1.6 and the vector plot of the direction of strain is shown in Figure 1.7. In this figure the yellow squares are where the torque load measuring strain gauges will be attached. The strains in the ATMD when only applied torque, around 20 μstrain, is big enough to be measured by the strain gauges, and the vector plots show that the strain is working in the same directions as in theory, see section 2.2. The maximum possible forces applied to the ATMD is 20 Nm and 8500 N in total axial force, where 7000 N is due to hydraulics and 1500 N is an estimation of the weight of the turbine runner, bearing housing and other parts. The stress calculated for the maximum amount of forces is 74 MPa which is 36 % of the yield strength for a stainless steel type with 205 MPa as yield limit [3].

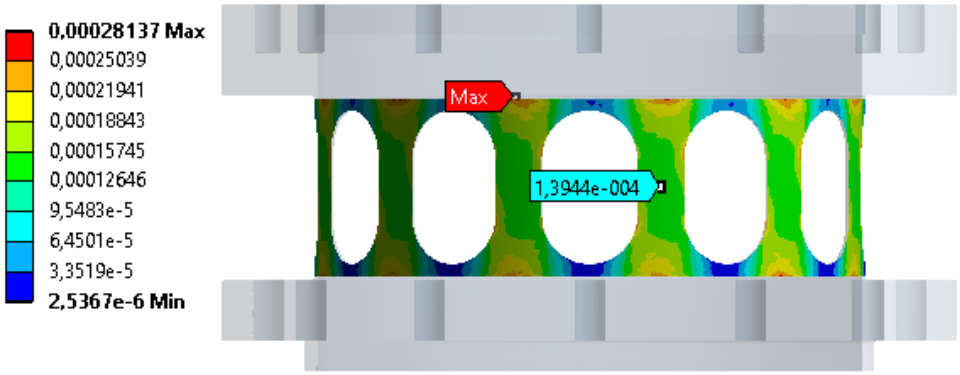

Figure 1.4: The distribution of strain when applied 7000 N and 20 Nm torque.

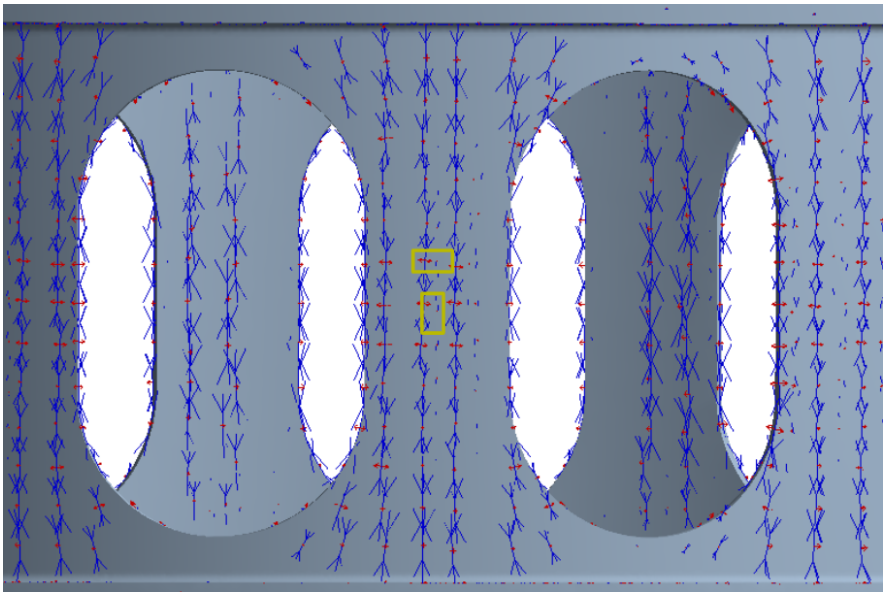

Figure 1.5: Vector plot of the strains when applied 7000 N and 20 Nm torque with the placement of axial load-measuring strain gauges shown with yellow squares.

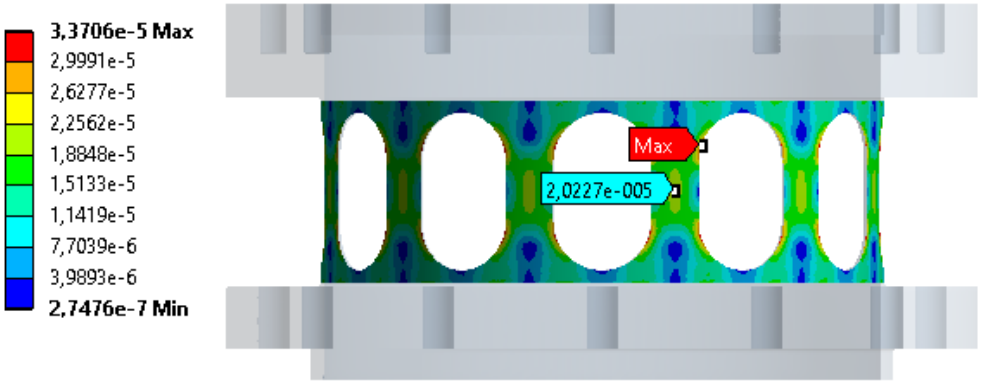

Figure 1.6: The distribution of strain when applied 20 Nm torque.

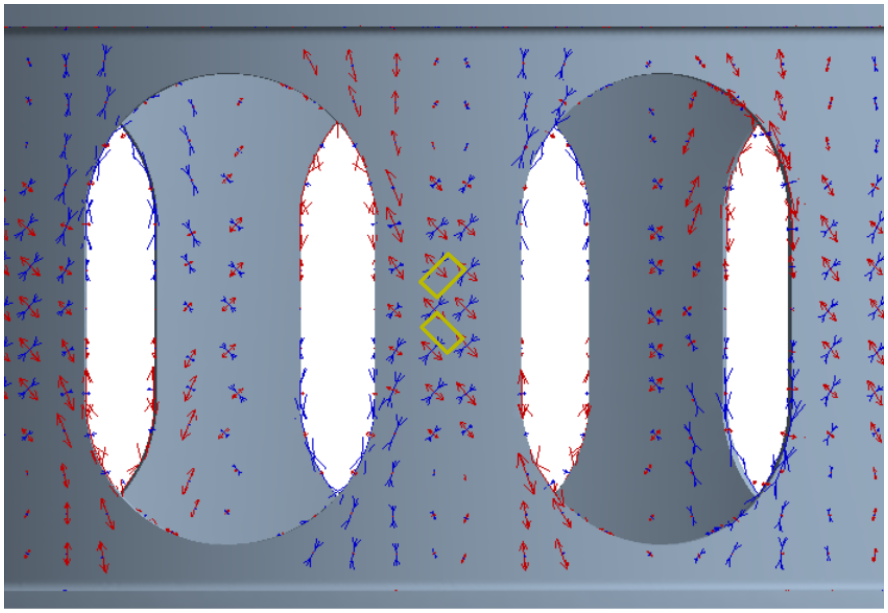

Figure 1.7: Vector plot of the strains when applied 20 Nm torque with the placement of torque-measuring strain gauges shown with yellow squares.

Chapter 2

Theoretical Foundation

This chapter describes the theory used in the experimental work and is mostly copied from Engøy's master thesis [1].

2.1 Stress and Strain in a Solid Body

As a result of forces working on a solid body, stress and strain occurs in the material. The three following equations are from [4]. Normal strain ϵ is defined as the relative change in length in the axial direction, given by

$$\epsilon = \frac{\Delta L}{L_0} \qquad [-] \tag{2.1}$$

The normal stress in a solid body σ is defined as the normal force N divided by the body's cross section area A, given by

$$\sigma = \frac{N}{A} \qquad [\mathrm{Pa}] \tag{2.2}$$

For linear elastic materials, like steel, Hooke's law describes the linear relationship between the stress and strain, and is given by

$$\epsilon = \frac{\sigma}{E} = \frac{N}{A \cdot E} \qquad [-] \tag{2.3}$$

where E is Young's Modulus for the material. A material being linear elastic means that any compression or elongation giving stress values σ below the yield strength, is reversible. If there is applied stress values above this limit, the object behaves like a spring that have been pulled too far and lost its "bounce".

2.2 Strain Gauges

Strain gauges mounted on the surface of a solid body that is compressed or stretched can measure the strain through the change in length of the wires causing changes in the resistance [5]. Strain gauges are often arranged in a Whetstone bridge as this configuration is well suited for measuring changes in resistance [6]. Figure 2.1 shows the schematic of a full Wheatstone bridge.

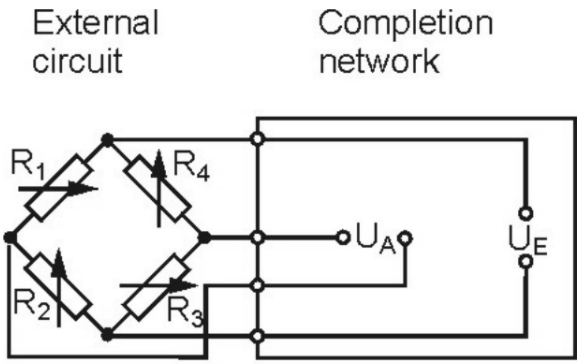

Figure 2.1: Strain gauges arranged in a full Wheatstone bridge [6].

The following equations are from the article *Applying the Wheatstone Bridge circuit* by Karl Hoffman [6]. When the strain gauges are arranged as in Figure 2.1 a linear relationship between the relative change in resistance and strain is obtained, given by

$$\frac{\Delta R}{R_0} = GF \cdot \epsilon \qquad [-] \tag{2.4}$$

where GF is the Gage Factor, a characteristic depending on the specific strain gauge.

The equation

$$\frac{U_A}{U_E} = \frac{R_1}{R_1 + R_2} - \frac{R_4}{R_3 + R_4} = \frac{R1 \cdot R_3 - R_2 \cdot R_4}{(R_1 + R_2) \cdot (R_3 + R_4)} \qquad [-] \tag{2.5}$$

is valid for a bridge that is initially balanced, which means

$$\frac{U_A}{U_E} = 0 \qquad [-] \tag{2.6}$$

when

$$R_1 = R_2 = R_3 = R_4 \qquad [\Omega]$$

or

$$\frac{R_1}{R_2} = \frac{R_4}{R_3} \qquad [-]$$

When R_1 to R_4 are exposed to strain, the bridge is no longer balanced and U_A is non-zero. With the assumption that the deviation in resistance, ΔR_i, is much smaller than the resistance itself, R_i, second-order factors can be neglected and equation 2.5 can be written as

$$\frac{U_A}{U_E} = \frac{1}{4} \cdot (\frac{\Delta R_1}{R_1} - \frac{\Delta R_2}{R_2} + \frac{\Delta R_3}{R_3} - \frac{\Delta R_4}{R_4}) \qquad [-] \tag{2.7}$$

By substituting equation 2.4 in equation 2.7, we get the relation between the change in voltage and applied strain

$$\frac{U_A}{U_E} = \frac{GF}{4} \cdot (\epsilon_1 - \epsilon_2 + \epsilon_3 - \epsilon_4) \qquad [-] \tag{2.8}$$

There are several different ways of arranging the strain gauges depending on the desired measurand. For measuring axial strain the arrangement is as in Figure 2.2. With this arrangement the strain gauges only give output due to axial load, any torque load or extension of the wires due to a temperature rise will be canceled out [7]. Note that the figure is demonstrating tension while the ATMD will be applied compression. The direction of the axial force *F* only affects the sign of the strain output, and the principle is the same for positive and negative axial forces. For measuring compression ϵ_1 and ϵ_3 will be negative and ϵ_2 and ϵ_4 will be positive, and equation 2.8 becomes

$$\frac{U_A}{U_{E\,Compression}} = \frac{GF}{4} \cdot (-|\epsilon_1| - |\epsilon_2| - |\epsilon_3| - |\epsilon_4|) \qquad [-] \tag{2.9}$$

In most cases ϵ_1 and ϵ_3 are the values of interest as strain gauge number 1 and 3 are the ones placed in the same direction as the applied forces. Poisson's Ratio, ν, is a material constant describing the material's change in length perpendicular to the force direction, and is usually around 0.3 for metals. For a purely axial compression, we have $\epsilon_1 = \epsilon_3 = \epsilon$ and $\epsilon_2 = \epsilon_4 = \nu \cdot \epsilon$, by using this we can rewrite equation 2.9 to

$$\frac{U_A}{U_{E\,Compression}} = \frac{GF}{4} \cdot (-|\epsilon| - |\nu \cdot \epsilon| - |\epsilon| - |\nu \cdot \epsilon|)$$

$$\frac{U_A}{U_{E\,Compression}} = -\frac{GF \cdot |\epsilon|}{4} \cdot (2 + 2 \cdot \nu) \qquad [-] \tag{2.10}$$

For measuring torque the strain gauges are arranged as in Figure 2.3. With this arrangement the strain gauges only give output caused by torque, any axial load or extension due to temperature rise, will be canceled out [7]. In the figure a clockwise torque is applied, meaning the left side of the beam is held fixed and a clockwise twist is applied on the right side of the beam. This causes strain gauge 1 and 3 to experience positive strain and strain gauge 2 and 4 to experience negative strain. In most practical cases for torque measurement, pre-positioned strain gauges, arranged as a fishtail, are used to make sure the strain gauges are exactly 45°. The absolute value of $|\epsilon_1| = |\epsilon_2| = |\epsilon_3| = |\epsilon_4| = \epsilon$ making equation 2.8 to reduce to

$$\frac{U_A}{U_{E\,Torque}} = \frac{GF}{4} \cdot (|\epsilon| - (-|\epsilon|) + |\epsilon| - (-|\epsilon|))$$

$$\frac{U_A}{U_{E\,Torque}} = GF \cdot \epsilon \qquad [-] \tag{2.11}$$

Since the equations for change in voltage for axial and torque load applied, respectively equations 2.10 and 2.11, only consist of one unknown value ϵ, this value is possible to derive. The change in voltage in the bridge U_A is measureable, and the the exitation voltage U_E, the gage factor GF and, for the compression case, the Poisson's Ratio ν are known.

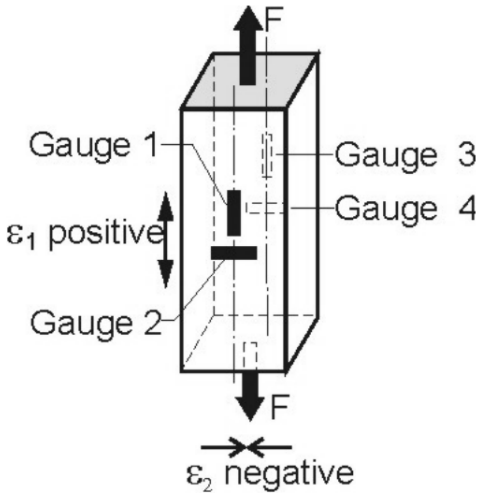

Figure 2.2: Arrangement of strain gauges for measuring axial forces [6].

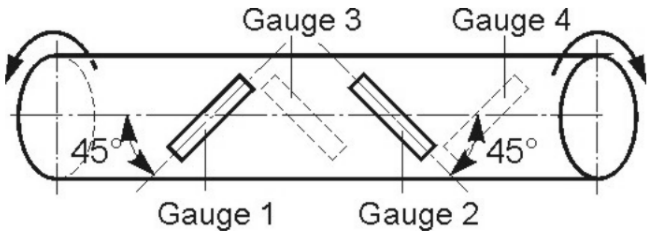

Figure 2.3: Arrangement of strain gauges for measuring torque [6].

2.3 Uncertainty

Uncertainties are divided into two parts: systematic and random. The systematic error is caused by the experimental setup and the measuring devices used, are never exactly accurate. The following equations, describing systematic errors, are published by German Calibration Service (DKD) in *Calibration of Pressure Gauges* [8]. The first number in the subscripts in the equations is referring to a total of six measurement series. Each measurement session is done in pairs, first on-loading (number 1, 3 and 5) and then off-loading (number 2, 4 and 6), where measurement series 1 and 2 are one pair of on-loading and off-loading. The second subscript refers to a measurement point within a measurement series. In the equations where the second subscript is *j*, then the uncertainty is different for each measurement point. The unit in the three following equations is not specified since it depends on the unit of the measurements, which is μstrain for measurements performed by the ATMD.

If the measurement of a variable has different output when the variable is increasing and decreasing, hysteresis is occurring, see Figure 2.4 [5], and is given by

$$h_{mean,j} = \frac{1}{n_x} \cdot \big(|(x_{2,j} - x_{1,0}) - (x_{1,j} - x_{1,0})| + |(x_{4,j} - x_{3,0}) - (x_{3,j} - x_{3,0})| + |(x_{6,j} - x_{5,0}) - (x_{5,j} - x_{5,0})| \big) \tag{2.12}$$

where n_x is the number of measurement pairs, which is three for a set of six measuring series.

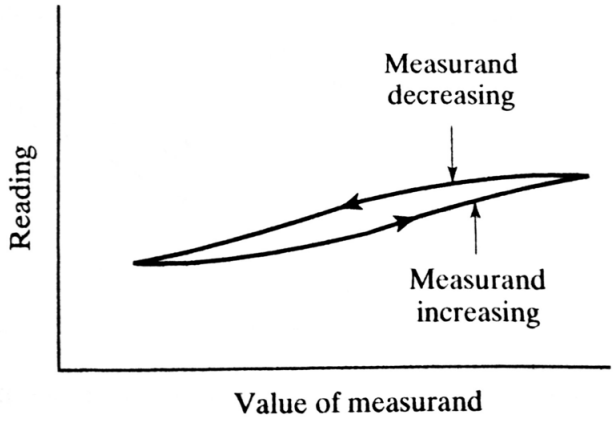

Figure 2.4: The principle of hysteresis [5].

Another systematic error is the deviation in output at zero loads for the different measurement series, called zero deviation. It is calculated by taking the maximum deviation of the measured value at zero load for one on-loading and the corresponding off-loading, and is calculated by

$$f_0 = max\big(|x_{2,0} - x_{1,0}|, |x_{4,0} - x_{3,0}|, |x_{6,0} - x_{5,0}|\big) \tag{2.13}$$

Repeatability is the error that describes how much the results at one point deviates within the different measurement series. The repeatability for each measurement point *j* is given by

$$\begin{aligned} b'_{up,j} =& max\big(|(x_{1,j} - x_{1,0}) - (x_{5,j} - x_{5,0})|, && (2.14)\\ & |(x_{1,j} - x_{1,0}) - (x_{3,j} - x_{3,0})|, && (2.15)\\ & |(x_{3,j} - x_{3,0}) - (x_{5,j} - x_{5,0})|\big) \\ b'_{down,j} =& max\big(|(x_{2,j} - x_{2,0}) - (x_{4,j} - x_{4,0})|, && (2.16)\\ & |(x_{2,j} - x_{2,0}) - (x_{6,j} - x_{6,0})|, && (2.17)\\ & |(x_{4,j} - x_{4,0}) - (x_{6,j} - x_{6,0})|\big) \\ b'_{mean,j} =& max(b'_{up,j}, b'_{down,j}) && (2.18) \end{aligned}$$

Random errors will occur when gathering data in big samples. By assuming the data points of a measurement have a Gaussian distribution, the random uncertainty can be calculated by

$$w_{\bar{x}} = t \cdot \frac{S_x}{\sqrt{n_{S_x}}} \tag{2.19}$$

where S_x is the standard deviation of the sample and n_{S_x} is the size of the sample. The number *t* is the Student's t-distribution number which is obtained from tables and is a function of the degree of freedom and the desired confidence interval.

When dealing with a variable that depends on several uncertain values it is not very likely that all terms become simultaneously high or low, and summing up all the uncertainties give unreasonably high estimates. Calculating the *Root of the Sum of the Squares* (RSS) is a more used method for the total uncertainty [5], and is given by

$$w_R = \left(\sum_{i=1}^{n} \left[w_{x_i} \cdot \frac{\delta R}{\delta x_i}\right]^2\right)^{\frac{1}{2}} \tag{2.20}$$

where w_R is the total uncertainty for the result variable *R* and w_{x_i} is the uncertainty of variable x_i. The last term, $\frac{\delta R}{\delta x_i}$, is the relation between a small change in the result variable *R* and a small change in variable x_i, and is equal to one if a change in x_i have a direct impact on the result variable *R*.

Chapter 3

Preparations for Calibration

3.1 The Experimental Set Up

The experimental set up for axial load measurements is arranged such that the ATMD is compressed, see Figure 3.1 for a schematic. Make sure the ATMD is placed on a stable and still place where it is not exposed to any vibration. On top of the ATMD, place a circular cover in which the hanging system can be attached in the exact center. This is important because if the weights applied are applied slightly off-center the forces will not be evenly distributed in the walls of the ATMD and the strain gauges will give wrong output.

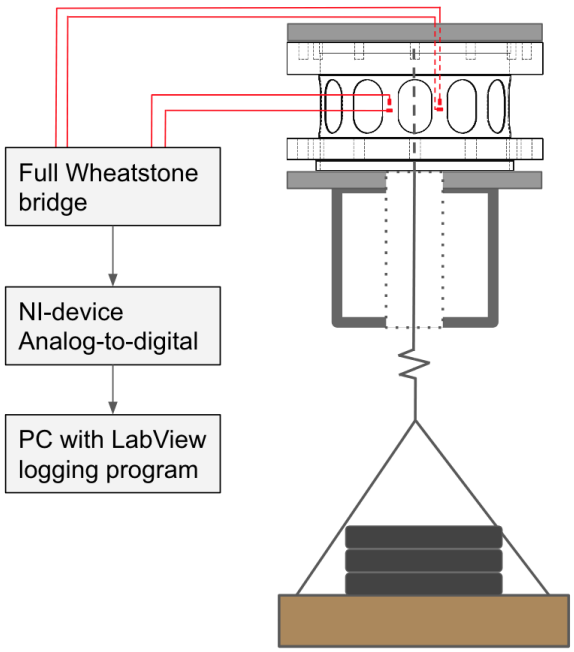

Figure 3.1: Drawing of the experimental set up for axial load measurement.

The equipment used in the axial load data collection:

- The ATMD with the design as in Figure 1.3
- Strain gauges attached to the ATMD cabled in a full Wheatstone bridge
- A temperature probe taped to the surface of the ATMD
- Some isolating material to cover the strain gauges and temperature probe
- A strong beam with a hole between the top and bottom
- Hanging system
  - Top cover plate with screws
  - A hook
  - Straps
  - Lever hoist
  - Pallet
- 700 kg in weight plates (each plate of maximum 50 kg)
- NI-devices converting analog signals from the strain gauges to digital signals
  - NI-module meant for temperature measurements, e.g. NI 9217
  - NI-module meant for strain gauge measurements, e.g. NI 9237
  - Two terminal boxes (if necessary, depending on the NI-module), e.g. NI 9949
  - NI-chassis with power cord, e.g. NI cDAQ-9178
  - USB-cable to connect the chassis with the PC
- PC with LabView program for logging
- Matlab for post-analysis
- Safety shoes

For the torque load measurements hang the ATMD in a stable frame and attach an arm of 15 cm underneath, see Figure 3.2 for schematic. Also for this setup, the ATMD must be hanged from a stable place without any vibrations. The hanging system may consist of a thin wire and a metal plate where the weights are laid.

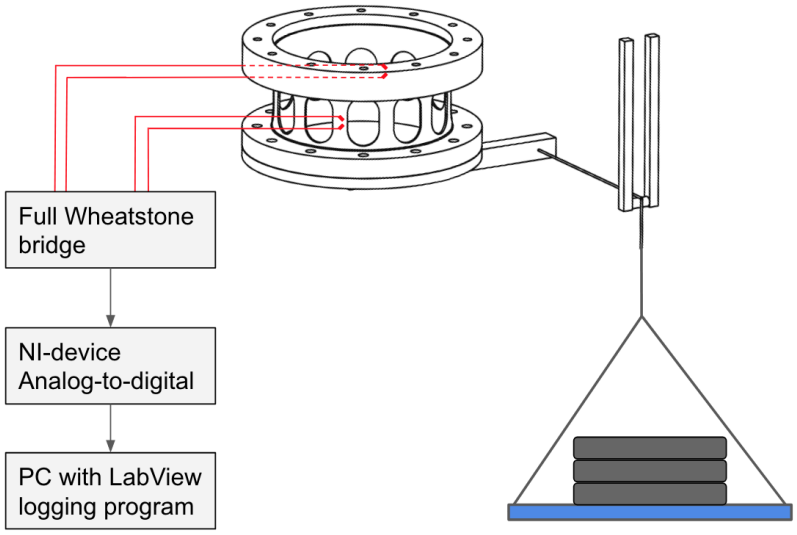

Figure 3.2: Drawing of the experimental set-up for torque measurements.

The equipment used in the torque load data collection:

- The ATMD with the design as in Figure 1.3
- Strain gauges attached to the ATMD cabled in a full Wheatstone bridge
- A temperature probe taped to the surface of the ATMD
- Some isolating material to cover the strain gauges and temperature probe
- A strong frame to hang the ATMD from
- Hanging system
  - An arm attached underneath the ATMD (e.g. 15 cm)
  - Plate to place weights
  - Wire(s) to attach to the arm and plate
  - Pulley on which the wire can slide frictionless
- 7 weight plates of 2 kg (or 14 plates of 1 kg)
- NI-devices converting analog signals from the strain gauges to digital signals
  - NI-module meant for temperature measurements, e.g. NI 9217
  - NI-module meant for strain gauge measurements, e.g. NI 9237
  - Two terminal boxes (if necessary, depending on the NI-module), e.g. NI 9949
  - NI-chassis with power cord, e.g. NI cDAQ-9178
  - USB-cable to connect the chassis with the PC
- PC with LabView program for logging
- Matlab for post-analysis
- Safety shoes

It matters which order the weight plates are applied, and this order must be the same for all measuring series. To achieve this, each weight plate must be labeled. For weight plates of 25 kg, a suggested label is w25-1, w25-2, etc., and for weight plates of 10 kg, a suggested label is w10-1, w10-2, etc. When all the plates have been systematically labeled, they should be weighted by a calibrated scale so that their true weight is known.

3.2 Setup of the Strain Gauges

When the ATMD is produced in the stainless steel, with the wall thickness of 1 mm and cutouts as in Figure 1.3, eight strain gauges should be attached. The version of the ATMD used in Engøy's Master's Thesis is made of structural steel st52 [1], and the strain gauges tested are a pre-wired type from Tokyo Sokki Kenkyujo with type number FLA-1-11-1L. They have a gauge resistance of 119.8 $\pm$ 0.5 Ω and a gauge factor of 2.15 $\pm$ 1 %. The gauge length is 1 mm and the strain difference due to temperature change is $\pm$ 0.85 μstrain / °C. The strain gauges to use on the final ATMD must be a type that is matched spesifically to stainless steel to avoid scewed data due to temperature differences.

Attaching the strain gauges to the ATMD is important to do correctly, and it is recommended to perform the mounting with someone experienced. Start by cleaning the ATMD by removing grease, dirt, etc. and clean the workplace such that the ATMD stays clean. On the position where the strain gauges will be attached, lightly polish the surface with an abrasive paper of #120-180 and wipe with acetone, use clean cloths and cotton pins, and let the acetone evaporate. Use a piece of installation tape that is meant for strain gauge mounting and tape the strain gauges in the correct position on the ATMD. Keep the uninsulated wires taped to the surface while the rest of the tape with the strain gauge is lifted off from the surface. Then adhesive can be added on the surface where the strain gauge will be placed, and, in assistance by the tape, the strain gauge can be placed back on the surface. Use thumb pressure on the tape so that the adhesive cures. It is important to use fresh adhesive that is meant to be used on the specific strain gauges, matched with stainless steel and a temperature difference of 20 to 40 °C, the strain gauge supplier should recommend a suited adhesive.

The complete procedure of preparing the surface of the ALMD and the technique of using tape to attach the strain gauges is best to learn by guidance from someone experienced or by watching YouTube videos [9]. Four of the strain gauges are arranged as in Figure 2.2 and 1.5 for the axial load measurements and this group is named vertical-SGs. The other four is arranged as in Figure 2.3 and 1.7 for the torque measurements and is named diagonal-SGs. When the eight strain gauges are attached, they are cabled in two full Wheatstone bridges into the National Instrument module, where the NI-module serves as the *Completion network* in Figure 2.1. National Instruments has a guidance *Connecting Strain Gages to a DAQ Device* that describes how to perform the cabling [10].

3.3 Setup of the Software

When the strain gauges are connected and cabled correctly, connect the temperature probe to a NI-module meant for temperature measurements, and connect the chassis to the computer. Then the next step is to set up the software.

Either construct new logger program or download the files from the LabView-folder in the shared google drive folder. Note that the folder exist of two files, and that both is needed. Open the file ”ATMD-strain-recorder.vi” and the program’s block diagram. Doubleclick the DAQ-assistant to set up the input channels. The first input should be the temperature measurement, the vertical-SG is the second and the diagonal-SG is the third. For the vertical-SG use strain configuration ”Full Bridge III” and Poisson ration 0.3, and for the diagonal-SG use ”Full Bridge I”. For both the vertical-SG and diagonal-SG, fill in the gage factor and gage resistance depending on the strain gauges. Choose voltage excitation source to be internal and voltage excitation value may be set to 2.5 V.

In the ”Strain Setup”, perform an offset nulling-calibration as described in the NI-guidance [10]. This calibration removes the null point offset making sure the output is equal to zero for no load applied. At this point, it is also possible to perform a shunt calibration. When the DAQ assistant is set up correctly, run the program to test it.

Chapter 4

The Calibration

4.1 Collection of Calibration Data

The first thing to do in a measurement session is to turn on the power on the chassis and start the LabView program, then let the program run for 10-15 minutes without any recordings and with no load applied to the ATMD. This is important because the output might drift during the start-up process. Use this time to prepare the weight plates, necessary documents and put on safety shoes. Make sure the temperature probe is taped to the surface of the ATMD, and cover both the probe and the strain gauges with some isolating material so that they are less exposed to the changing air temperature.

The script that is performing the calibration curve calculations and uncertainty analysis, described in section 4.2, needs the collected files to be organized and named in a certain way, and it is therefore recommended to do so right away. Each session of associated onloading and offloading of weights should be stored in one folder and may be called ”AxialSeries_1And2” for the first axial load session. Then each filename must be specified to be ”up#.txt” for onloading and ”down#.txt” for the offloading, where Table 4.1 gives the number ”#”. The full file path and filename is specified in the file path-box, e.g. ”(desired file path)\AxialSeries_1And2 \up#.txt”.

When the signals have stabilized after the start-up process, the first recording without any load, not even the hanging system, can be performed, and this file must have the name ”up-1.txt”. When pressing the record button, LabView will write the output from the strain gauges and temperature probe to the specified file for one minute. Next, the hanging system can be applied, change the filename to ”up0.txt”, make sure it hangs still and undisturbed, and press record. For the data collection of axial load, 50 kg is added in 14 steps, where their filenames will be ”up1.txt” to ”up14.txt”, adding up to a total of 700 kg plus the weight of the hanging system. For the offloading, reverse the process. The first offloading measurement should be performed with maximum weight and named ”down14.txt”, note that ”up14.txt” and ”down14.txt” is collecting measurements for the exactly same load. Then remove weights in LIFO-order, last in first out, and name the files ”down14.txt” to ”down1.txt”. As for the onloading, ”down0.txt” should be a measurement of the hanging system, and ”down-1.txt” should be a measurement without any load. The complete procedure with onloading and offloading is performed three times, resulting in six measurement

series.

The data collection of torque load is performed in the same matter as for axial load. The first recording is without any load and has the filename ”up-1.txt”, then the hanging system is applied with filename ”up0.txt”, and then weights of 1 or 2 kg are added in as many steps as needed to achieve a total torque of 20 Nm. With an arm of 15 cm, a total weight of 14 kg (including the hanging system) is giving the correct amount of torque. Table 4.2 is a suggested table to use during onloading and offloading torque load. As for the axial load, repeat the complete procedure with onloading and offloading torque two more times, resulting in a total of six measurement series.

#	Total weight of added plates [kg]	Actual total weight [kg]	Which weight plates are added				
-1	0	0	-				
0	0	[Weight of hanging system]	Hanging system				
1	50	50+weight of hanging sys	w25-1	w25-2	-	-	-
2	100	100+weight of hanging sys	w25-3	w25-4	-	-	-
3	150	150+weight of hanging sys	etc.				
4	200	200+weight of hanging sys					
5	250	250+weight of hanging sys					
6	300	300+weight of hanging sys					
7	350	350+weight of hanging sys	w10-1	w10-2	w10-3	w10-4	w10-5
8	400	400+weight of hanging sys	w10-6	etc.			
9	450	450+weight of hanging sys					
10	500	500+weight of hanging sys					
11	550	550+weight of hanging sys					
12	600	600+weight of hanging sys					
13	650	650+weight of hanging sys					
14	700	700+weight of hanging sys					

Table 4.1: Example of a table for systematically adding of weights for axial load data collection. The ”Actual total weight”-column should contain the accumulated real weight applied, and the ”Which weight plates are added”-column are filled out with the names of the plates to add.

#	Total weight of added plates [kg]	Actual total torque [Nm]	Which weight plates are added
-1	0	0	-
0	0	[Torque due to hanging system]	Hanging system
1	2	2.9 + torque of hanging sys	w2-1
2	4	5.9 + torque of hanging sys	w2-2
3	6	8.8 + torque of hanging sys	w2-3
4	8	11.8 + torque of hanging sys	w2-4
5	10	14.7 + torque of hanging sys	w2-5
6	12	17.7 + torque of hanging sys	w2-6
7	14	20.6 + torque of hanging sys	w2-7

Table 4.2: Example of a table for systematically adding of weights for torque load data collection. The ”Actual total torque”-column should contain the accumulated real torque applied, and the ”Which weight plates are added”-column are filled out with the names of the plates to add.

4.2 Analysis of the Calibration Data

When the necessary data collection have been performed, there is time to analyze the data in order to produce calibration curves. The Matlab-folder in the shared google drive folder contains scripts that are performing all the necessary calculations and plots. The three folders of measurement files for axial load, e.g. named ”AxialSeries_1And2” etc., must be stored in the ”Axial Load”-folder within the downloaded ”Matlab”-folder, and the three folders of measurement files for torque load, e.g. named ”TorqueSeries_1And2” etc., must be copied to the ”Torque Load”-folder.

There are two Matlab-scripts: ”MainLoadMeasurementsAxialLoad.m” and ”MainLoadMeasurementsTorqueLoad.m”. At the beginning of each script, it must be filled in some constants, folder names, file names, etc. When everything is filled in correctly, run the script, and it will plot the measured strain against the applied load, calculate all coefficients for the best fit lines and perform a complete uncertainty analysis. Note that both scripts are plotting the output from both vertical-SG and diagonal-SG although vertical-SG should have about zero output for torque load and diagonal-SG should have about zero output for axial load.

When running the axial load-script, the strain measured by vertical-SG should be linear and approximately zero for zero loads. If it is not linear that might indicate that something is wrong with the strain gauges. If it is far from zero for zero loads then there is something wrong with the offset nulling or the zero deviation is big. The best fit line for the diagonal-SG should be close to zero for all loads and should be horizontal compared to the output from the vertical-SG. If the line is not close to zero, then the diagonal-SGs are reacting to axial load as they should not, according to theory. It is important to investigate why and whether any measures are possible to perform so that the diagonal-SG does not have output for axial load. Two possible reasons to consider is: 1. axial load is not applied in the exact middle so that the axial load applied, is unevenly distributed through the body, or 2. the diagonal-SG is not mounted exactly $\pm 45°$.

The torque load-script works in the same matter as the axial load-script, except that the vertical-SG and diagonal-SG have opposite roles. For the torque load-script, the strain measured by diagonal-SG should be linear and approximately zero for zero loads. If it is not linear that might indicate that something is wrong with the strain gauges. If it is far from zero for zero loads then there is something wrong with the offset nulling or the zero deviation is big. The best fit-line for the vertical-SG should be close to zero for all loads and should be horizontal compared to the output from the diagonal-SG. If the line is not close to zero for all loads, then the vertical-SGs are reacting to torque load as they should not, according to theory. It is important to investigate why and whether any measures are possible to perform so that the vertical-SG does not have output for torque load. Two possible reasons to consider: 1. when applying torque load, the ALMD is also applied some axial forces, or 2. the vertical-SG is not mounted exactly $0°$ and $90°$.

When the vertical-SGs only have output for axial load and the diagonal-SGs only have output for torque load, then the calibration curves may be obtained. The axial load-script is plotting the calibration curve for the vertical-SGs and the torque load-script is plotting the calibration curve for the diagonal-SGs. As long as the degree of the best fit lines is 1, meaning linear, then the script will print out the equations for the calibration lines in the command window as well as the upper and lower deviation lines. If the uncertainties are satisfactory low, then the measurement system is complete and ready to be installed.

Chapter 5

Implementing the Measuring System

When the ATMD is ready to install, 2D and 3D-drawings of TTL should be updated so that the part *Axial Thrust Block Spare Section* is replaced by the final design of the ATMD. A Creo part-file is included in the shared google drive folder.

5.1 Water on the Inside of the ATMD

The drainage of the labyrinth seal water is currently arranged such that there is water on the inside of the Axial Thrust Block Spare Section. When this part is replaced by the ATMD, some measures must be implemented to prevent leakage. There are two main possible solutions: keep the water from entering the inside of the ATMD or to cover the inside of the ATMD with some sealing material that will not influence the measurements.

In Figure 5.1 the ATMD is colored yellow and the two main seals are shown. The labyrinth seals, colored blue, remove the pressure energy in the water but do not block water from passing through. The shaft seals, colored purple, keep the water from leaking through the intersection of one part at standstill and one moving part [11]. Additionally, O-rings keep water from leaking through the intersection of two parts at standstill and must be installed between the ATMD and adjacent parts.

By using an extra shaft seal between the *Head cover top*, part 20 in Figure 1.1, and the rotating *Turbine shaft to runner*, part 13 in Figure 1.1, the water is kept from entering the inside of the ATMD. For the labyrinth seals to work there must be a continuous flow of water through, which means before the blocking shaft seal, water must be drained. Figure 5.2 show this alternative solution with drainage through four drilled holes in the runner hub and drainage in pipes through the cutouts of the ATMD.

The advantage of this solution is that the ATMD does not need modifications and the solution is sure to not influence the measurements. The disadvantage is that other parts of the rig need modifications. Especially by drainage through the hub, Figure 5.2a, involve drilling in an expensive part. There is only room for one shaft seal, so there must be used a type where one is enough.

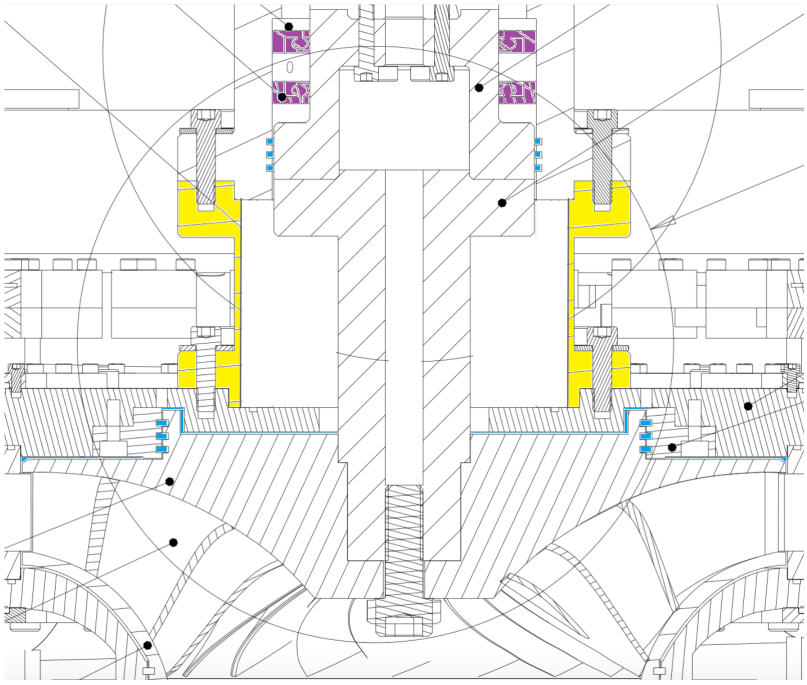

Figure 5.1: Machine drawing of the ATMD (yellow), the labyrinth seals (blue) and the shaft seal (purple).

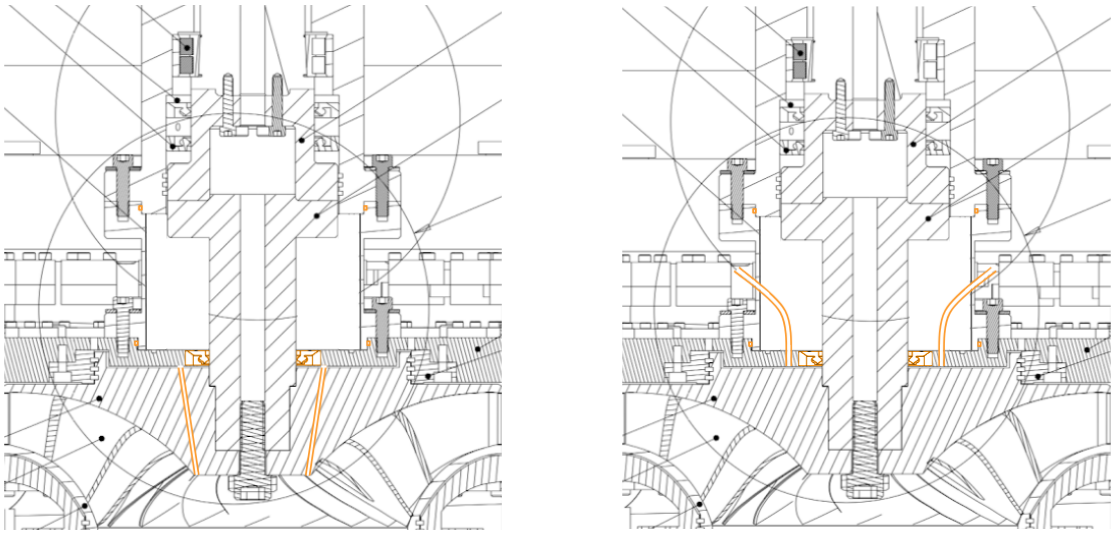

(a) Drainage through the hub.

(b) Drainage through the ATMD.

Figure 5.2: Keeping the inside of the ATMD dry.

A second solution is to allow water on the inside of the ATMD and to use some sealing material to keep it from leaking, see Figure 5.3. If a hard pipe is used, it must have a lower height than the ATMD to make sure it is not carrying any axial forces. There must also be installed an upper and lower O-ring to keep water from leaking between the pipe and the ATMD. The sealing material may also be a soft plastic foil that can be glued on. The glue must be water-resistant and have great adhesive strength on both plastic and stainless steel. Also for this case, water must be drained for the labyrinth seal to work, and the drainage will be through pipes through the sealing material.

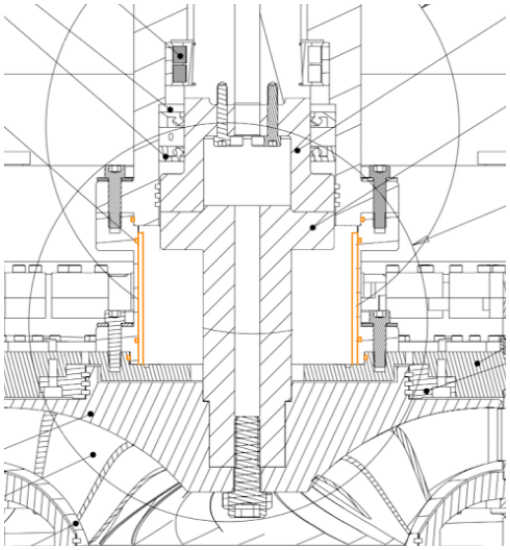

Figure 5.3: Covering the inside of the ATMD.

The advantage of this solution is that it is only the ATMD that needs modifications and every change is possible to undo. A disadvantage is that the hard pipe must be custom made with an outer diameter of exactly 178 mm, which is the inner diameter of the ATMD, and a height less than 110 mm, which is the height from the *Head Cover Top*, the vertical rest of the ATMD, to the *Bearing Housing*-part. A disadvantage with the soft sealing material alternative is the high demands of the adhesive and the risk of leaks.

An additional advantage of this solution is the opportunity to use the sealing pipe as a safety measure. The maximum stress in the ATMD with maximum applied force is numerically calculated to be less than 36 % of yield strength, see section 1.1, and by using the Goodman mean stress method to calculate the fatigue life, the ATMD should handle more than 10^6 cycles before there is a risk of destruction. This means that the ATMD should have no problem for all range of use at TTL. Even so, the final design of the ATMD is significantly weaker than the 18 mm thick Axial Block Spare Section currently installed, and are more likely to break due to an extraordinary incident. The sealing pipe may be a thick steel pipe with a 109 mm height. At this height, it will not influence the measurements as it will not carry any axial forces, and if the ATMD would ever break, the runner and associated parts would fall maximum 1 mm and land on the steel pipe and limit the extent of possible damage.

5.2 Use of the measuring device

After installation, the output from the strain gauges must be included in the main signal acquisition program together with the formulas calculating applied force, friction torque and the uncertainties. For a suggestion for how to perform calibration of the device while installed in the rig, see the Master's Thesis of Selmurzaev Chapter 5.1 and 5.2 [12].

Bibliography

[1] A. Engøy, *Master's Thesis: Development of a Francis Turbine Test Rig at Kathmandu University*. NTNU, 2019.

[2] ——, *Project Thesis: Development of a Francis Turbine Test Rig at Kathmandu University*. NTNU, 2019.

[3] Atlas Steels Technical Department. (2013) *Stainless Steel Grade Datasheets*. [Online]. Available: http://www.worldstainless.org/Files/issf/non-image-files/PDF/Atlas_Grade_datasheet_-_all_datasheets_rev_Aug_2013.pdf

[4] K. Bell, *Konstruksjonsmekanikk Del 2 Fasthetslære*. Fagbokforlaget, 2015.

[5] A. J. Wheeler and A. R. Ganji, *Introduction to Engineering Experimentation*. Pearson, 2010.

[6] K. Hoffmann. (2019) *Applying the Wheatstone Bridge Circuit*. [Online]. Available: http://eln.teilam.gr/sites/default/files/Wheatstone%20bridge.pdf

[7] K. Jakobsen, *Måling med strekklapper*. Tapir, 1979.

[8] Physikalisch Technische Bundesanstalt. (2004) *Calibration of Pressure Gages*. [Online]. Available: https://www.ptb.de/cms/fileadmin/internet/dienstleistungen/dkd/archiv/Publications/Guidelines/DKD-R_6-1_2016_englisch.pdf

[9] Dynatech India. (05.06.2017) *Strain gage installation procedure*. [Online]. Available: https://www.youtube.com/watch?v=qJDRllcchBo

[10] N. Instruments. (2019) *Connecting Strain Gages to a DAQ Device*. [Online]. Available: http://www.ni.com/getting-started/set-up-hardware/data-acquisition/strain-gages

[11] SKF. (2013) *Industrial Shaft Seals*. [Online]. Available: https://www.skf.com/binary/83-129139/Industrial-shaft-seals---10919_2-EN.pdf

[12] M. Selmurzaev, *Master's Thesis: Design of the measurment setup for the friction torque and axial load on the Francis turbine test rig*. NTNU, 2016.

Andrea Engøy

Development of a Francis Turbine Test Rig at Kathmandu University

NTNU
Norwegian University of
Science and Technology